The role of convection on the basal melting of Antarctic Ice shelves

Mainak Mondal

A thesis submitted for the degree of
Doctor of Philosophy
The Australian National University

October 2019

© Mainak Mondal 2019

This thesis is an account of research undertaken between January 2015 and February 2019 at the Research School of Earth Sciences, the Australian National University, Canberra, Australia. Except where acknowledged in the customary manner, the material presented in this thesis is, to the best of my knowledge, original and has not been submitted in whole or part for a degree in any university.

Mainak Mondal
13 October 2019

The thesis is dedicated to my parents and Dr. Murray William.

Acknowledgments

Thank you to my supervisor Bishakhdatta Gayen for guiding me through this whole project, particularly with your rigorous hands on training on CFD and coding. Thank you for being patient with my numerous mistakes and directing me into the right path.

To my supervisor Ross Griffiths, thank you for contributing your valuable time into this project. I was always mesmerise by your profound knowledge and insights into this problem. Thank you for your guidance and inspiration throughout my PhD.

Thank you to Ross Kerr, Andy Hogg, who has been my mentors and to whom I can always go to for advice. I also thanks to Callum, Andrew, Mike for your valuable comments in the group meetings.

My endless gratitude goes to the Aidan Heerdegen, James Monroe for you valuable support on coding. Thanks to Alina Bryleva, Robyn Petch, Mary Coldrick and Virginia Wolf for all the administrative support.

Thanks to my CFP fellows, thanks for making my time at ANU some of the most enjoyable years of my life. You have helped me to grow and mature. Particular thanks to my fellow students Cat, Craig, Alice,Taimoor, Paige, Madi, Kate, Josue, Angus, Jemima, Smruti for your company and help.

To ma, papu and aunt, you are such important persons in my life! without your help I won't be doing a Ph.D. in first place. Special thanks to Dr. Murray, for being such a good friend of mine. Without your support not sure how I would have finished my Ph.D. Thanks to Mr. Lyn Kingston for your financial support. Thanks to Peter, Nicat, Ayan, Christoph, Chandrima, Tonmoy and Arpita for being such good friends.

I gratefully acknowledge the support by the ANU Ph.D fellowship, provided by the Australian Government Research Training Program. The research was supported by Australian Research Council grants DP120102772 and DP120102744. B.G. was supported by ARC DECRA Fellowship DE140100089 and an Australian Antarctic Division RJL Hawk Fellowship to BG. Numerical computations were carried out on the Australian National Computational Infrastructure, ANU.

Preamble

The main body of the thesis (Chapters 2 to 4) is composed in the three scientific journal publications. The majority of the work is attributable to the thesis author, Mainak Mondal, who was the primary researcher of each paper, with co-authors aiding through supervision, guidance and manuscript editing. The articles are:

Chapter 2 Mondal, M., Gayen, B., Griffiths, R. W., and Kerr, R. C. (2019). Ablation of sloping ice faces into polar seawater. J. Fluid Mech. doi:10.1017/jfm.2018.970.

Chapter 3 Mondal, M., Gayen, B., and Griffiths, R. W., (2019). Effects of ambient current on the melting of the ice shelves. J. Geophys. Res. (in progress).

Chapter 4 Mondal, M., Gayen, B., McConnochie, C. and Griffiths, R. W., (2019). DNS of melting with subglcaial discharge under sloping ice-shelves. J. Geophys. Res. (in progress).

Abstract

Melting of the Antarctic ice-shelves has a large impact on ocean circulation, future sea level rise and the global climate. Most of the ice-shelves in Antarctica are sloped forward into the ocean forming an ice cavity underneath. The turbulent transport of heat and salt into the ice interface melts the ice and drives convective wall plumes that play a crucial role in the basal melting. Ice-bathymetry and various ambient flows like tides, waves and sub-mesoscale eddies further modify the plumes. The regional and global ocean models work at scales over 100 meters and rely on crude sub-grid scale parameterization of convection and turbulent processes at the ice-ocean boundary layer, causing uncertainties in the estimation of the melt rate. Over the course of my dissertation I have examined the role of micro scale turbulent processes at the ice ocean boundary using Direct Numerical Simulation (fully resolving convection and turbulence). We carry out simulations by varying the slope of the ice shelves, changing the strength of ambient flow and including sub glacial discharge. Our results show that the melt rate is controlled by the slope of the ice-face with decreasing melt rate at shallower slopes. Over the geophysical flow regime, convection is still a key parameter that controls the heat and salt transfer into the ice-face and hence the melt rate. The results from this study significantly widen our present understanding of the basal melting and can improve the ice-ocean parameterizations for large-scale models. .

Contents

Acknowledgments **7**

Preamble **9**

Abstract **11**

1 Introduction **1**
- 1.1 Mass loss in Antarctica 1
  - 1.1.1 Antarctic Ice sheets and Ice cavities 3
- 1.2 Ice ocean interface 5
  - 1.2.1 Theoretical development 7
  - 1.2.2 Experimental studies 8
  - 1.2.3 Observational studies 10
  - 1.2.4 Ocean modelling and ice Ocean parameterization 11
- 1.3 Direct Numerical Simulations 14
- 1.4 Thesis Outline 15

2 Effects of slope on the boundary layer transport at a ice-seawater interface **17**
- 2.1 Introduction 17
- 2.2 Formulation of the problem and solution techniques 20
- 2.3 Scaling Analysis 26
  - 2.3.1 Laminar Boundary layer flows: viscous-buoyancy balance . . . 27
  - 2.3.2 Turbulent boundary layer flows: boundary layer inertia-buoyancy balance 29
- 2.4 Results 33
- 2.5 Discussion and Conclusions 44

3 Effects of ambient current on the melting of the ice shelves **47**
- 3.1 Introduction 47
- 3.2 Problem set up 49
- 3.3 Results 53
- 3.4 Discussion and Scaling analysis 61
- 3.5 Conclusions 66

4 Effects of subglacial discharge under sloping ice shelves of Antarctica **69**
- 4.1 Introduction 69
- 4.2 Problem formulation 72
- 4.3 Scaling theory 76

4.4 Result 78
4.4.1 Turbulent kinetic energy budget 87
4.5 Discussion and Conclusion 88

5 Conclusion **91**
5.1 Discussion and Future work 92

List of Figures

1.1 Meltrate (m/yr) around Antarctic basins [Rignot et al., 2013]. Size of the circles represent the amount of ice loss with black and striped portion representing its relative contribution from melting and calving (Gt/yr). 2

1.2 Cavity circulation under sloping ice-shelves. 4

1.3 Schematic of the pathways of different watermass formations at the Antarctic ice shelves. Dashed lines represent the front of the different water masses [Dinniman et al., 2016]. 6

1.4 Schematic of the ice-ocean boundary layer, showing a buoyant turbulent plume formed due to melting and the corresponding various components of heat and salt fluxes at the interface. 7

1.5 Laboratory experiments on vertical ice-block in salty water at oceanic ambient. a) Shadowgraph image of convectively unstable turbulent boundary layer by the fresh buoyant meltwater from the ice-water interface (shown by the black vertical section) at ambient temperature $T_b = 4°\text{C}$ and ambient salinity $S_b = 3.55$ wt% Nacl [McConnochie et al, 2016a]. b) Similar shadowgraph image of fresh meltwater in a stratified ambient with Brunt-Vaisala frequency of 0.214 rad s^{-1} showing double diffusion intrusion layer spanning out of the boundary layer with with same T_b and S_b [McConnochie et al., 2016b]. 9

1.6 Observations from the Autonomous Underwater Vehicle (AUV) under Pine island glacier (PIG) a)High resolution Ice-bathymetry data [Dutrieux et al., 2014], b) Distribution of the slope angle under the glacial tongue around various Antarctic basins [Patton et al., 2016], c) Swath of the AUV, profiling the salinity under the ice-cavity of PIG [Jenkins, 2011a]. 11

1.7 a) Reanalysis of the tidal flow speed around Antarctic basin based on mooring data. b) enlarged view of the tidal flow distribution around Ronne and Flichner ice shelf in the southern Weddell Sea [Padman et al., 2018]. 12

2.1 Schematic of the simulation domain shown in respect to the schematic that of a typical ice-shelf in Antarctica. The ice face of length L is in contact with seawater beneath at initial temperature T_w and salinity S_w. At the bottom right, the domain has an open boundary condition using a sponge layer. Interface conditions at the ice (T_{int}; S_{int} and dissolution velocity V) are evaluated from heat and salt flux balances at that boundary. 21

2.2 Simulated and theoretically predicted (2.14) laminar to turbulent transition length, where the prediction (curves) are based on the critical Grashof number for a vertical wall ($Gr_c^{\perp} = 10^9 - 10^{10}$). The simulated transition length L_t is calculated based on turbulent statistics from the simulations for $L = 1.8$ m and 20 m, respectively. 24

2.3 Schematic of the theoretical model boundary layer structure, with up-slope velocity and solute concentration profiles in the wall-normal direction, for the case of a turbulent plume (thicknesses not to scale). . . . 27

2.4 Temporal evolution of ablation rate ($\mu m/s$) measured at the mid-length for slope angle $\theta, = 2°$, 50° and 80° in the 1.8 m domain. 31

2.5 Snapshots of the up-slope velocity u_ζ (colour scale in m/s) on a vertical $\zeta - \eta$ plane normal to the ice face for slopes (a) $\theta = 2°$, (b) 50° and (c) 80°, respectively, with $L = 1.8$ m. 33

2.6 Similar to figure 2.5, up-slope velocity u_ζ (colour scale in m/s) for (a) θ = 5°, (b) θ = 10° and (c) θ = 20°, respectively, for $L = 20$ m. The slope-normal distance η is enlarged by approximately 10 times relative to the slope-parallel scale in order to more clearly show the structure in the boundary layer. 34

2.7 Snapshots of (a) temperature T (°C) and (b) salinity S (gkg^{-1}) fields for $\theta = 50°$. 35

2.8 (a) Along-slope profiles of instantaneous laminar ($\theta = 30°$) and turbulent ($\theta = 80°$) dissolution rates. (b) Instantaneous laminar dissolution rates for $\theta = 2°$, 10° and 30°, respectively, as a function of along-slope distance (in logarithmic scale) for $L = 1.8$ m, along with the theoretical 1/4 scaling (2.22) for laminar ablation rate for an arbitrary slope angle (continuous line). Values are taken after the flow field reaches quasi-steady state. 36

2.9 Time averaged ablation rates at mid-length as functions of (a) slope angle θ and (b) $\sin\theta$. In (b) scales are logarithmic. Lines show the predicted 1/4 (dashed line) and 2/3 (solid line) power laws as predicted by (2.22) and (2.40). • turbulent boundary layer with $L = 1.8$ m; ◦ turbulent boundary layer with $L = 20$ m, △ laminar boundary layer with $L = 1.8$ m. 37

2.10 Thermal boundary layer thickness δ_T (m) as a function of (a) slope angle θ and (b) $\sin\theta$ (scales are logarithmic). Solid and dotted line show the predicted scaling, (2.26) and (2.42), respectively. Symbols as in figure 2.9. 38

2.11 Salinity boundary layer thickness δ_S (m) as function of (a) slope angle θ and (b) $\sin\theta$ (scales are logarithmic). Solid and dotted line shows the predicted scaling of (2.19) and (2.38), respectively. Symbols as in figure 2.9. 38

2.12 (a) Snapshot of slope-normal advective buoyancy flux (sum of mean ($U_\eta\rho^*$) and turbulent ($u'_\eta\rho'$) advective fluxes in kg s^{-1}/m^2), for $L = 1.8$ m and $\theta = 80°$, (b) Absolute value of time- and area-averaged total wall-normal buoyancy flux as a function of $\sin\theta$, where the real values are negative; scales are logarithmic. In (a) the slope-normal distance is enlarged by approximately 10 times relative to the slope-parallel scale in order to show the structure inside the boundary layer. In (b) the dashed line has slope 2/3. The averaging is over a period $\tau \sim 10\tau_b$ and across the thickness of the velocity boundary layer. 39

2.13 The instantaneous distribution of turbulent kinetic energy, K (colour scale in m^2/s^3) in turbulent boundary layers for slope angle (a) $\theta = 50°$ and (b) $\theta = 90°$ for $L = 1.8$ m and (c) $\theta = 5°$ and (d) $\theta = 20°$ for $L = 20$ m. A middle portion of the domain (the actively turbulent region) is shown and in (c) and (d) the slope-normal distance is enlarged by approximately 10 times relative to the slope-parallel scale in order to more clearly show the turbulent activity in the boundary layer. 40

2.14 Snapshot of rates of (a) turbulent shear production, P (m^2/s^3), (b) buoyancy production B (m^2/s^3) and (c) viscous dissipation, ε (expressed in a logarithmic colour scale) for $\theta = 90°$ in 1.8 m domain. 41

2.15 Snapshot of rates of (a) turbulent shear production P (m^2/s^3), (b) buoyancy production B (m^2/s^3) and (c) viscous dissipation ε (expressed in log scale) for $\theta = 10°$ and $L = 20$ m. The slope-normal distance is enlarged by approximately 10 times relative to the slope-parallel scale in order to show the structure inside the boundary layer. 42

2.16 Normalised time and area averaged turbulent statistics as function slope angle; (a) turbulent kinetic energy $\langle K\rangle$ is normalised by characteristic velocity scale $U_c \sim (g\beta\Delta SL)^{1/2}$, (b) turbulent dissipation $\langle\varepsilon\rangle$, buoyancy production $\langle B\rangle$, and turbulent shear production $\langle P\rangle$, for 1.8 m domain (filled symbols) and for 20 m domain (open symbols) normalised using the respective domain length L and velocity scale U_c. 43

3.1 Simulated flow field with $T_b = 1°$ and $U_b = 0.05$ ms^{-1}. Plume velocity, u_ζ (ms^{-1}) and spanwise velocity v (ms^{-1}) are shown in $\eta - \zeta$ and $\eta - y$ respectively. The spatial variation in meltrate, V (m/yr) is shown over the ice face ($y - \eta$ plane) as viewed through the ice. 51

3.2 Snapshot of the spanwise velocity field, v (ms^{-1}) over $y - \eta$ plane for a) $U_b = 0.0$ ms^{-1} and b) $U_b = 0.05$ ms^{-1} and c) $U_b = 0.1$ ms^{-1}. Data taken for $T_b = -1°C$. 53

3.3 Snapshots of up-slope velocity, u_ζ (ms^{-1}) in $\zeta - y$ plane for a) $U_b = 0$ ms^{-1} (purely convective flow), b) $U_b = 0.05$ ms^{-1} and c) $U_b = 0.1$ ms^{-1} respectively. Ambient conditions similar to figure 3.2. 54

3.4 a) wall-normal profile of the u_ζ for different ambient currents as a function of wall normal distance. b) same plots over a friction coordinate, $\eta^+ = \eta * u^*/\nu$. Where u_τ is the friction velocity at the wall given by $u^* = \sqrt{\tau/\rho}$, $\tau = du_\zeta/d\eta$. 54

3.5 Meltrate V (μms^{-1}) as a function of ambient flow, U_b (ms^{-1}) for a slope angle, $\theta = 10°$ and two different background temperatures, $T_b = -1°$C (blue dot) and $T_b = 1°$C (red dot) respectively. $U_b = 0$ ms^{-1} corresponds to a purely convective flow field. The red and blue dashed line represents the theoretical estimation of the meltrate based on the convective scaling [Mondal et al., 2019]. 55

3.6 Meltrate V (μ ms^{-1}) as a function of friction velocity, u^* (ms^{-1}) with $T_b = -1°$C and 1°C respectively for a slope angle $\theta = 10°$. Blue and red filled circles (at respective T_b as in figure 3.5) correspond to simulated meltrates where boundary layer is shear driven ($U_b >> 0.07$ ms^{-1}) , while the open symbols represents when the flow convectively driven. Black triangles are the simulated meltrate for a convective only case, with $T_b = 2.3°$C, over a range of slope angle, $\theta = 50° - 90°$, where data are taken from Mondal et al. [2019]. 56

3.7 Estimated drag coefficient, C_d based on the DNS data as a function of the mean velocity at the far field $U_{\zeta m} = \sqrt{U_b^2 + U_\zeta^2}$. Blue triangle represents C_d for the convective plume over a closed domain with varying slope angles, cyan circle represents the same for a periodic domain, blue and red circles represent C_d for a boundary layer forced by an ambient flow orthogonal to the convection direction for ambient temperature $T_b = -1°$ C and 1° C respectively. Convection dominated region and shear dominated region are represented by the green and orange shadow respectively. 57

3.8 Instantaneous snapshot of meltrate (ms^{-1}) at $T_b = -1°$ C, estimated from the thermal flux at the ice interface ($\zeta - y$ plane) for a) $U_b = 0$ ms^{-1} (purely convective flow), b) $U_b = 0.05$ ms^{-1} and c) $U_b = 0.15$ ms^{-1} respectively. 58

3.9 Plots of the iso-surfaces of spanwise vorticity (ω_y), along with the spanwise velocity (v ms^{-1}) in the ζ direction for a) $U_b = 0.05$ ms^{-1} and b) $U_b = 0.1$ ms^{-1}. 59

3.10 Schematic of the vortex stretching mechanism in the flow direction as a result of the interacting convective and shear boundary layer. 60

3.11 Instantaneous snapshot of the tke in the $\zeta - \eta$ plane for a) $U_b = 0$ ms^{-1}, b) $U_b = 0.05$ ms^{-1}, c) $U_b = 0.1$ ms^{-1} (top panel). Time and domain averaged *tke* as a function of the wall-normal distance (η) is shown in d), e) and f). 62

3.12 Time and spatial averaged buoyancy production (B), turbulent shear production (P) and dissipation (ϵ) as a function of the wall-normal distance (η), for a) purely convective flow field ($U_b = 0$ ms^{-1}) and b) forced flow field ($U_b = 0.1$ ms^{-1}). 63

3.13 Domain averaged profile of normalised salinity anomaly(blue) and normalised mean velocity, $U = \sqrt{U_\zeta^2 + U_b^2}$ (red) as a function of the wall-normal distance (η), for (a) purely convective boundary layer and (b) $U_b = 0.1$ ms^{-1}. The horizontal axis is logarithmic. Based on the profile of velocity the boundary layer is divided into viscous sublayer (characterised by uniform velocity gradiant), logarithmic inner layer (characterised by logarithmic velocity profile) and outer layer. 64

3.14 (a)Local Froude number, Fr_{local}^2 and Grashof number, Gr_{local} plotted as a function of ambient velocity U_b for $T_b = 1°$ C. The triangles and circles represent a convection dominated and shear dominated flow field respectively. (b) Local friction Reynolds number is plotted as a function of background velocity U_b, estimated for three different ambient temperature, $T_b = 0°$ (green dots), $T_b = 1°$ (blue dots) and $T_b = 2°$ (red dots) respectively. 65

4.1 a) Real world schematic of subglacial discharge at the grounding line of a sloping ice-shelf [Moyer et al., 2017]. b) Schematic of the simulation domain. The ice face of length L is in contact with seawater beneath at ambient temperature T_w and salinity S_w. The ice face is sloped at an angle $\theta = 10°$ with the horizon. The discharge flux is added from the side boundary near base by prescribing wall-normal velocity with a Gaussian profile. The far right of the ice-wall is an open boundary where a sponge layer is placed [Mondal et al., 2019]. 73

4.2 Top panel: Snapshots of the along-slope velocity, u_ζ (ms^{-1}) during the passing of the discharge front along the ice face with inclination $\theta = 50°$ at an ambient temperature $T_b = 2.3°$C and ambient salinity $S_b = 35$ g kg^{-1}. a), b) and c) are the snapshots taken at time instants 0.03 hr, 0.032 hr and 0.036 hr respectively, after the initiation of the discharge. Temporal evolution of the spanwise averaged meltrate V (μms^{-1}) at a point P which is at $\zeta = 0.6$ m above the bottom of the domain at the ice-interface. Respective time instants of the flow snapshots are shown on the plot with red (point A, before the discharge), blue (point B, immediately after the discharge) and green (point C, after discharge) dots, respectively. 79

4.3 Contour of temporal and spanwise averaged along-slope velocity u_ζ (ms^{-1}) for $\theta = 50°$ with similar ambient condition as in figure 4.2, for a) $B^* = 1$, b) $B^* = 5$ and c) $B^* = 7$, respectively. 80

4.4 Along-slope profiles of the temporally averaged (over 100 buoyancy period) interface salinity, S_i (g kg^{-1}). Triangles and circles represent $\theta = 50^\circ$ and $\theta = 90^\circ$ respectively at different B^* values. $B^* = 1$ represents no discharge case. Uniform ambient temperature, $T_b = 2.3^\circ$ C and salinity, $S_b = 35$ g kg^{-1} is used here. 81

4.5 Temporally averaged along slope profile of maximum plume velocity, u_η over the plume witdth $b_T(\zeta)$ at an along slope distance ζ. The averaging is done for 100 buoyancy periods once the initial gravity current front has subsided. Symbols and ambient conditions as in figure 4.4. 82

4.6 Temporal and spatial averaged plume velocity u_ζ (ms^{-1}) as a function of B^* for slope angle $\theta = 50^\circ$, 65° and 90° respectively. The red and black lines are the theoretical u_ζ(m) based on equation and respectively. 83

4.7 Temporal and spatialy averaged plume (over the plume width) velocity $\overline{u_\zeta}$ (ms^{-1}) as a function of B^* for slope angle $\theta = 50^\circ$ (black symbols), 65° (blue symbols) and 90°(red symbols) respectively. The red line is based on the theoretical scaling based on equation (4.26). The triangles represents average plume velocity without external source buoyancy . . 84

4.8 Temporally averaged meltrate V (μms^{-1}) as a function of the along-slope distance ζ for different B^* values for slope angle $\theta = 90^\circ$ (circles) and $\theta = 50^\circ$ (triangles) respectively at discrete locations, while the dotted line represents the corresponding continuous values. The meltrates are averaged for 0.05 hr after the discharge front has swept across the domain and the boundary layer plume is at quasi-steady state. 85

4.9 Temporal and spatial averaged meltrate V (μ ms^{-1}) as a function of B^* for slope angle $\theta = 50^\circ$ (green symbols), 65° (blue symbols) and 90° (red symbols) respectively. The meltrate is temporally averaged for 0.05 hr and spatially averaged over 0.1 m across the mid-depth, after the discharge front has swept across the domain and the boundary layer plume is resettled to a quasi-steady state. 85

4.10 Snapshot of the a) turbulent shear production (S), b) buoyancy production (B) and c) dissipation (ε) for $\theta = 50^\circ$ (top panel) and d), e), f) are the corresponding values at the same slope angle with $B^* = 5$. . . . 86

4.11 Entrainment coefficient α, calculated based on the gradient of the time averaged volume flux, $\alpha = dQ/d\zeta$, averaged over 0.1 m at $\zeta = 1.2$ m, where the plume velocity and the meltrate are weakly dependent on along slope distance. Red and blue dots are α for $\theta = 90^\circ$, and $\theta = 50^\circ$ respectively, red and blue traiangles are the α of the correspoding θ without discharge ($B^* = 1$). 88

List of Tables

3.1 Simulations 52

4.1 Estimation of the coefficient c2 based on the simulation parameter. . . 78

Chapter 1

Introduction

The compositionally-driven convection at a melting boundary layer is a fascinating area of research. It is a well known Stefan problem that involves phase transition to take place at the well-defined dynamical interface. In the context of understanding the melting processes of the polar ice caps, it is an intriguing and challenging geophysical problem. Polar ice-sheets are subjected to forcings ranging from planetary scales down to dissipative scales. Large scale dynamics fail to explain entirely the observed behaviour of the ice-sheet responses from seasonal scales to decadal scales. Most of the recent scientific work indicates that the small scale turbulent process is of equal importance alongside the synoptic scale forcings (by the warm ocean and atmosphere). The present study seeks to analyse and understand the behaviour of the turbulent boundary layer at the melting ice-ocean interface, identifies the underlying processes and attempts to interpret the observed behaviour of the polar ice-loss from the analysis of the turbulence right at the ice-ocean interface using turbulence resolving simulations.

1.1 Mass loss in Antarctica

Antarctic ice sheets are the largest storage of fresh water on earth, containing almost 27 million Km^3 of ice [IPCC, 2014; Vaughan et al., 2013]. The sea level would rise upto 58 m if all the Antarctic Ice caps are melted [Shepherd et al., 2018]. Over the past decade the melting rate of Antarctic ice has increased by more than 75% [Payne et al., 2004] and at present is melting at an alarming rate [Harig et al., 2015; Helm et al., 2014; Martín-Español et al., 2016; McMillan et al., 2014; Rignot et al., 2011; Shepherd et al., 2012b; Velicogna, 2009]. A combination of satellite observations and large scale modelling reveals a net loss of 2,720 ± 1,390 billion tonnes of ice between 1992 and 2017. The amount corresponds to an equivalent increase in mean sea level by 7.6± 3.9 millimetres [Gardner et al., 2018]. The rapid loss of ice is particularly evident along the west Antarctic coastline: the Amundsen and the Bellingshausen Seas, Pine Island Bay and Antarctic Peninsula. Between 1992 and 2011, the ice sheets of East Antarctica, West Antarctica and the Antarctic Peninsula changed in mass at rates -14 ±43 Gt/yr, -65±26 Gt/yr, and -20 ±14 Gt/yr, respectively [Shepherd et al.,

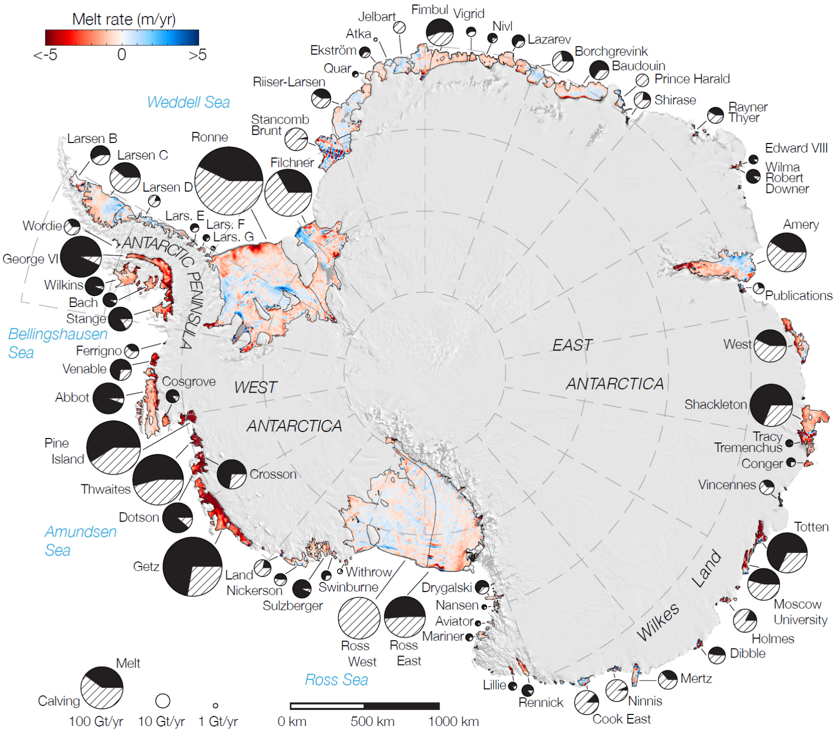
Melt rate (m/yr)
<-5
0
>5
Weddell Sea
Jelbart
Fimbul
Vigrid
Nivl
Lazarev
Atka
Ekström
Quar
Borchgrevink
Baudouin
Prince Harald
Shirase
Riiser-Larsen
Rayner
Thyer
Stancomb Brunt
Ronne
Filchner
Larsen B
Larsen C
Larsen D
Lars. E
Lars. F
Lars. G
Edward VIII
Wilma
Robert
Downer
Amery
Publications
Wordie
George VI
Wilkins
Bach
Stange
Bellingshausen Sea
Ferrigno
Venable
Abbot
Pine Island
Thwaites
Dotson
Amundsen Sea
Getz
Cosgrove
Crosson
ANTARCTIC PENINSULA
WEST
ANTARCTICA
EAST
ANTARCTICA
West
Shackleton
Tracy
Tremenchus
Conger
Vincennes
Totten
Moscow University
Holmes
Dibble
Mertz
Ninnis
Cook East
Rennick
Lillie
Wilkes
Land
Land
Nickerson
Sulzberger
Withrow
Swinburne
Drygalski
Nansen
Aviator
Mariner
Ross West
Ross East
Ross Sea
Melt
Calving
100 Gt/yr
10 Gt/yr
1 Gt/yr
0 km
500 km
1000 km

Figure 1.1: Meltrate (m/yr) around Antarctic basins [Rignot et al., 2013]. Size of the circles represent the amount of ice loss with black and striped portion representing its relative contribution from melting and calving (Gt/yr).

2012a].

The net ice loss around Antarctic basins is contributed by different processes like sublimation, fringing/calving and melting. Ice shelves are permafrost that drifts into the sea. The stability of the ice sheet is dependent on the balance between the buoyant force on the submerged ice and the weight of the sub-areal ice. A 3D schematic of the ice-shelf is shown in figure 1.2. These drifting glaciers rest on the bedrock that can either be inclined forward or backward, depending on the basin. Therefore, the stability of the ice shelf depends on the nature of the slope of the bedrock. Intrusion of quiescent warm and salty water at the base of the ice shelf for a forward sloping bedrock melts the ice-shelf base and can lubricate the resting ground that results in an enhanced ice draft. On the other hand, if the bedrock is inclined backward the intrusion of ambient salty water causes a faster retreat of the ground line (the last point of contact of the ice-shelf with the bedrock). As the ice-shelves drift into the sea, they are subjected to tidal and structural stress over the overhanging region. As a result, the ice-shelves can fringe and add to the sea ice. This fringing of the ice-front (also called calving of ice) at the glacier tongue, and melting of the ice-base near the grounding line, are the two major contributors to the Antarctic ice loss [Rignot et al., 2013; Depoorter et al., 2013]. Figure 1.1 shows the distribution of ice-loss around Antarctica and the corresponding relative contributions from melting and calving [Rignot et al., 2013]. The study suggests that the contribution to the net ice-loss comes 55 ± 10% of the from the melting process, making it even more significant.

Melting of the Antarctic ice-sheet is driven by both atmospheric and oceanic warming. Over the period 1880-2012 there is a rise of 0.85 °C in the global mean surface temperature [IPCC 2013]. As a result, the present situation is quite vulnerable to further warming. Increasing lack of ice-cover during summer time around Antarctic basins reduces the net surface albedo and captures a significant amount of heat, which would otherwise be reflected away. A 50-year meteorological record attributes a significant contribution of Antarctic ice loss to atmospheric warming [Vaughan et al., 2013]. Recent study using a coupled ice-sheet/ice-shelf model [Golledge et al., 2015] has found that, if atmospheric warming exceeds 1.5°C to 2 °C above present mean temperature, it would trigger the collapse of the entire Antarctic ice sheet. More than 80% surface of the ice-shelf is submerged into the sea and therefore acts as the major contributor to the Antarctic ice-loss from ocean warming. The ambient warm and salty Circumpolar Deep Water (CDW) (figure 1.2 and 1.3) surrounding these ice-shelves often flows up the bedrock and reaches the base of the ice shelves [Walker et al., 2007; Thoma et al., 2008; Wåhlin et al., 2010]. Based on in situ and satellite observation a consistent mean warming of CDW (> 0.5°C per decade) is observed around Antarctica since 2000 [Schmidtko et al., 2014]. Studies by Nakayama et al. [2018], have found 0.1°C- 0.2 °C warming of the CDW over the year 2009-2014.

The present trend of ice-loss suggests severe consequences in the near future. The recent IPCC (Intergovernmental Panel for Climate Change) report says for an emission scenario above RCP 2.6, the ice-loss from Antarctica would raise the sea-level up to 3 meters by the end of the year 2300. A very recent numerical study based on the present trends in the satellite based measurements of polar ice-loss around Greenland and Antarctica, implies a definite 25 cm of global mean sea level rise by end of this century Golledge et al. [2019].

1.1.1 Antarctic Ice sheets and Ice cavities

There are spatial variations in the rate of ice loss around different Antarctic basins. The noticeable difference in the ice loss rate between West and East Antarctica lies in the ice-shelf morphology, the geography of the basin and the coastal wind structure influencing the ambient ocean upwelling [Payne et al., 2004; Bindoff et al., 2000]. The East Antarctic Ice Sheet (EAIS) in general is around 4800 meters thick and well above the sea level, while the surrounding ocean is much colder. West Antarctic Ice Sheet (WAIS), on the otherhand is thinner, warmer and mostly below sea level with the deepest part 2800 meters below sea level. The rate of ice loss at these basins often depends on how easily CDW can reach the ice-shelves. Satellite observations since 1994 reveal that stronger ocean circulation with a small rise in temperature and salinity of the Circumpolar Deep Water (CDW) correlates with the 33% increase in the meltrate at the Pine Island Bay [Jacobs et al., 2002]. The CDW flows up the continental shelf and warms the ambient sea water around these ice shelves. As the ice melts, cold dense water forms in these ice cavities and exits the continental shelf as Antarctic Bottom Water, a crucial component of the global thermo-haline circulation

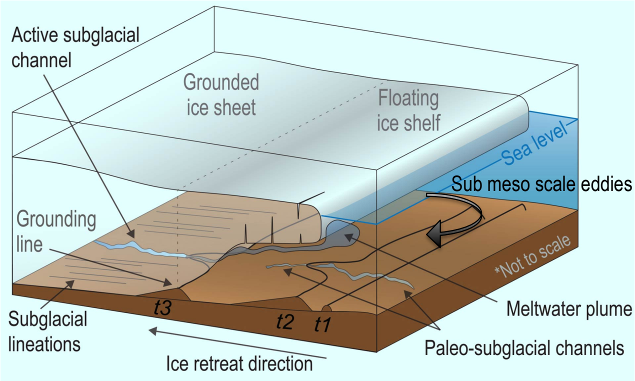

Figure 1.2: Cavity circulation under sloping ice-shelves.

Orse et al. [1999]. The formation of fresher melt water from the Ice shelf creates a strong stratification at the ocean surface that effectively shallows the thermocline depth. With shallower thermocline the pathway of warmer and saltier CDW to reach into the base of the ice shelf increases. With higher melting at the bottom portion of the submerged ice due to lower melting temperature at higher water depth and friction at the bottom bedrock the ice-shelves forms a tongue shaped ice cavity. However for EAIS the scenario is slightly different in the presence of strong katabatic wind. With a much shallower grounding line, an intensified surface forcing often deepens the thermocline at the ice front that restricts the advection of CDW into the ice shelf. As a result the effective thermal forcings at those ice-cavities decrease and creates a negative feedback.

Mechanisms of ice loss under the Antarctic ice cavity involve many dynamic phenomena at various scales. As the continental shelf slopes inwards (as shown in the figure 1.3) the denser HSSW erodes the ice-shelf close to the grounding line causing it to retreat faster and weakening the structure of the ice-shelf. Based on the temperature, the forcing under the ice cavity can either be a hot ocean forcing by increased thermal driving or cold ocean forcing due to changes in the flow structure inside ice cavity [Gwyther et al., 2015]. While the hot ocean forcing dominates most of the western Antarctic basins, cold ocean forcing is more observed in the eastern part of Antarctica (Amery Ice shelf). In situ observations have found a:q substantial increase in melting, driven more by a stronger cavity circulation than by the small increase in local CDW temperature [Jenkins, 2011a].

Recent studies [Khazendar et al., 2013; Gwyther et al., 2014; Silvano et al., 2018] show that regions of deep convection, also known as polynya are another key factor responsible for the warming of abyssal water and the increased meting at the grounding line. Based on passive microwave data over polynya regions in Tottem glacier of West Antarctica, Khazendar et al. [2013] showed that higher melting is occurring due to the intrusion of the warmer and saltier water at the grounding lines through these open ocean polynya. This present trend of ice loss demands an understanding of the melting dynamics and prediction of the future scenarios of Antarctic ice cover due to climate change.

Most of the melting around WAIS takes place at the grounding line below 700 meters from sea level. With a deeper grounding line the ambient pressure increase that depresses the ambient melting temperature at least 2°C below the surface freezing point. At higher pressure at the bottom even the cold ambient water has enough thermal drive to cause a significant melting at these grounding lines. Generally the WAIS are sloped forward into the sea forming a glacier tongue [Jenkins, 2011a]. Under these glacier tongues the slope of the ice-shelves gradually decreases with decreasing depth and becomes nearly horizontal at sea level. At the front part of the ice shelf it is shredded and to connect to sea ice (figure 1.3). Inside the ice cavity two water masses are mainly responsible for the basal melting: The formation of sea-ice causes salt to be released into the ambient shelf-water, which forms a cold (with temperature close to the surface freezing point) and highly saline water mass, called the High Saline Shelf Water (HSSW) next to the ice-front . The dense HSSW sinks to the bottom of the water column depth. It finally flows down into the ice shelf cavity toward the grounding line (figure 1.3). Warmer and saltier Circumpolar Deep Water (CDW) is generally prevented from entering into the ice cavity by the Antarctic slope front. However CDW can occasionally make its way into the bottom half of the cavity. The presence of warm and salty water at the grounding line melts the ice and drives a convective plume. As the plume flows up the ice face, it entrains ambient water. This relatively fresher water mass in presence of meltwater has temperature far below the surface freezing point and is called the Ice shelf Water (ISW). As this melt water plume moves up, the ambient pressure decreases and the plume becomes supercooled and refreeze at shallower depths by forming tiny crystals of frazil ice. This frazil ice gets deposited underneath the upper half of the ice-cavity, driving an ice-pump. As a result of this ice-pumping, the shape of the ice cavity evolves dynamically. This ISW mixes with CDW at mid depth and becomes saltier and heavier and eventually flows down the continental shelf as Antarctic Bottom Water (ABW).

1.2 Ice ocean interface

The melting of ice in salty water is a complex problem. We can draw the example of ice-cubes melting in a glass of plain and salt water respectively. The ice-cube in plain water would melt faster compared to salt water due to the fact that the cold and heavy melt water can circulate in plain water and transfers more heat by convection. However in the glass of salt water the circulation is opposed by density stratification under the ice-face that suppresses turbulent convection and the ice-cube melts much more slowly. If the water temperature is now brought down close the 0° C, the freezing point temperature of water, melting would cease in plain water but still continue in the salt water. This is due to the fact that in presence of salt the

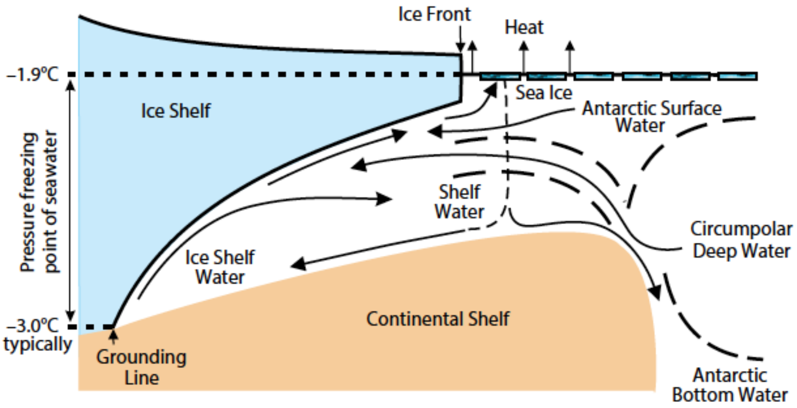
Ice Front
Heat
−1.9°C
Sea Ice
Ice Shelf
Antarctic Surface Water
Pressure freezing point of seawater
Shelf Water
Circumpolar Deep Water
Ice Shelf Water
Continental Shelf
−3.0°C typically
Grounding Line
Antarctic Bottom Water

Figure 1.3: Schematic of the pathways of different watermass formations at the Antarctic ice shelves. Dashed lines represent the front of the different water masses [Dinniman et al., 2016].

freezing point temperature drops, given by the liquidus relation. The freezing point temperature T_{fr}, is represented as a simplified linear relation of the interface salinity S_i and pressure P_i as follows

$$T_{fr} = a_s S_i + bP_i, \tag{1.1}$$

where a and b are constants.

Ice wall in a warmer and saltier ambient (similar to Antarctic ambient) forms a thermal and a salinity boundary layer at the ice-seawater interface. The diffusive fluxes of heat is balanced by the latent heat flux at the melting interface and the conductive heat flux into the ice figure 2.3.

$$Q^H_{ice} - Q^H_w = Q^H_m, \tag{1.2}$$

Similarly salt at the boundary is balanced by the interface salt flux at the ice-ocean boundary and a negligible flux into the ice,

$$Q^S_{ice} - Q^S_w = Q^S_m, \tag{1.3}$$

where Q^H_{ice} , $Q^S_{ice}$and Q^H_w, Q^S_w are the heat and salt fluxes in the ice and water, respectively, Q^H_m is the latent heat flux of melting and Q^S_m is the salt flux at the ice-water interface.

The above three equations are used to solve for the interface condition including the meltrate. The thermal diffusivity of ice is an order of magnitude less than the thermal diffusivity of water while the salinity diffusivity of ice is more than two order magnitude less than water [Pringle et al., 2006]. Therefore, the resulting diffusive fluxes into the ice, Q^H_{ice}, Q^S_{ice} can be neglected in the above equation and interface heat and salt fluxes are effectively controlled by the the Q^H_w and Q^S_w.

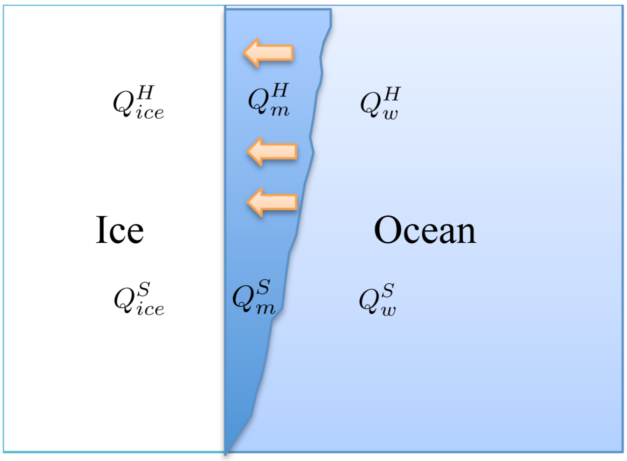

Figure 1.4: Schematic of the ice-ocean boundary layer, showing a buoyant turbulent plume formed due to melting and the corresponding various components of heat and salt fluxes at the interface.

As the ice melts a layer of fresher positively buoyant boundary layer forms and drives a convective plume. The plume flows up the ice wall and shields the ice interface from the ambient ocean. The turbulent eddies in the plume control the heat and salt transport at the ice-ocean boundary layer. Therefore in the estimation of the ice-loss the biggest challenge is to estimate Q^H_w and Q^S_w, which are controlled by the turbulent eddies in the boundary layer and molecular diffusion at the interface.

1.2.1 Theoretical development

Analytical solution of the melting boundary layer is extremely challenging due to complex flow dynamics by the combined impact of thermal and salinity fields. The theoretical scaling of ice melting particularly in presence of turbulence boundary layer involves understanding of both the diffusive and the turbulent transports inside the boundary layer. A thermal and compositional laminar sublayer forms at the interface of an ice-block. The nature of the diffusive sublayers is also controlled by the ambient forcing. In case of strong thermal driving diffusion of solute becomes insignificant and ice simply melts into water. On the other hand in a weak thermal driving diffusion of solute at the ice-interface is coupled with the diffusion of heat the process is called dissolution [Woods 1992, Kerr 1994b]. Wells and Worster [2011] and Woods 1992 showed that this transition between melting and dissolution is dependent on the strength of the ambient temperature and salinity and is independent on the laminar or turbulent nature of the flow.

The thermal and solutal fluxes at the ice-wall are primarily dependent on the advection by the mean flow and turbulent eddies inside the boundary layer. Earlier study on the estimation of the heat flux inside the boundary layer involves asymptotic analytical solution for a vertically heated wall at large Prandtl number, Pr [Kuiken, 1968]. Nilson [1985] extended those solutions for two-component convection. Later [Carey et al., 1980] proposed the theoretical condition for flow reversal based on the ambient thermal and salinity forcing, which is later observed in laboratory experiments for laminar [Carey and Gebhart, 1982] and turbulent flow [Josberger and Martin, 1981]. Theoretical solution of a laminar flow field for ice dissolution/melting in uniform ambient involves asymptotic similarity solutions that depends on the Prandtl and Schmidt number [Carey and Gebhart, 1982; Wells and Worster, 2011]. Solution of turbulent boundary layer involves the modelling of the turbulent transports. Josberger and Martin [1981] modelled the Reynolds transport using an eddy diffusivity model and used similarity solutions for boundary layer properties including plume velocity. and also proposed laminar to turbulent transition length based on critical Grashof number. Wells and Worster [2011] used similarity solution and found a scaling for the heat transfer coefficient, Nusselt number (Nu, based on the strength of the convective to diffusive heat transfer) and boundary layer thicknesses for a laminar boundary layer next to an dissolving ice interface in an uniform oceanic ambient.

Kerr & McConnochie 2015 used the turbulent heat transfer scaling for Nusselt number with Rayleigh number on a vertical wall and applied it for the compositional convection. They proposed a functional form of dissolution rate which is length independent and the dissolution rate follows $V \sim \Delta T_L^{4/3}$, where ΔT_L is the driving temperature difference between ambient temperature and the freezing point temperature at ambient salinity. For a stratified ambient Huppert & Turner proposed the theoretical layer height for the thermohaline staircase for melting of ice-wall in stratified ambient, McConnochie & Kerr 2016 showed the theoretical dependency of the meltrate with height in a stratified ambient.

For an infinitely long vertical ice-face in a homogeneous ambient, the boundary layer properties can be represented as self-similar profile Josberger and Martin [1981]. Earlier analytical solution on a heated vertical wall Carey and Gebhart [1982] used asymptotic analysis at high Prandtl ($Pr = \nu/\kappa_T$) and Schmidt ($Sc = \nu/\kappa_S$) number at the laminar boundary layer next to a vertical ice block in warm and salty ambient.

1.2.2 Experimental studies

Laboratory experiments with a small ice block, immersed in warm water with a uniform ambient salinity, showed a upward bidirectional laminar boundary layer comprised of an upward moving positively buoyant flow and downward moving denser flow that forms next to the ice face [Josberger, 1979; Carey and Gebhart, 1982]. This flow was observed to be formed by the anomalous buoyancy production due to the difference in the diffusion rate of the temperature and salinity and is dependent on ambient salinity and temperature Carey and Gebhart [1982]. Experiments on a horizontal dissolving interface overlain with lighter dissolving fluid, had found the turbulent flow at the dissolving boundary is controlled by compositional convection [Kerr, 1994]. Experiments on the ablation of a relatively tall (O(1 m)) and

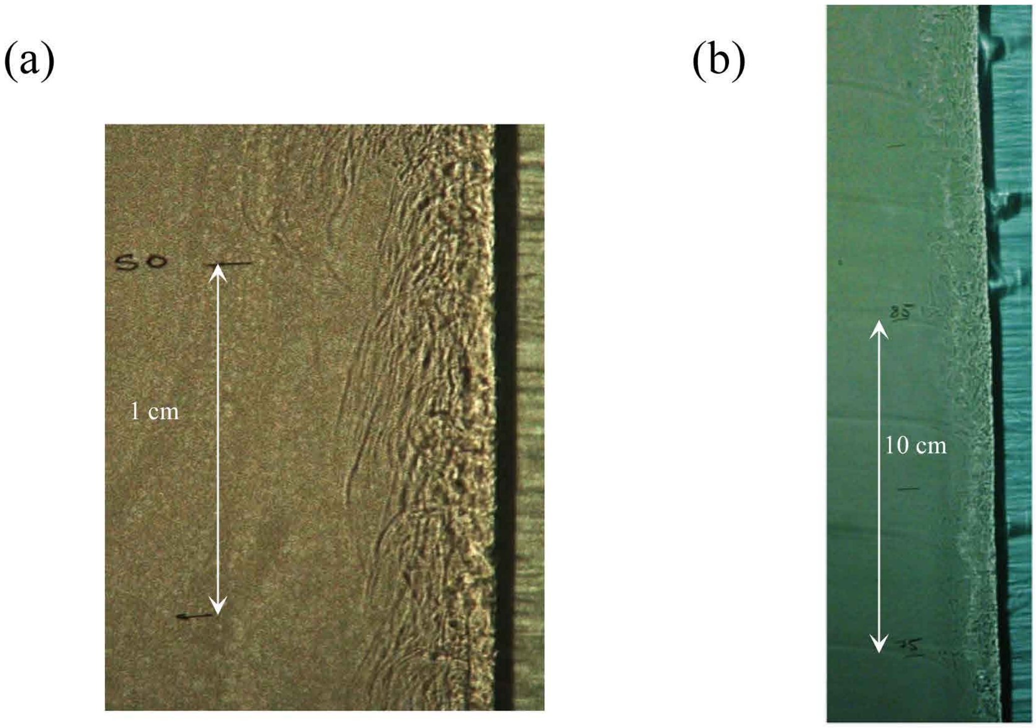

Figure 1.5: Laboratory experiments on vertical ice-block in salty water at oceanic ambient. a) Shadowgraph image of convectively unstable turbulent boundary layer by the fresh buoyant meltwater from the ice-water interface (shown by the black vertical section) at ambient temperature $T_b = 4°\mathrm{C}$ and ambient salinity $S_b = 3.55$ wt% Nacl [McConnochie et al, 2016a]. b) Similar shadowgraph image of fresh meltwater in a stratified ambient with Brunt-Vaisala frequency of 0.214 rad s^{-1} showing double diffusion intrusion layer spanning out of the boundary layer with with same T_b and S_b [McConnochie et al., 2016b].

vertical ice surface in colder and saline (35 %) water of uniform far-field conditions achieved a turbulent boundary layer [Josberger and Martin, 1981]. While at the bottom of the experimental domain, the flow is still laminar and bidirectional, the plume velocity increases with height and the flow eventually transits into a well mixed turbulent flow over a critical length. This transition length is dependent on both the thermal and compositional buoyancy forcing [Josberger and Martin, 1981; Kerr and McConnochie, 2015]. Experimental measurements on vertical ice blocks found that the interface temperature is very much coupled to the interface salinity [Johnson and Mollendorf, 1984; Josberger and Martin, 1981; Kerr and McConnochie, 2015]. For a fully turbulent boundary layer the estimated ice-ablation rate was found to be independent of height [Josberger and Martin, 1981; Kerr and McConnochie, 2015]. Recent experimental measurements using Particle Image Velocimetry (PIV) data have found the velocity of the turbulent plume over a vertical ice-interface correlates with 1/3rd power of the buoyancy flux [Kerr & McConnochie 2015, McConnochie & Kerr 2016 a b]. Ablation experiments over a vertical ice-block in uniform salinity gradient were also conducted for both laminar [Huppert and Turner, 1980] and turbulent [Huppert and Josberger, 1980; McConnochie and Kerr, 2016b] boundary layer. The experiments showed that the meltwater spreads into the interior and forms a series of double diffusive layers, with layer thickness predicted by the theoretical scaling. Based on the experimental data McConnochie and Kerr [2016b] showed that, beyond a critical height determined by a stratification parameter, interface temperature and meltrate decrease with increasing stratification, and the ablation rate decreases with height. Experiments on the side melting of an ice-block, drifting in a uniform ambient current [Fitzmaurice et al. 2016], have found that the melt rate increases non-linearly with the strength of the current. Fitzmaurice et al. 2016, also reported a flow separation at the drifting ice-front beyond a critical flow speed.

1.2.3 Observational studies

The flow field near the ice-water interface is very difficult to measure and the available data are limited. One of the seminal work on the observations of boundary layer flow properties under Erebus Glacier Tongue Jacobs et al. [1981] reports the formation of thermohaline steps induced by melting. In situ measurements Stevens et al. [2014] show the presence of a strong boundary layer shear flow next to the ice face along with a strong stratification inside the ice-cavity [Jenkins, 2011a; Stevens et al., 2014] created by a stable gradient in salinity and an unstable gradient in temperature in those ice-shelve cavities (figure 1.6b). Recently field measurements using an autonomous underwater vehicle (AUV) under Pine Island Glacier (figure 1.6a) have shown rough bathymetry under the ice shelf [Dutrieux et al., 2014] , Patton et al. [2016] tabulated several observations of ice-slope gradiant as a function of the basin width where the slope varies between $0^\circ - 40^\circ$. As the ice melts the fresher melt water plume flows over this rough bathymetry. The fresh water plume shields the ice-interface from the ambient ocean. The flow structure changes over different slopes and so do the turbulent properties at the ice ocean boundary layer. As a result

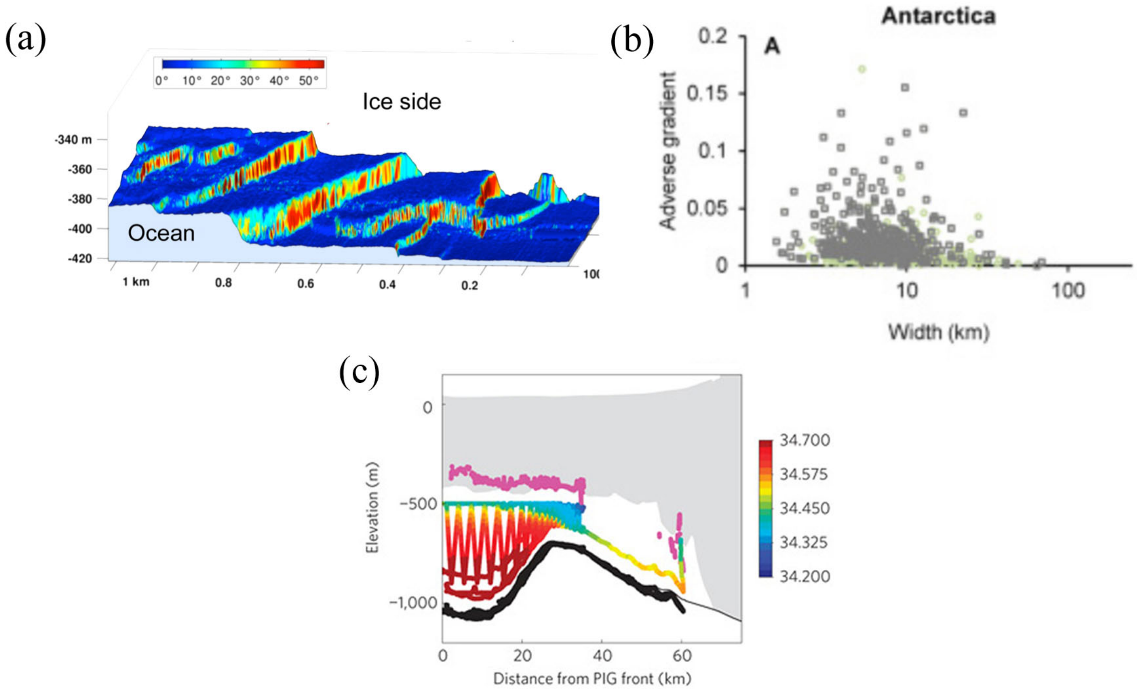

Figure 1.6: Observations from the Autonomous Underwater Vehicle (AUV) under Pine island glacier (PIG) a)High resolution Ice-bathymetry data [Dutrieux et al., 2014], b) Distribution of the slope angle under the glacial tongue around various Antarctic basins [Patton et al., 2016], c) Swath of the AUV, profiling the salinity under the ice-cavity of PIG [Jenkins, 2011a].

the rate of ice-loss over different parts of the rough ice bottom changes according to the turbulent properties and the ice shelf evolves dynamically. Ambient stratification impacts the plume dynamics and forms thermohaline staircases [Kimura et al., 2015]. Satellite and air borne observations around Flichner-Ronne Ice shelf [Makinson et al., 2011; Padman et al., 2018], Larsen C Ice shelf [Mueller et al, 2012] and at the frontal zone of Ross Sea ice shelf [Arzeno et al., 2014] show a strong correlation in the meltrate with the strength of the ambient tidal current (figure 1.7). However at the base of the ice-shelves no such correlation was found [Stanton et al., 2013].

1.2.4 Ocean modelling and ice Ocean parameterization

Modelling of basal melting in a regional ocean model is quite challenging. Most of the present ocean models focus on the flow-field at scales (>O(1) km) while the typical meltwater plume is only O(100) m wide [Dutrieux et al., 2014; Le Brocq et al., 2013; Sugden et al., 1991]. Therefore, these models can not resolve the convective plume and rely on parametrising the small scale turbulent processes occurring inside

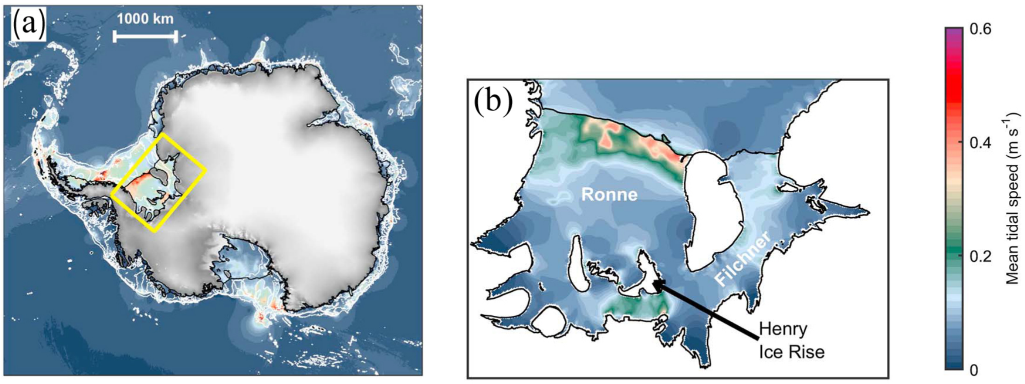

Figure 1.7: a) Reanalysis of the tidal flow speed around Antarctic basin based on mooring data. b) enlarged view of the tidal flow distribution around Ronne and Flichner ice shelf in the southern Weddell Sea [Padman et al., 2018].

the boundary layer next to the ice-face.

Estimation of the melting requires the knowledge of fluxes (heat and salt) from the ice-water interface into the ice and from water into the ice-water interface. Ice is poorly conductive and the diffusivity of salt in ice is negligible [Cameron and Bull, 1962]. Based on the ice core record the heat flux into ice can be neglected without a reasonable violation of energy conservation. Therefore the turbulence fluxes effectively control the ice-ocean interface fluxes. In large scale models these fluxes are parameterised based on turbulent exchange velocity. A simpler, less computationally expensive approach uses a single exchange velocity γ_{TS} based on combined heat and salt transfer coefficient for the estimation of heat flux and is represented as,

$$\gamma_{TS} = \frac{u_*}{\gamma_{Tturb} + \gamma^{TS}_{mol.}} \tag{1.4}$$

Here u^* is the friction velocity related to the stress at the ice-wall, γ_{Tturb} and γ^{TS}_{mol} are the turbulent and molecular counterparts of the transfer coefficient respectively. Here just the heat flux is solved explicitly with implicit solution of the salt flux and an interface temperature estimated from the linear liquidus relation, known as the 2 equations parameterization. A more sophisticated approach [Holland and Jenkins, 1999] solves both the heat and salt fluxes based on respective exchange velocities (γ_T, γ_S) along with similar interface temperature relation, also know as the 3 equation parameterization [Jenkins, 1991].

$$Q^T_w = \rho_w c_w \gamma_T (T_w - T_i) \tag{1.5}$$

$$Q_w^S = \rho_w \gamma_S (S_w - S_i), \tag{1.6}$$

$$T_i = a.S_w + b.T_w \tag{1.7}$$

T_i is the interface temperature, T_w is the ambient temperature, ρ_w, c_w is the density and the specific heat of water and $\gamma_T/\ \gamma_S$ evolved from being considered constant [Hellmer and Olbers, 1989] to

$$\gamma_{T/S} = \frac{u^*}{\Gamma_{Turb} + \Gamma_{mol.}^{T/S}}, \tag{1.8}$$

based on a laboratory experiment over horizontal hydraulically smooth ice-surface [Kader and Yaglom, 1972]. Here, $\gamma_{mol.}^{T/S}$ are based on molecular properties, viz. Pr and Sc, while γ_{Tturb} is a function of fixed Richardson number (ration of buoyancy to shear instability) and Obukhov length [McPhee et al., 1987].

The above parameterisation often undermines the convective boundary layer which is partially incorporated into the parameterization using plume model. The meltwater at the ice-wall forms a positively buoyant plume moving up against the ice-face. The dynamics of the plume and the heat and salt transfer at the ice-face are based the bulk conservation of mass, momentum and buoyancy fluxes across a buoyant plume with local or distributed source of buoyancy [Batchelor, 1954, Morton et al., 1956]. Instead of explicitly solving the diffusive fluxes boundary, they are estimated based on the bulk conservation of fluxes across the plume width. This ?buoyant plume theory' has been predominantly applied to different engineering and geophysical applications, from a ventilated filling box over a heated wall [Cooper and Hunt, 2010], dynamics of a volcanic ash cloud [Baines and Sparks, 2005] to density current over a slope [Wells and Wettlaufer, 2005]. Reed Macayeal [1984] first applied this theory on glacial melting, later Jenkins et al., 1991 coupled BPT to the melting parameterization at the ice-ocean interface.

Recent applications of BPT based ice-ocean parameterisation involves both the study of a Greenlandic tidewater glacier [Cowton et al., 2015; Slater et al., 2016a; Magorrian and Wells, 2016; Carroll et al., 2016] and Antarctic ice shelves [Holland and Feltham, 2006; Payne et al., 2007; Jenkins, 2011b]. Magorrian and Wells [2016] has developed a model for the locally planar sloping ice-face in a linearly stratified ocean based on turbulent buoyant plume theory (BPT). They have proposed scaling laws for melt rate as a function of the far field oceanic conditions and the slope of the ice face. However, the boundary layer properties have not been fully addressed in this study. The portability of the plume theory is often compromised with the over-simplification of the flow field, where a 2D turbulent symmetry is used for closure. Another major assumption of the BPT is that the turbulence in the inner boundary layer of the plume next to the ice wall is shear driven and the mean flow is represented by a quadratic drag law and thermal and saline Stanton numbers [Jenkins 1991, 2011].

Present parameterization schemes used in these models to estimate the heat flux across the ice-face are often not coupled to the grid resolution. The validity of the ice-ocean parameterization based on BPT in an oceanic flow conditions can only be tested either using laboratory experiments with melting ice boundary layer or using turbulence resolving numerical studies. The actual underlying process at these ice-ocean boundary is still not fully understood.

1.3 Direct Numerical Simulations

Direct Numerical simulations (DNS) are becoming more effective in analysing the structure of the boundary layer. DNS is capable of resolving all scales of motion and ensures an accurate description of boundary layer processes including meltrate. First applied on a heat transfer problem over horizontal surface with low Prandtl number (Pr<2) with laminar boundary [Kim and Moin 1989], what had come a long way over the past three decades. It has been applied to convective boundary layer at a heated wall [Kwamura 1998, 1999] with high enough Reynolds number for a purely turbulent boundary layer. DNS has been successfully applied for passive scalar transport at a thermally convective boundary for laminar and turbulent [Herlina and Wissink, 2014] boundary layer. Recently, Gayen et al. [2015] first applied DNS for the study of the binary melt (i.e melting caused by the transport of both heat and solute) at the convective boundary layer at ice-salt water interface for both uniform and stratified ambient. The results replicated the bidirectional flow, also observed in laboratory experiments [Kerr and McConnochie, 2015]. A subsequent DNS study by Gayen et al. [2016], on the dissolution of ice into saline water, for the case of planar vertical interface has showed detailed turbulent structures otherwise difficult to estimate in lab experiments. The simulated dissolution rates are in close agreement with the experiments and predicts a theoretical 4/3 power law of the thermal forcing [Josberger and Martin, 1981; Kerr and McConnochie, 2015]. The DNS also showed the presence of a logarithmic layer in both the velocity and scalar fields in the boundary layer and hints that over a vertical interface boundary layer turbulence could be driven by shear instability.

Most of the earlier DNS study focused on the melting boundary layer next to verical ice-face. However, the ice-ocean interface is subjected to much complex geometry (figure 1.6a) and flow structure (figure 1.6a and 1.7). Most importantly it is still unclear how convection is important on the heat transfer at the ice-ocean boundary layer. Laboratory experiments also suffer from several limitations like domain length scales, replicating oceanic flow structure in laboratory scale and maintaining the consistent ambient condition. This motivates us to employ turbulence resolving simulations of the ice-ocean interface with varying geometry and flow conditions. The present study only addresses the melting of the ice-face only, DNS studies of freezing processes are not included as a part of the present thesis.

1.4 Thesis Outline

The first section of the thesis talks about the effects of ice bathymetry over the convective boundary layer at the ice-ocean interface. Changes in the turbulent flow structure and resulting heat and salt transfer rate and related ice ablation has been studied using a 3 dimensional DNS model. Mechanisms for production of turbulence has been discussed. The second section of the thesis deals with the effects of ambient current on the convective melting at the ice-ocean interface. The conjugate heat and mass transfer by convective plume and ambient shear has been studied and mechanisms for heat and mass transfer has been analysed. Based on this study different melting parameterisation based on the flow regime has been proposed. The third chapter of the thesis talks about the effects of subglacial discharges on the resulting gravity currents on the melting of Antarctic ice shelves. The final and fourth chapter of the thesis discuses the conclusion and future works.

Chapter 2

Effects of slope on the boundary layer transport at a ice-seawater interface

The effects of the slope of an ice-seawater interface on the mechanisms and rate of ablation of the ice by natural convection are examined using turbulence resolving simulations. Solutions are obtained for ice slopes $\theta = 2^\circ - 90^{\circ}$, at a fixed ambient salinity and temperature, chosen to represent common Antarctic ocean conditions. For laminar boundary layers the ablation rate decreases with height, whereas in the turbulent regime the ablation rate is found to be height independent. The simulated laminar ablation rates scale with $(\sin\theta)^{1/4}$, whereas in the turbulent regime it follows a $(\sin\theta)^{2/3}$ scaling, both consistent with theoretical predictions developed here. The reduction in the ablation rate with shallower slopes arises as a result of the development of stable density stratification beneath the ice face, which reduces turbulent buoyancy fluxes to the ice. The turbulent kinetic energy budget of the flow shows that for very steep slopes both buoyancy and shear production are drivers of turbulence, whereas for shallower slopes shear production becomes the dominant mechanism for sustaining turbulence in the convective boundary layer. Based on the present study we present a modified parameterization for convection driven melting as, $V \simeq 8.98 \times (\Delta T_L)^{4/3}(\sin\theta)^{2/3} \quad \mathrm{m/yr}$, where ΔT_L is the thermal driving.

2.1 Introduction

Recent studies report that the rate of loss of the grounded ice mass of West Antarctica has increased by 70% since 2002 [Paolo et al., 2016]. A net mass loss from Antarctic ice sheets has contributed to global ocean sea level rise [Cazenave and Llovel, 2010; Piecuch and Ponte, 2014] and its contribution is expected to become larger in the future. Melting of glacier tongues is also contributing to a stronger fresh water layer over the Weddell Sea and this can result in reduced production of Antarctic Bottom Water, an important component in the global thermohaline circulation [Lavergne et al., 2014]. Much of the acceleration of ice loss has been attributed to increased flow or warming of circumpolar deep water entering cavities beneath floating ice shelves, where it can cause faster melting, retreat of the grounding line and a speed-up of glacier advance [Jenkins et al., 2010; Jacobs et al., 2011]. The rate of melting has been studied using General Circulation Models (GCMs) [Swingedouw et al., 2008; Hellmer and Olbers, 1989; Spence et al., 2014; Snow et al., 2016] and the Regional Ocean Modelling System (ROMS) [Galton-Fenzi et al., 2012a]. Modelling of the Pine Island Glacier and its grounding line, for example, has shown a tight coupling between the ice sheet interior and the surrounding ocean water properties and ablation rate [Rydt and Gudmundsson, 2016]. However, the underlying dynamics of ice melting are quite complex and poorly understood. The melting crucially involves the transport of heat and salt through a thin boundary layer at the ice face, whereas the models cited above resolve the flow-field only at scales larger than O(100) m and rely on assumptions and parameterisations in order to invoke the roles of the convection and turbulent processes that control the melt (or ablation) rate. These parameterisations are also not coupled to the grid resolution, thereby exacerbating the uncertainty in the resulting model solutions [Morrison et al., 2011; Gladish et al., 2012]. In contrast turbulence-resolving simulations, such as the Direct Numerical Simulations (DNS) recently reported by Gayen et al. [2016], along with theoretical modelling, serve as tools to understand the mechanisms governing the melting process. The results from theory and DNS are also likely to provide improved parameterisations for larger scale models, thus enabling more accurate predictions of future ice-shelf melting rates.

Laboratory experiments with a small ice block, immersed in warm water with a vertical salinity gradient, showed a laminar boundary layer next to the ice face and the formation of double diffusive horizontal intrusions [Huppert and Turner, 1978, 1980; Carey and Gebhart, 1982]. Experiments on the ablation of a relatively tall (O(1 m)) and vertical ice surface in colder and saline (35 gkg^{-1}) water of uniform far-field conditions [Josberger and Martin, 1981] achieved a turbulent boundary layer. A recent experimental study [Kerr and McConnochie, 2015] revisited the turbulent ablation of a vertical wall with ambient water temperatures ($0 - 6$ °C) and salinity (35 gkg^{-1}) close to those of Antarctic waters, and showed that the melt rate is independent of height. The results also imply that natural convection is driven by the salinity buoyancy. Diffusion of salt to the ice interface lowers the melting temperature, allowing the ice to melt (or dissolve) even when the interface temperature is less than 0 °C [Woods, 1992; Kerr, 1994; Wells and Worster, 2011; Kerr and McConnochie, 2015].

Scaling laws for the natural convection boundary layer properties and ablation rate have been proposed for various flow scenarios. For a laminar boundary layer next to a vertical ice interface a balance between vertical advection by mean flow and lateral diffusion of solute leads to an ablation velocity that scales to the $-1/4$ power of the height, and the $1/4$ power of buoyancy anomaly, the latter predominantly provided by the salinity field [Josberger and Martin, 1981; Carey and Gebhart, 1982; Nilson, 1985; Wells and Worster, 2011]. For a turbulent boundary layer, on the other hand, a turbulent parameterisation [such as the use of a constant turbulent diffusivity; Josberger and Martin, 1981] is necessary. A recent theoretical model for dissolution [based on an established scaling for turbulent heat transfer for natural convection, Holman, 2010], predicts that the ablation velocity scales as $V \sim \Delta T_L^{4/3}$, where $\Delta T_L = T_w - T_L$ is the difference between the ambient temperature T_w and the freezing point at ambient salinity T_L [Kerr and McConnochie, 2015]. The salinity dependence of T_L implies that the temperature difference ΔT_L, and therefore the ablation rate, are determined by the transport of solute to the ice interface. The quantity ΔT_L is referred to as the 'driving temperature difference' because this temperature difference is the cause of melting and represents the source of the latent heat required for melting. However, it is not to be confused with the source of momentum, which is the solutal buoyancy. Kerr and McConnochie [2015] also show that the theoretical model is consistent with earlier estimation of iceberg melt rate from ocean measurements [Morgan and Budd, 1978; Budd et al., 1980; Shepherd et al., 2004], as well as with their own laboratory experiments.

In large scale ice-ocean models the boundary layer turbulence is assumed to be driven by shear instability of an ambient current or buoyant plume. Where a buoyant plume is modelled it represents a contribution of natural convection at the ice-ocean interface due to either melting of the interface or a subglacial discharge of fresh water [Payne et al., 2007; Jenkins, 1991, 2011a]. Plume models have used the conservation of momentum and heat [Morton et al., 1956; Ellison and Turner, 1959] for a one-dimensional convective plume with 'top hat' profiles across the plume, providing a parameterisation of turbulent fluxes to the ice face. The wall plume model is further developed by incorporating the flux equation for salt transport through a solutal boundary layer under a sloping ice interface [Jenkins, 2011a; Magorrian and Wells, 2016; Slater et al., 2016a]. For a vertical ice face McConnochie and Kerr [2016] have improved the model through laboratory measurements of entrainment into the turbulent plume. Like the parameterisations for the case of an ambient current, use of the plume model assumes that turbulent fluxes to the ice face are a result of instability of the mean shear in the plume.

Three-dimensional Direct Numerical Simulations of the dissolution of ice into sea water have to date focussed on natural convection alone, and a vertical planar ice face. For a range of typical Antarctic water temperatures and salinities the computed dissolution rates [Gayen et al., 2016] are in excellent agreement with the laboratory experiments by Josberger and Martin [1981] and Kerr and McConnochie [2015] and with the predicted 4/3 power dependence of ablation rate on the difference between the far-field water temperature and the interface melting temperature. The DNS also showed that the ablation rate is independent of height when the boundary layer is turbulent at large values of the Grashof number, which implies that the flow is independent of further increase in the size of the computational domain. Another important result from the DNS is logarithmic profiles in velocity and density fields within the boundary layer. This is associated with production of the eddies by the mean shear at a rate comparable to that from convective instability in this vertical natural convection at the Grashof number achieved.

The focus of this paper is the effects of ice face slope on melting rates. Observations of glacier tongues on the seaward side of the grounding line indicate that the ice-water interface has a wide range of slopes [Jenkins et al., 2010]. Melting near the grounding line is of particular interest, as this is where melting is most likely to influence the glacier dynamics and the overall rate of

The focus of this paper is the effects of ice face slope on melting rates. Observations of glacier tongues on the seaward side of the grounding line indicate that the ice-water interface has a wide range of slopes [Jenkins et al., 2010]. Melting near the grounding line is of particular interest, as this is where melting is most likely to influence the glacier dynamics and the overall rate of loss of grounded ice, hence sea level rise [Rignot et al., 2013].The focus of this paper is the effects of ice face slope on melting rates. Observations of glacier tongues on the seaward side of the grounding line indicate that the ice-water interface has a wide range of slopes [Jenkins et al., 2010]. Melting near the grounding line is of particular interest, as this is where melting is most likely to influence the glacier dynamics and the overall rate of Under a sloping ice face the flow and melting are expected to be complicated by a component of the buoyancy force orthogonal to the sloping face, leading to a gravitationally stable salinity stratification in the boundary layer. Attempts to describe the melting of a sloping ice boundary [Jenkins, 2011a; Magorrian and Wells, 2016] have used the turbulent buoyant plume theory. However, there are no turbulence resolving simulations to test the scaling for boundary layer properties and melting rate. The energy pathways for production of turbulence, an important consideration for the formulation of a parameterisation, are also unknown. Here we investigate the effects of slope on the ablation rate and boundary layer properties for ice in contact with uniform and quiescent surrounding sea water using scaling theory and Direct Numerical Simulation. The simulations show complex boundary layer structures and support a new scaling prediction. The energy pathways to turbulence are also examined.

2.2 Formulation of the problem and solution techniques

The flow field is solved in a rectangular domain shown in figure 2.1 with length L parallel to the slope, depth W normal to the ice face and a width D in the spanwise direction (normal to the plane of the schematic). Ice-water interface conditions are applied at one boundary (the ice face) of the computational domain (figure 2.1). The domain and coordinate system are rotated relative to gravity in order to represent the ice slope. Gravity is always directed downward. The flow field is represented by $\tilde{\mathbf{u}} = [u_\eta,\ v,\ u_\zeta]$, where the wall-normal (η), spanwise (y) and slope-parallel (ζ) directions are u_η, v and u_ζ, respectively. The co-ordinates and velocities are relative to a reference frame fixed at the planar ice water interface. This is the most convenient reference frame and we make no assumption about the relative speeds of the glacier advance and ablation. We solve the incompressible continuity, Navier-Stokes, heat and salt equations:

$$\nabla \cdot \tilde{\mathbf{u}} = 0 \tag{2.1}$$

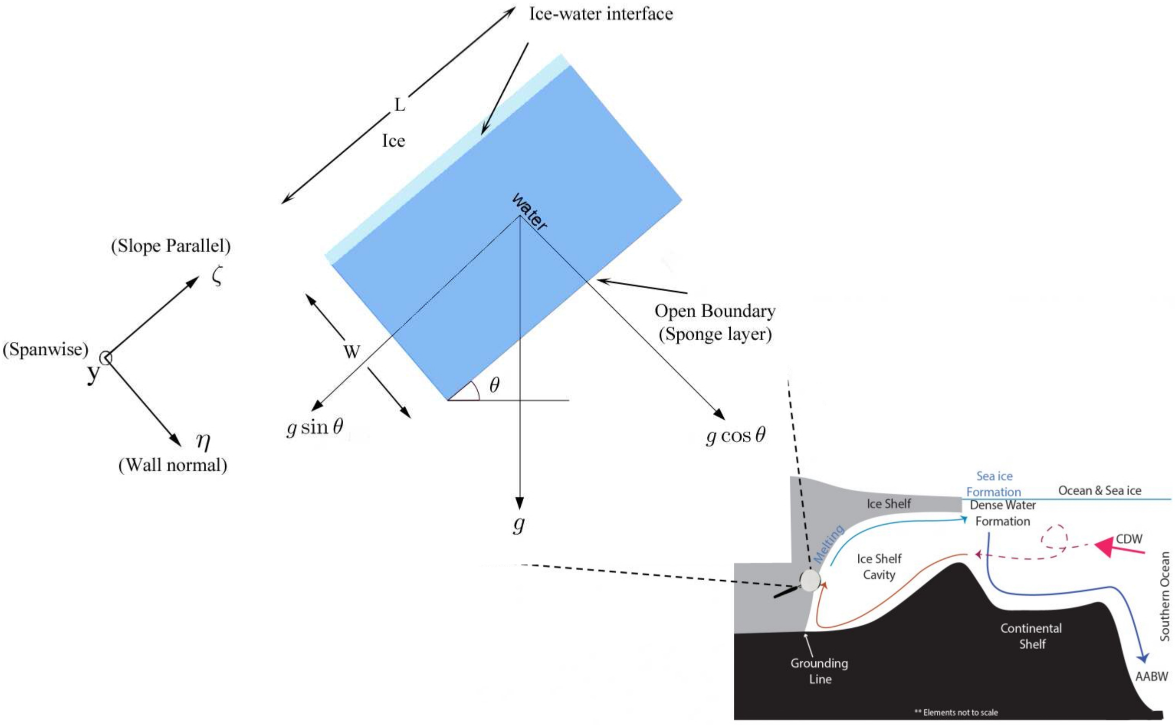
Ice-water interface
L
Ice
water
(Slope Parallel)
ζ
(Spanwise)
y
η
(Wall normal)
W
θ
$g \sin\theta$
$g \cos\theta$
g
Open Boundary
(Sponge layer)
Sea ice
Formation
Ocean & Sea ice
Ice Shelf
Dense Water
Formation
Melting
Ice Shelf
Cavity
CDW
Southern Ocean
Continental
Shelf
AABW
Grounding
Line
** Elements not to scale

Figure 2.1: Schematic of the simulation domain shown in respect to the schematic that of a typical ice-shelf in Antarctica. The ice face of length L is in contact with seawater beneath at initial temperature T_w and salinity S_w. At the bottom right, the domain has an open boundary condition using a sponge layer. Interface conditions at the ice (T_{int}; S_{int} and dissolution velocity V) are evaluated from heat and salt flux balances at that boundary.

$$\frac{\partial u_\eta}{\partial t} + (\tilde{\mathbf{u}} \cdot \nabla) u_\eta = -\frac{1}{\rho_0}\frac{\partial p^*}{\partial \eta} + \nu \nabla^2 u_\eta + \frac{\rho^*}{\rho_0} g \cos\theta \tag{2.2}$$

$$\frac{\partial u_\zeta}{\partial t} + (\tilde{\mathbf{u}} \cdot \nabla) u_\zeta = -\frac{1}{\rho_0}\frac{\partial p^*}{\partial \zeta} + \nu \nabla^2 u_\zeta - \frac{\rho^*}{\rho_0} g \sin\theta \tag{2.3}$$

$$\frac{\partial v}{\partial t} + (\tilde{\mathbf{u}} \cdot \nabla) v = -\frac{1}{\rho_0}\frac{\partial p^*}{\partial y} + \nu \nabla^2 v \tag{2.4}$$

$$\frac{\partial T^*}{\partial t} + (\tilde{\mathbf{u}} \cdot \nabla) T^* = \kappa_T \nabla^2 T^* \tag{2.5}$$

$$\frac{\partial S^*}{\partial t} + (\tilde{\mathbf{u}} \cdot \nabla) S^* = \kappa_S \nabla^2 S^*. \tag{2.6}$$

Here ρ_0 is the reference density for pure water at 0°C and p^*, T^*, S^* and ρ^* denote the deviation from the ambient hydrostatic pressure (p_w), temperature (T_w), salinity (S_w) and density (ρ_w). The saline water has kinematic viscosity ν, thermal diffusivity κ_T and salinity diffusivity κ_S. As the flow involves only a small range of temperatures, the equation of state is closely approximated as linear without significant effects on the solution:

$$\rho^* = \rho_0(\beta S^* - \alpha T^*), \tag{2.7}$$

with coefficient of thermal expansion α and coefficient of haline contraction β. Computational domains of a given length but different slopes have different vertical heights. Thus we compare the flow and melt rate for different slopes at two given values of the global Grashof number (Gr, which is the relative strength of buoyancy to viscous force) and one value of the Stefan number (St),

$$Gr \equiv \frac{g\beta \Delta S L^3}{\nu^2}, \quad St \equiv \frac{\rho_s L_f}{\rho_w c_w (T_w - T_{int})}, \tag{2.8}$$

where, $[S_{int}, T_{int}]$ are the interface and $[S_w, T_w]$ are the far field salinity and temperature, $\Delta S = (S_w - S_{int})$ is the salinity anomaly, c_w is the specific heat, L_f is the latent heat of fusion for ice and ρ_s is the density of the ice. The values of Gr and St are independent of slope because the simulations in section 4 show that the interface temperature and salinity are independent of slope. The Prandtl number ($Pr = \nu/\kappa_T$) and Schmidt number ($Sc = \nu/\kappa_S$) are fixed.

Three relations are applied at the ice-water interface. The freezing point of saline water is closely approximated by a linear function of salinity and pressure:

$$T_{int} = a_s S_{int} + b P_{int} \simeq a_s S_{int}. \tag{2.9}$$

For the present study the effect on the freezing point of hydrostatic pressure difference within the limited domain size is negligible and the interface temperature is assumed to be solely dependent on interface salinity. The slope of the liquidus line is fixed at $a_s = -6 \times 10^{-2}$°C gkg^{-1-1} [Holland and Jenkins, 1999].

The second interface relation expresses the balance between latent heat flux Q^H_m of melting and the divergence of conductive heat fluxes at the interface,

$$Q^H_{ice} - Q^H_w = Q^H_m, \tag{2.10}$$

where Q^H_{ice} and Q^H_w are the heat fluxes to the interface in the ice and water, respectively. The conductive transfer of heat into the ice is very small compared to the total heat being used to melt the ice-shelf under typical Antarctic conditions [Holland and Jenkins, 1999; Kerr and McConnochie, 2015]. We therefore neglect the diffusive heat flux into the ice (setting $Q^H_{ice} \sim 0$). It is also assumed that the diffusion of heat in water at the interface is much faster than the advection of heat by the ablation velocity (i.e. $\kappa_T \partial^2 T/\partial \eta^2 >> V \partial T/\partial \eta\big|_{\eta=0}$, as $V << \kappa_T/\delta_T$, where δ_T is the diffusive thermal boundary layer thickness), so that (2.10) becomes

$$\rho_w c_w \kappa_T \frac{\partial T}{\partial \eta}\bigg|_{\eta=0} = \rho_s V L_f, \tag{2.11}$$

where V is the ablation velocity. We adopt the convention that poisitive ablation velocity indicates melting and retreat of the interface in the negative η-direction (at speed V) relative to the ice mass, or equivalently, translation of the ice mass in the positive η-direction relative to the interface reference frame used here.

An analogous equation is used to describe the salt flux balance at the interface due to fresh water release and salt flux divergence:

$$Q^S_{ice} - Q^S_w = Q^S_m. \tag{2.12}$$

Here Q^S_{ice} and Q^S_w are the diffusive salt fluxes at the interface on the ice and water sides, respectively, and Q^S_m is the advective fresh water flux associated with melting. The latter can be expressed as $Q^S_m = \rho_s V(S_{ice} - S_{int})$. The diffusive salt flux in the ice is neglected and (2.12) becomes

$$\rho_w \kappa_S \frac{\partial S}{\partial \eta}\bigg|_{\eta=0} = \rho_s V(S_{int} - S_{ice}). \tag{2.13}$$

Thus there is a balance between the diffusive flux of salt toward the ice and the advective flux of salt away from the ice face (due to the freshwater release by melting). This is in contrast to the neglect of the heat advection as discussed above. For the solutions found here we will assume that the ice is free of salt ($S_{ice} = 0$).

In the DNS we impose wall-normal velocity $u_\eta = \rho_S V/\rho_w$ [Wells and Worster, 2011] at the ice face. Effects of any mean gradient $du_\eta/d\zeta|_{\eta=0}$ (which occurs in the laminar boundary layer cases, where V is dependent on ζ) are neglected as justified

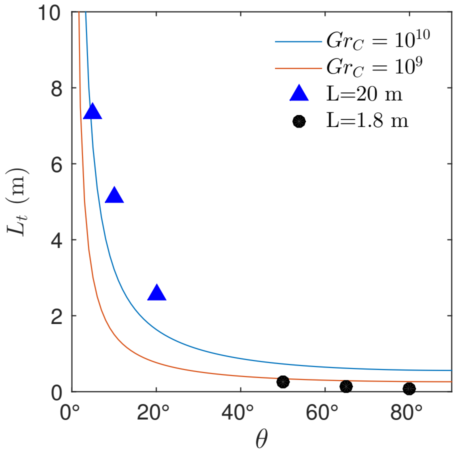

Figure 2.2: Simulated and theoretically predicted (2.14) laminar to turbulent transition length, where the prediction (curves) are based on the critical Grashof number for a vertical wall ($Gr_c^\perp = 10^9 - 10^{10}$). The simulated transition length L_t is calculated based on turbulent statistics from the simulations for $L = 1.8$ m and 20 m, respectively.

by Carey and Gebhart [1982]. Also neglected are the effects of spatial (in ζ and y) and temporal variations of $u_\zeta|_{\eta=0}$ associated with the flow fluctuations. It was verified that the DNS solutions are unchanged even when $u_\eta|_{\eta=0}$ is everywhere set to zero.

The 'open ocean' side of the computational domain is maintained as an open boundary by relaxing temperature and salinity back to its background temperature T_w and salinity S_w, respectively, through a 'sponge' region [Gayen and Sarkar, 2011] at $0.5W \leq \eta \leq W$. The along-slope, span-wise velocities and scalar fields are relaxed towards the background state in the sponge region by adding damping functions $-\sigma(\eta)u_i(\eta, y, \zeta, t)$ $(i = 2, 3)$, $-\sigma(\eta)T^*(\eta, y, \zeta, t)$ and $-\sigma(\eta)S^*(\eta, y, \zeta, t)$ to the right-hand side of the momentum and scalar equations, respectively, where $\sigma(\eta)$ is based on the time step Δt and changes from 0 at $\eta = 0.5W$ to $1/\Delta t$ s^{-1} at $\eta = W$. At the down-slope and up-slope boundaries of the domain, no-slip conditions are imposed for velocities and no-flux conditions are maintained for the temperature and salinity. Both T_{int} and S_{int} vary with location and time on the ice interface due to turbulent variations in the local heat and solute transport to the interface.

The solution is obtained using a mixed spectral/finite difference algorithm [Gayen et al., 2016]. The wall-normal and slope-parallel spatial derivatives (η and ζ) are computed with second-order finite difference. The spanwise (y) direction is considered periodic and derivatives in this direction are treated with a pseudo-spectral method. Time-stepping is accomplished with a mixed implicit/explicit strategy with all terms involving viscous contribution being stepped with the Alternating Direction Implicit (ADI) method. All the other terms are treated with a low storage 3rd order Runge-Kutta method [Gayen, 2012].

The physical dimension of the rectangular domain for one set of simulations is

$W = 0.4$ m, $D = 0.05$ m and $L = 1.8$ m. Additional simulations with the across-slope width doubled to $D = 0.1$ m, and the same W and L, show similar boundary layer properties and melt rates. Thus a width of $D = 0.05$ m is used for the remainder of the simulations for the sake of computational efficiency. A second set of solutions in a larger domain used $W = 0.4$ m, $D = 0.05$ m and $L = 20$ m. In the two domain lengths the grids have $256 \times 64 \times 1150$ and $256 \times 64 \times 1920$ points in the η, y and ζ direction, respectively. In order to resolve the salinity boundary layer and turbulent microscales for salinity, grid stretching is used in the η direction. All solutions satisfy rigorous grid resolution and grid convergence criteria that are reported in detail in Gayen et al. [2014, 2016]. Variable time stepping with a fixed Courant-Friedrichs-Lewy (CFL) number of $N_{CFL} = 0.5$ is used. The time step is calculated to be $\Delta t = (1/N_{CFL})[\Delta\eta/u_\eta, \Delta y/v, \Delta\zeta/u_\zeta]_{min}$ and varies significantly, from $O(10^{-3})$ s in the turbulent regime to $O(10^{-2})$ s in the laminar regime. The fractional step method is used to evaluate dynamic pressure at each time step [Gayen and Sarkar, 2011].

The slope angle θ is varied from 2° to 90°. In order to focus on the effect of slope on the melting process, the far-field temperature $T_w = 2.3°$ C and salinity $S_w = 35$ gkg^{-1} are fixed for all cases. All temperatures are measured with respect to the freezing point of pure water and therefore are quoted in Celsius. We fix $g = 10$ m s^{-2}, $\kappa_T = 1.285 \times 10^{-7}$ m^2 s^{-1}, $c_w = 3985$ J kg^{-1}K^{-1}, $\nu = 1.8 \times 10^{-6}$ m^2 s^{-1}, $\alpha = 6 \times 10^{-5} K^{-1}$ and $\beta = 8 \times 10^{-4}$ g^{-1}kg, taken from the physical properties of aqueous NaCl solutions at the far field temperature and salinity [Washburn, 1926; Weast et al., 1989]. We use $\kappa_S = 7.2 \times 10^{-10}$ m^2 s^{-1} at 0° C [Josberger and Martin, 1981] with a resultant $Sc = 2500$ at grid points adjacent to the interface. In the interior we use $\kappa_S = 3.6 \times 10^{-9}$ m^2 s^{-1} [$Sc = 500$, Gayen et al., 2016] in order to make the turbulence simulations feasible. The Prandtl number is fixed at $Pr = 15$ throughout the domain. The primary solution sets are designed to cover the range of slope angles for both $Gr = 7.5 \times 10^{11}$ (for a domain length of 1.8 m) and $Gr = 10.28 \times 10^{14}$ (domain length of 20 m).

The critical Grashof number for transitions from laminar to turbulent flow on a vertical wall varies from $Gr_c^\perp \sim 10^9 - 10^{10}$[Holman, 2010; Josberger and Martin, 1981; Turner, 1979]. A first approximation for the critical along-slope distance L_c beyond which the boundary layer becomes turbulent, based on the critical vertical height $L_c^\perp$, is

$$L_c \approx \frac{L_c^\perp}{\sin\theta} = \frac{1}{\sin\theta}\left(\frac{\nu^2 Gr_c^\perp}{g\beta\Delta S}\right)^{1/3}, \tag{2.14}$$

giving a critical Grashof number for the sloping interface as

$$Gr_c \approx \frac{Gr_c^\perp}{(\sin\theta)^3}. \tag{2.15}$$

Based on this assumption we calculated the transition length for various slope angles bounding the previously established critical $Gr_c^\perp$ (figure 2.2) and plotted the laminar to turbulent transition length (L_c) given by the DNS, where L_c is defined as the height where spanwise fluctuations (v_{rms}) reach 10% or more of the average up-slope flow. The results show that the along-slope length required to achieve turbulence increases rapidly with decreasing slope angles. Hence we require the longer domain of 20 m in order to simulate turbulent conditions under sloping ice at $\theta \leq 20°$.

2.3 Scaling Analysis

Ablation of the ice face takes place when it is in contact with saline water with a temperature greater than the melting temperature. The addition of melt water to the saline water results in freshening of a layer adjacent to the ice and gives rise to a buoyant boundary layer plume. Working from the momentum and solute transport equations the plume can be divided into multiple layers (figure 2.3) based on the dominant balances discussed below. The buoyancy force is important only within a solutal boundary layer at the ice face, of thickness δ_S, and we refer to this as the 'inner layer'. Diffusion or turbulent advection of heat in the wall-normal direction is important within a thermal boundary layer of thickness δ_T. However, the thermal buoyancy is relatively small and does not enter the momentum balance at leading order. In the inner layer, solutal buoyancy and stress are the dominant terms in the momentum equation. Outside the inner boundary layer there is an outer layer, of thickness δ_0, in which buoyancy forces make a negligible contribution.

When the flow is laminar the whole of the inner layer will be dominated by the balance of buoyancy with molecular viscous stress, and by molecular diffusion of heat and solute toward the ice, as previously described in the context of a vertical ice face [Wells and Worster, 2011]. The laminar outer layer is governed by an inertia-viscous balance. That analysis is adapted here (Section 3.1) to a sloping ice face. We find that this laminar solution may have geophysical relevance for very small ice slopes, as a consequence of a stabilising density stratification produced by the melting.

When the plume is turbulent, small-scale eddies add significantly to momentum transport in the wall-normal direction within the buoyant inner layer, leaving a much thinner laminar and diffusive sublayer (of thickness δ_{sub}) on the ice face. Within the sub-layer eddy transport and turbulent kinetic energy production are negligible. The smallness of the sub-layer thickness is confirmed by the DNS solutions reported here, which show it to be O(10) times smaller than the inner layer thickness δ_S. In the inner layer the dominant momentum balance is between the solutal buoyancy and Reynolds stress. However, scaling indicates that the molecular diffusion of solute toward the ice remains a dominant term in the salt budget. In the outer layer the turbulent plume is dominated by Reynolds stress and turbulent transport of solute, leaving the solute relatively well mixed, which in turn implies a negligible molecular transport of solute. Molecular diffusion of heat can remain important throughout a region of thickness δ_T, which may overlap the outer inertial layer. Ambient fluid is entrained into the turbulent plume from the edge of the outer layer. The layers defined here are consistent with a model previously proposed for thermal convection

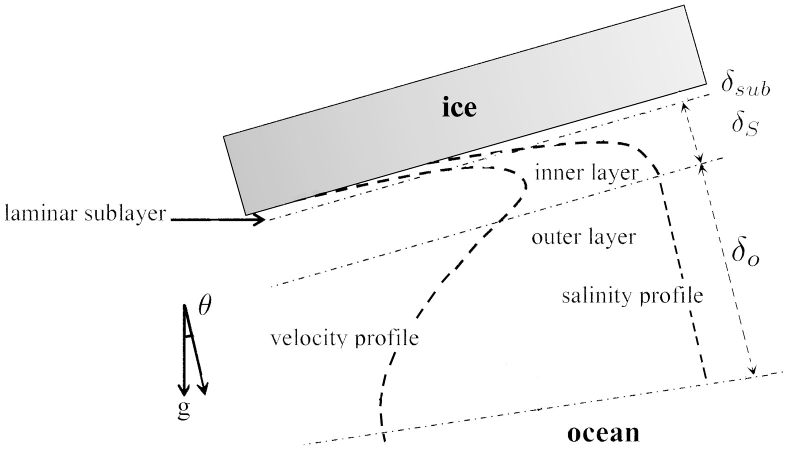

Figure 2.3: Schematic of the theoretical model boundary layer structure, with up-slope velocity and solute concentration profiles in the wall-normal direction, for the case of a turbulent plume (thicknesses not to scale).

at a heated vertical boundary [Wells and Worster, 2008]. In the following sub-sections the thicknesses of the sloping inner solutal layer and thermal boundary layer, and the ablation rate, are analysed for laminar and turbulent cases.

2.3.1 Laminar Boundary layer flows: viscous-buoyancy balance

Wells and Worster [2011] derived similarity solutions for melting and dissolving with a laminar boundary layer for a vertical ice face and quiescent far field[1] In the inner layer δ_S and $\mathcal{L}$ are the characteristic length scales for the wall normal and the along slope directions, respectively, whereas δ_0 and $\mathcal{L}$ are characteristic length scales associated with the outer layer. At small Grashof numbers ($Gr < Gr_c$) or shallow slopes, the inertia terms inside the diffusive boundary layer are negligible, leaving a balance between viscous drag and buoyancy in the up-slope flow in the momentum equations (4.2-2.4). The buoyancy is predominantly supplied by the salinity anomaly (ΔS) across the diffusive boundary layer:

$$\nu \frac{\partial^2 U_\zeta}{\partial \eta^2} \sim \nu \frac{U_\zeta}{\delta_S^2} \sim g \sin\theta \; \beta \Delta S. \tag{2.16}$$

The scaling of the viscous terms in (2.16) holds for large Sc, as the inflection in the up-slope velocity profile must lie outside the buoyancy driven inner layer. The wall-normal derivatives in the boundary layer are the dominant contributions (ie. $\partial/\partial\eta \gg \partial/\partial\zeta$ as $\delta_S \ll \mathcal{L}$) to both the viscous drag and the diffusion of solute. Outside the solutal diffusive boundary layer the buoyancy force is neglected and hence the inertia in the outer layer balances the residual viscous drag force generated by the up-slope flow [Nilson, 1985]. This leads to

---

[1] The final form of the similarity solution for the case of dissolution of a solute at a vertical wall was also quoted by Husband and Ozsahin [1967]. Here we summarise their solution for the case of dissolving and extend it to sloping ice faces. However, for brevity we use simple scaling arguments, which also assist in contrasting the dynamics of laminar and turbulent cases.

$$\frac{U_\zeta^2}{\mathcal{L}} \sim \nu \frac{U_\zeta}{\delta_0^2}. \tag{2.17}$$

The convective salt transport by mean flow in (4.4) balances solute diffusion through the inner boundary layer:

$$U_\zeta \frac{\Delta S}{\mathcal{L}} \sim U_\eta \frac{\Delta S}{\delta_S} \sim \kappa_S \frac{\Delta S}{\delta_S^2}. \tag{2.18}$$

Here total velocity $u_i = U_i + u_i'$ is decomposed into the mean boundary layer flow U_i and fluctuating velocity component u_i' with the latter assumed to play a negligible role for laminar flow. We also assume that the salinity anomaly in the along-slope direction is equivalent to the salinity difference across the boundary layer. Combining (2.16) and (2.18) leads to the scaling of the thickness of the solutal boundary layer as

$$\delta_S \sim \delta_{S0} (\sin\theta)^{-\frac{1}{4}}, \tag{2.19}$$

where δ_{S0} is the salinity boundary layer thickness for the case of a vertical ice face

$$\delta_{S0} \sim \left(\frac{\nu \kappa_S \mathcal{L}}{g \beta \Delta S} \right)^{\frac{1}{4}}, \tag{2.20}$$

or equivalently,

$$\frac{\delta_{S0}}{\mathcal{L}} \sim Gr_{\mathcal{L}}^{-1/4} Sc^{-1/4}, \tag{2.21}$$

with the local Grashof number $Gr_{\mathcal{L}} = g\beta\Delta S \mathcal{L}^3/\nu^2$ (which is based on the up-slope distance $\mathcal{L}$). From (2.13) the ablation rate can be estimated as $V \sim (\rho_w \kappa_S \Delta S)/(\rho_S S_{int} \delta_S)$, which gives

$$V \sim V_0 (\sin\theta)^{1/4}, \tag{2.22}$$

where V_0 is the ablation rate for a vertical ice face given by

$$V_0 \sim \frac{\rho_w \Delta S}{\rho_S S_{int}} \left(\frac{g \beta \Delta S \kappa_S^3}{\nu} \right)^{1/4} \mathcal{L}^{-1/4}, \tag{2.23}$$

or

$$\frac{V_0 \mathcal{L}}{\kappa_S} \sim \left(\frac{\rho_w \Delta S}{\rho_S S_{int}} \right) Gr_{\mathcal{L}}^{1/4}. \tag{2.24}$$

This scaling predicts that the ablation rate decreases in the up-slope direction as $\zeta^{-1/4}$, consistent with dissolution by laminar flow on a vertical ice face ($\theta = \pi/2$)

found by Wells and Worster [2011]. It also predicts that ablation rate decreases with slope angle as $(\sin\theta)^{1/4}$. Considering the diffusive heat transport in the thermal boundary layer, the ablation rate from (4.6) must satisfy

$$V \sim -\frac{\rho_w c_w \kappa_T \Delta T}{\rho_S L_f \delta_T}. \tag{2.25}$$

Equating (2.25) and (2.22), the thermal boundary layer thickness δ_T can then be expressed as

$$\delta_T \sim \delta_{T0}(\sin\theta)^{-\frac{1}{4}}, \tag{2.26}$$

where the thermal boundary layer thickness δ_{T0} for the case of a vertical ice face is

$$\delta_{T0} \sim \frac{c_w \kappa_T S_{int}}{\kappa_S L_f} \frac{\Delta T}{\Delta S} \left(\frac{\nu \kappa_S \mathcal{L}}{g \beta \Delta S} \right)^{\frac{1}{4}}, \tag{2.27}$$

or in dimensionless form

$$\frac{\delta_{T0}}{\mathcal{L}} \sim \left(\frac{\rho_S}{\rho_w} \frac{S_{int}}{\Delta S} \right) St Le Gr_{\mathcal{L}}^{-1/4} Sc^{-1/4}. \tag{2.28}$$

Here $Le = \kappa_T / \kappa_S$ is the Lewis number. The thermal boundary layer thickness shows a similar dependence on the up-slope distance and slope angle as does the solutal boundary layer (2.20, 2.21). Scaling of the outer inertial layer thickness δ_0 (using 2.17 and 2.20) becomes

$$\frac{\delta_0}{\mathcal{L}} \sim Sc^{1/2} \frac{\delta_S}{\mathcal{L}} \sim Gr_{\mathcal{L}}^{-1/4} Sc^{1/4}, \tag{2.29}$$

and this too increases with up-slope distance in the same manner as the inner layer thickness.

2.3.2 Turbulent boundary layer flows: boundary layer inertia-buoyancy balance

At large Gr the boundary layer becomes unstable to both buoyancy- and shear-driven instabilities, leading to small scale motions [Holman, 2010; Josberger and Martin, 1981; Gayen et al., 2016]. In the outer layer diffusive transport is negligible and there is a balance in (4.4) between advection of solute by the mean flow and turbulent solute transport, leading to

$$\frac{U_\zeta \Delta S}{\mathcal{L}} \sim \frac{\overline{u'S'}}{\delta_0}. \tag{2.30}$$

In the inner layer there is potentially a regime, at intermediate Gr, in which turbulent transport of solute dominates over molecular transport while viscous stress remains important relative to Reynolds stress. However, here we consider a regime at very large Gr, in which Reynolds stresses $\overline{u_i'u_j'}$ produced by the small scale motions dominate over the viscous stress and establish a dominant balance with local buoyancy in the inner layer. Thus we assume

$$\frac{\partial}{\partial \eta}\overline{u_\eta' u_\zeta'} \sim \frac{u_\eta'^2}{\delta_S} \sim g \sin\theta \; \beta \Delta S \tag{2.31}$$

along with local isotropy ($u_\eta' \sim u_\zeta' \sim v'$).

For this turbulent case small scale fluctuations contribute to solute transport in the inner layer and the mean convective transport in the wall-normal direction becomes relatively small, as indicated by the ratio of terms $(\overline{u'S'}/\delta_S)/(U_\zeta \Delta S/\mathcal{L}) \sim \delta_0/\delta_S \gg 1$ (using 2.30). This is consistent with previous studies of natural thermal convection at a heated vertical boundary [George Jr and Capp, 1979; Tsuji and Nagano, 1988; Wells and Worster, 2008]. The solute transport by fluctuations balances, to leading order, the diffusive transport of salt giving

$$\frac{\partial \overline{u_\eta' S'}}{\partial \eta} + \frac{\partial \overline{u_\zeta' S'}}{\partial \zeta} \sim \kappa_S \frac{\partial^2 S}{\partial \eta^2}, \tag{2.32}$$

or in scaled form

$$\frac{\overline{u_\eta' S'}}{\delta_S} \sim \kappa_S \frac{\Delta S}{\delta_S^2}, \tag{2.33}$$

where S' is the salinity fluctuation and $\partial/\partial\eta \gg \partial/\partial\zeta$. For a vertical ice face the fluctuations in the salinity field S' and density field ρ' scale with ΔS and $\Delta\rho$ and (2.31, 2.33) lead to the turbulent inner layer thickness and ablation rate:

$$\delta_{S0} \sim \left(\frac{\kappa_S^2}{g\beta\Delta S}\right)^{1/3} \quad \text{and} \quad V_0 \sim \frac{\rho_w \Delta S}{\rho_s S_{int}} \left(g\beta\Delta S \kappa_S\right)^{1/3}. \tag{2.34}$$

Kerr and McConnochie [2015] reported scaling for the ablation velocity in this vertical case having this same dependence on buoyancy, $V_0 \sim (g\beta\Delta S)^{1/3}$, but different molecular dependences, $V_0 \sim (\kappa_S^2/\nu)^{1/3}$. The present scaling neglects the effect of viscosity, which is assumed small compared with the Reynolds stress in the inner layer.

When the ice face is inclined, the fresh water flux due to ablation generates stratification, which inhibits the turbulent fluctuations. Hence, salinity fluctuations S' cannot directly scale with salinity anomaly ΔS across the boundary layer. Another independent equation is required to solve for S'. We assume that the mean density gradient in the inner stratified layer scales with $\Delta\rho/\delta_S$ and the frequency of turbulent fluctuations (the eddy turnover rate $1/\Delta t$) scales with the buoyancy frequency

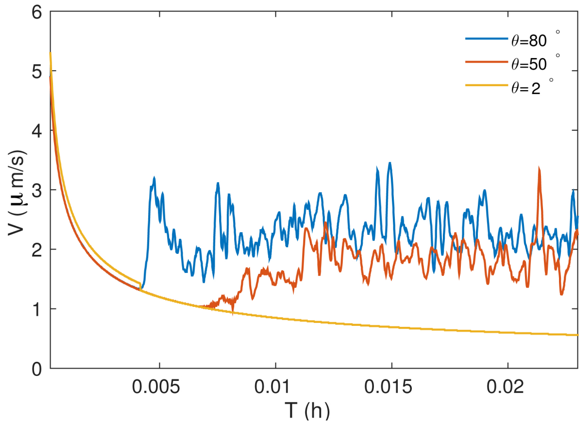

Figure 2.4: Temporal evolution of ablation rate ($\mu m/s$) measured at the mid-length for slope angle θ, = 2°, 50° and 80° in the 1.8 m domain.

N. Hence $\Delta t \sim 1/N \sim [\rho_0 \delta_S / g\Delta\rho]^{1/2}$, where $N^2 = -(g/\rho_0) d\rho/dz \sim (g/\rho_0)\Delta\rho/\delta_S$. This leads to a simple linearised equation for density fluctuation:

$$\frac{\partial \rho'}{\partial t} \sim u'_\eta \frac{\partial \overline{\rho}}{\partial \eta} \qquad \rightarrow \qquad \frac{\rho'}{\Delta t} \sim \frac{u'_\eta \Delta\rho}{\delta_S}. \tag{2.35}$$

These assumptions may not hold for near-vertical ice faces, where the effect of local stratification becomes negligible. Substituting the timescale in (2.35), the density and salinity fluctuations ($S' \sim \rho'/\beta\rho_0$) become

$$\rho' \sim u_\eta{}' \sqrt{\frac{\Delta\rho\rho_0}{g\delta_S}}, \qquad S' \sim u_\eta{}' \sqrt{\frac{\Delta S}{g\beta\delta_S}}. \tag{2.36}$$

From (2.31), (2.33) and (2.36) the salinity fluctuations scale as

$$S' \sim \Delta S(\sin\theta)^{1/2} \tag{2.37}$$

and the solutal boundary layer thickness becomes

$$\delta_S \sim \delta_{S0}(\sin\theta)^{-2/3}, \tag{2.38}$$

where δ_{S0} is again the inner solutal layer thickness for the case of a vertical ice face, this time for turbulent convection. In dimensionless form:

$$\frac{\delta_{S0}}{\mathcal{L}} \sim Gr_{\mathcal{L}}^{-1/3} Sc^{-2/3}. \tag{2.39}$$

Hence δ_{S0} and δ_S are independent of up-slope distance. From (2.13) the ablation velocity becomes

$$V \sim V_0 (\sin\theta)^{2/3}, \tag{2.40}$$

where the ablation velocity (2.34) for a vertical ice face is

$$\frac{V_0 \mathcal{L}}{\kappa_S} \sim \left(\frac{\rho_w \Delta S}{\rho_S S_{int}}\right) Gr_{\mathcal{L}}^{1/3} Sc^{2/3}. \tag{2.41}$$

Thus ablation rates too are predicted to be independent of distance up the slope. Ablation decreases with decreasing slope angle as $(\sin\theta)^{2/3}$.

Using (4.6) and (2.40) we solve for the thermal boundary layer thickness

$$\delta_T \sim \delta_{T0} (\sin\theta)^{-2/3}, \tag{2.42}$$

where for the vertical case

$$\delta_{T0} \sim \frac{c_w \kappa_T S_{int}}{\kappa_S L_f} \frac{\Delta T}{\Delta S} \left(\frac{\kappa_S^2}{g\beta\Delta S}\right)^{1/3}, \tag{2.43}$$

or

$$\frac{\delta_{T0}}{\mathcal{L}} \sim \left(\frac{\rho_S S_{int}}{\rho_w \Delta S}\right) St^{-1} Le Gr_{\mathcal{L}}^{-1/3} Sc^{2/3}. \tag{2.44}$$

Like the inner solutal boundary layer, the inner thermal boundary layer has thickness independent of distance up the slope.

The outer layer scaling can be established independently using turbulent entrainment parameterisation. Continuity (4.1) for the mean flow in the outer layer shows

$$\frac{U_\zeta}{\mathcal{L}} \sim \frac{U_\eta}{\delta_0}. \tag{2.45}$$

The mean normal velocity U_η is equivalent to the entrainment velocity and is assumed to be linearly proportional to the up-slope velocity, $U_\eta \sim E U_\zeta$, where E is the entrainment coefficient [Morton et al., 1956]. This leads to

$$\delta_0 \sim E\mathcal{L}. \tag{2.46}$$

Similar scaling was suggested for the outer layer in the case of natural thermal convection at a heated vertical boundary [Wells and Worster, 2008], for turbulent wall plumes driven by a uniformly distributed wall buoyancy flux [Cooper and Hunt, 2010] and also for the melt boundary layer at a vertical ice wall [Kerr and McConnochie, 2015; Gayen et al., 2016]. Under an inclined ice face E is likely to be dependent on the slope angle, potentially following the result of Ellison and Turner [1959] for a dense plume flowing down a sloping boundary. For our case of melting of a sloping ice face, the result is an outer layer thickness (the overall region of

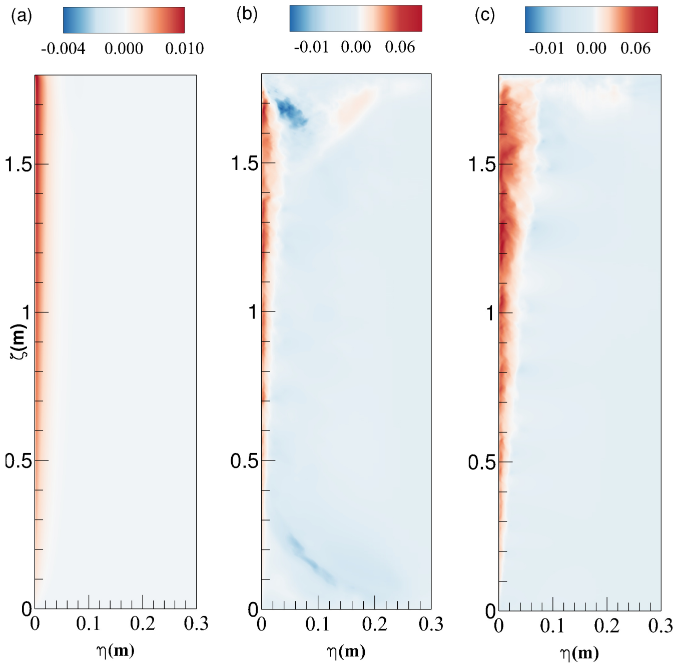

Figure 2.5: Snapshots of the up-slope velocity u_ζ (colour scale in m/s) on a vertical $\zeta - \eta$ plane normal to the ice face for slopes (a) $\theta = 2°$, (b) 50° and (c) 80°, respectively, with $L = 1.8$ m.

turbulent flow) that grows linearly with distance up the slope.

2.4 Results

All simulations were initiated with uniform temperature and salinity. White noise was imposed in the velocity field and concentrated near the interface. The initial ablation rate is large, as shown in figure 2.4, but it quickly slows down and reaches a statistically steady value. In the steady state, for most of cases, high frequency variations are observed in the ablation rates and the interface temperatures (not shown here), as a result of turbulent fluctuations inside the boundary layer. The time to reach steady state decreased with increasing slope angle (figure 2.4). For the laminar boundary layer at $\theta = 2°$ temporal variability is absent and the simulation takes significantly longer to reach a steady state. The steady state ablation rate decreases with decreasing slope.

Snapshots of the up-slope velocity for the 1.8 m and 20 m domains are shown in figures 2.5 and 2.6, respectively. Snapshots of the temperature and salinity field for a 1.8 m domain are shown in figure 2.7a and 2.7b, respectively. Buoyant water with low salinity is released from the interface and forms a very thin boundary layer (figure 2.7b) with up-slope flow adjacent to the ice face. At the same time, a cooled outer boundary layer forms with downslope flow extending far beyond the inner salinity boundary layer (figure 2.7a). This bi-directional flow was previously predicted for a

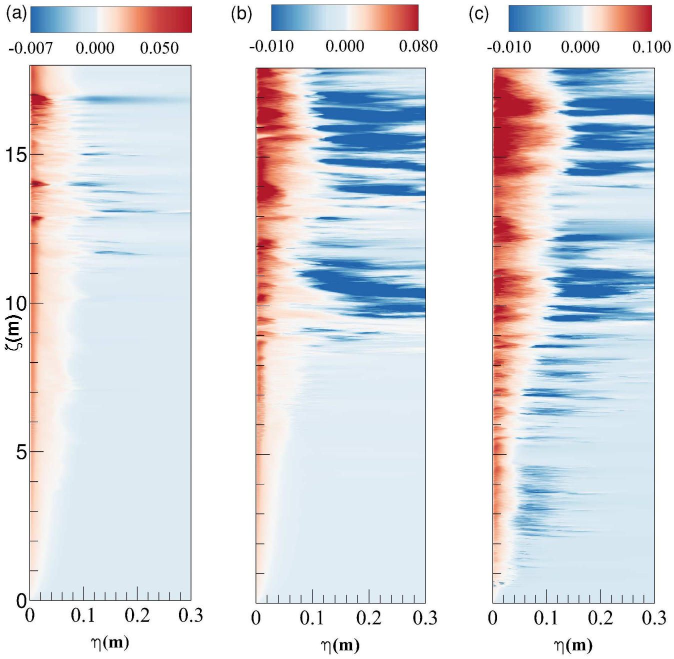

Figure 2.6: Similar to figure 2.5, up-slope velocity u_ζ (colour scale in m/s) for (a) θ = 5°, (b) θ = 10° and (c) θ = 20°, respectively, for $L = 20$ m. The slope-normal distance η is enlarged by approximately 10 times relative to the slope-parallel scale in order to more clearly show the structure in the boundary layer.

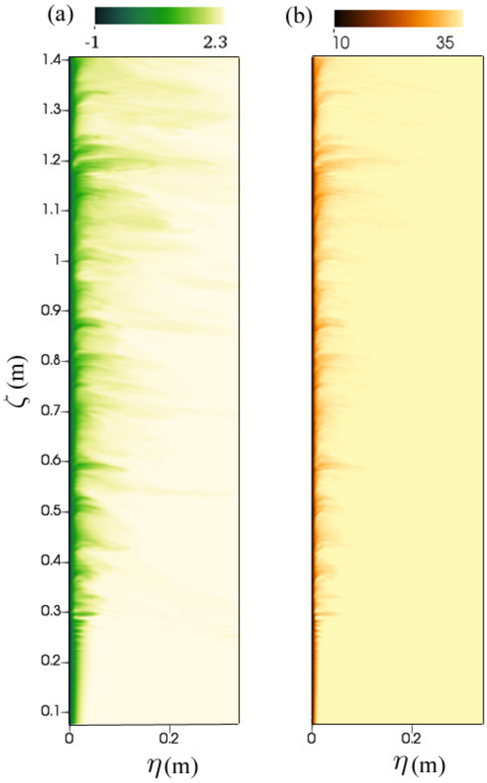

Figure 2.7: Snapshots of (a) temperature T (°C) and (b) salinity S (gkg^{-1}) fields for $\theta = 50°$.

vertical ice face [Nilson, 1985], and was found in laboratory experiments [Josberger and Martin, 1981; Kerr and McConnochie, 2015] and numerical simulations [Gayen et al., 2016]. The inner boundary flow accelerates with up-slope distance from the bottom of the domain and at the same time spreads outward due to laminar diffusion and turbulent entrainment of the quiescent ambient fluid. Flow structures inside the boundary layer are similar for turbulent cases at different slope angles.

For a given slope length the buoyancy force in the along-slope direction decreases with decreasing boundary slope, resulting in weaker up-slope flow. The wall-normal component of buoyancy keeps the up-slope plume in contact with the wall and tends to separate it from the down-slope flow (as shown in figure 2.5b). For the domain length of $L = 1.8$ m with slope angle $\theta \leq 30°$, the effective Grashof number is smaller than the the critical Grashof number ($Gr^{\perp} < Gr_c^{\perp}$) and the flow field is expected to be laminar. However, in the 20 m domain the flow is turbulent even for slopes as small as $\theta = 5°$ (figure 2.6a).

In figure 2.8a the ablation rates are compared for laminar and turbulent cases in the smaller domain (slopes $\theta = 30°$ and $\theta = 80°$). For $\theta = 80°$ a maximum ablation rate is observed around $\zeta = 0.05 - 0.075$ m from the bottom boundary, which is where transition from laminar to turbulent flow takes place. Above this transition region the turbulent ablation rate becomes statistically invariant with the along-slope

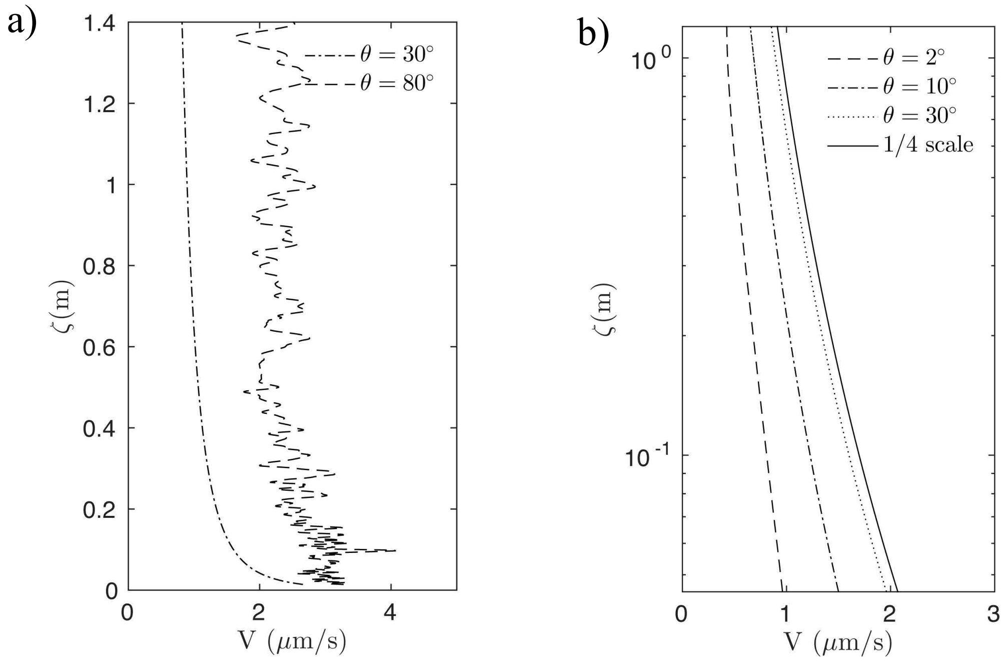

Figure 2.8: (a) Along-slope profiles of instantaneous laminar ($\theta = 30°$) and turbulent ($\theta = 80°$) dissolution rates. (b) Instantaneous laminar dissolution rates for $\theta = 2°$, 10° and 30°, respectively, as a function of along-slope distance (in logarithmic scale) for $L = 1.8$ m, along with the theoretical 1/4 scaling (2.22) for laminar ablation rate for an arbitrary slope angle (continuous line). Values are taken after the flow field reaches quasi-steady state.

distance. Similar observations were reported in laboratory experiments [Josberger and Martin, 1981; Kerr and McConnochie, 2015] and DNS of the vertical case [Gayen et al., 2016]. For $\theta = 30°$ the entire boundary layer is laminar (for $L = 1.8$ m) and the ablation rate decreases with along-slope distance. In order to estimate the power law relation of the ablation rate and along-slope distance, the ablation rates for $\theta = 2°, 10°$ and 30° are plotted as a function of distance up-slope on a logarithmic scale (figure 2.8b). Consistent with the theoretical estimation in (2.22), the laminar ablation rates decrease with up-slope distance as $\zeta^{-1/4}$.

Time-averaged ablation rates at mid-length are shown in figure 2.9a, where the rates are averaged over 8-10 turnover times τ_b at statistically steady state. Here, $\tau_b = \left[L/g\beta\Delta S\right]^{1/2}$ is calculated based on the effective domain length L and characteristic velocity scale $[g\beta\Delta SL]^{1/2}$. Both laminar and turbulent ablation rates monotonically increase with the slope angle. The turbulent ablation rates are more sensitive to the ice face inclination than are the laminar rates. The laminar cases show a $(\sin\theta)^{1/4}$ dependence (2.22), whereas turbulent ablation rates follow a $(\sin\theta)^{2/3}$ dependence (figure 2.9b). Both of these behaviours are predicted by the theoretical scaling in

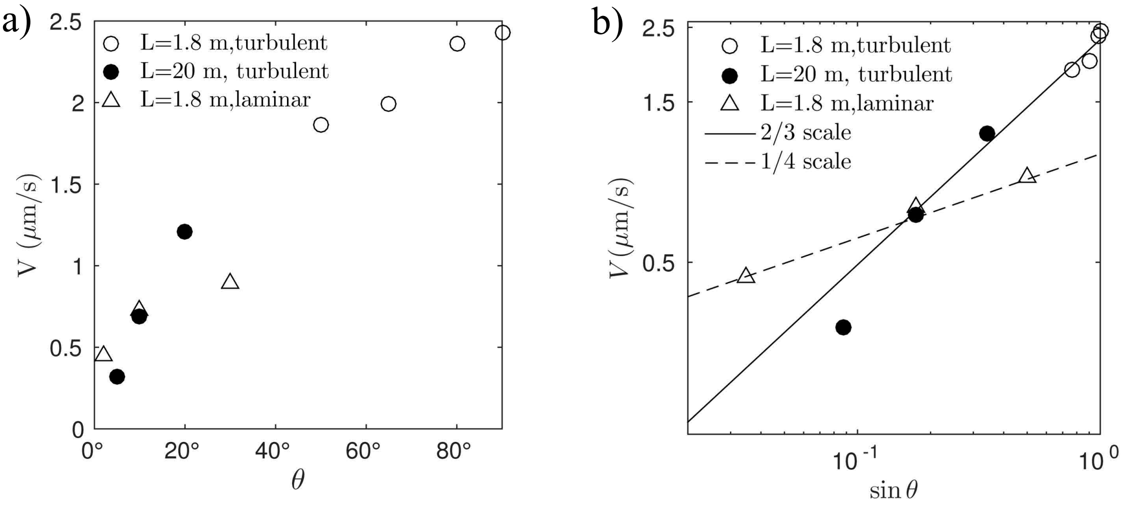

Figure 2.9: Time averaged ablation rates at mid-length as functions of (a) slope angle θ and (b) $\sin\theta$. In (b) scales are logarithmic. Lines show the predicted $1/4$ (dashed line) and $2/3$ (solid line) power laws as predicted by (2.22) and (2.40). • turbulent boundary layer with $L = 1.8$ m; ∘ turbulent boundary layer with $L = 20$ m, △ laminar boundary layer with $L = 1.8$ m.

(2.22) and (2.40). In figure 2.10a we plot the thermal boundary layer thickness (δ_T) as a function of slope angle, where δ_T is measured as the temperature e-folding distance from the ice-water interface. The measured boundary layer thickness increases with decreasing slope angle, with trends again depending on whether the boundary layer is laminar or turbulent. The thickness of the thermal boundary layer for laminar flow increases as $(\sin\theta)^{-1/4}$ (figure 2.10b). For turbulent flow the layer thickness is more sensitive to the slope angle and approximately follows $(\sin\theta)^{-2/3}$. Both behaviours are again consistent with the theoretical scaling in (2.26) and (2.42). The corresponding thickness of the salinity boundary layer (figure 2.11) behaves in an identical fashion and is approximately one half of the thermal boundary layer thickness.

The wall-normal advective buoyancy flux ($gu_\eta\rho^*/\rho_0$) based on wall-normal velocity u_η and density anomaly ρ^* is shown in figure 2.12a. Though the wall-normal buoyancy flux shows significant spatial variability associated with strong turbulent patches, the averaged value is negative. The magnitude of the averaged advective buoyancy flux shows increasing magnitude with the slope angle as $(\sin\theta)^{2/3}$ (see figure 2.12b). The ablation rate is also coupled to the net transport of buoyancy across the boundary layer. Hence the trend in buoyancy flux with slope angle is consistent with the change in ablation rate with slope angle as shown in (2.40). Under the conditions used here, the turbulent advection ($g\langle {u_\eta}'\rho'/\rho_0\rangle$) accounts for more than 80% of the total advective buoyancy flux in the wall-normal direction. The scaling (2.40) for transport can be compared with previous experiments for turbu-

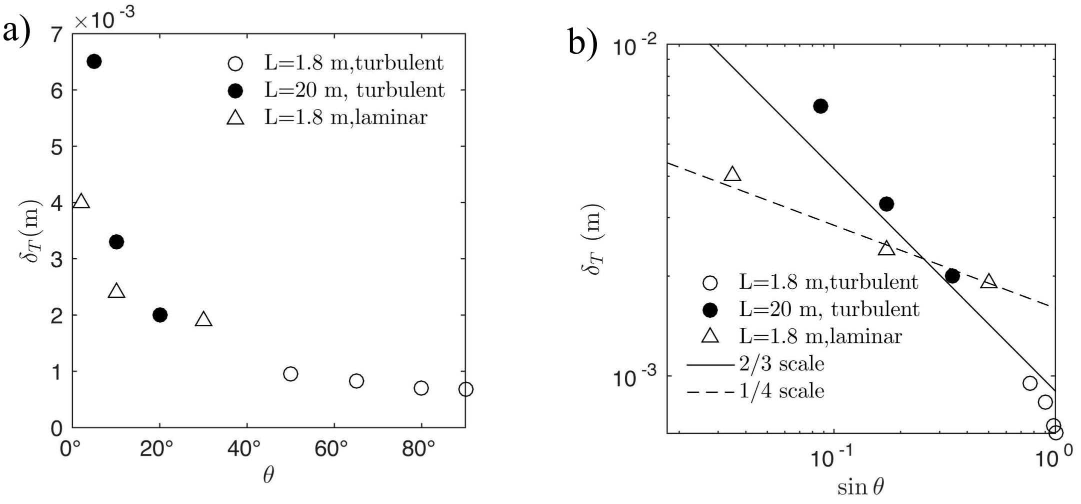

Figure 2.10: Thermal boundary layer thickness δ_T (m) as a function of (a) slope angle θ and (b) $\sin\theta$ (scales are logarithmic). Solid and dotted line show the predicted scaling, (2.26) and (2.42), respectively. Symbols as in figure 2.9.

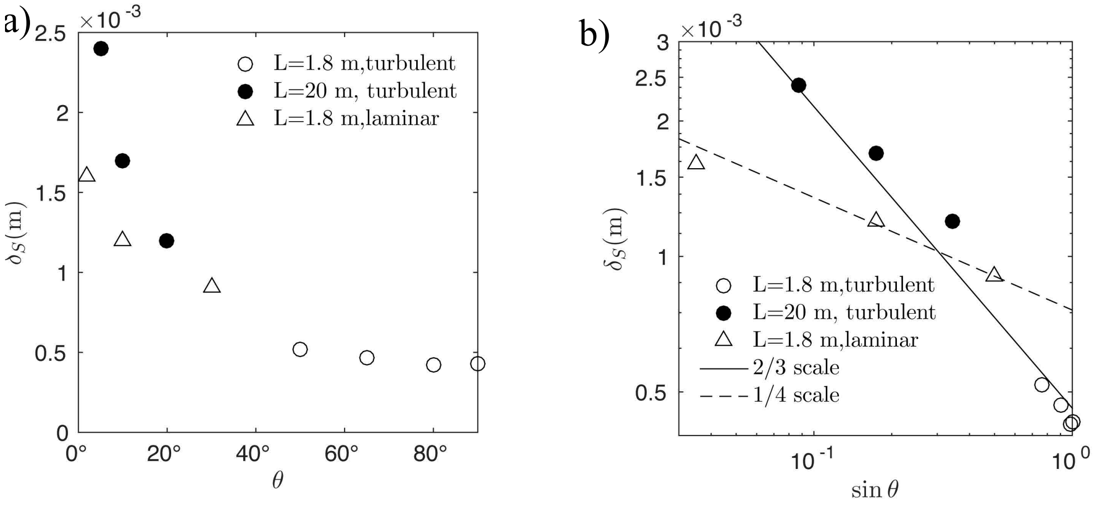

Figure 2.11: Salinity boundary layer thickness δ_S (m) as function of (a) slope angle θ and (b) $\sin\theta$ (scales are logarithmic). Solid and dotted line shows the predicted scaling of (2.19) and (2.38), respectively. Symbols as in figure 2.9.

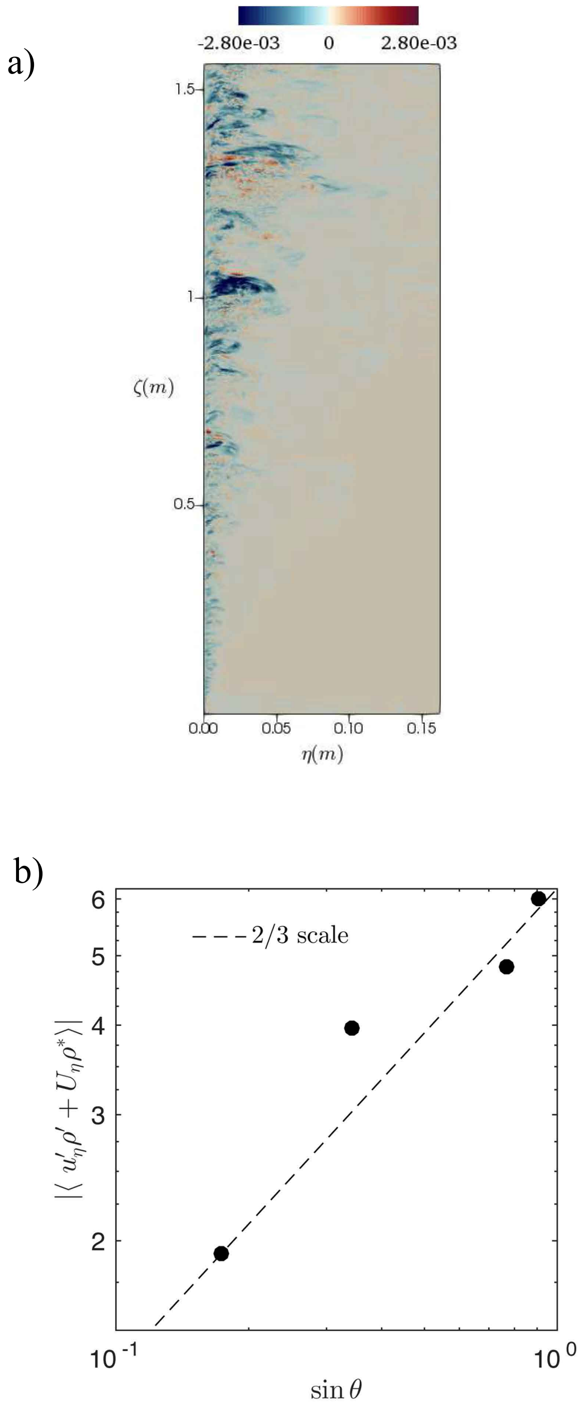

Figure 2.12: (a) Snapshot of slope-normal advective buoyancy flux (sum of mean ($U_\eta \rho^*$) and turbulent ($u'_\eta \rho'$) advective fluxes in kg $\mathrm{s}^{-1}/\mathrm{m}^2$), for $L = 1.8$ m and $\theta = 80°$, (b) Absolute value of time- and area-averaged total wall-normal buoyancy flux as a function of $\sin\theta$, where the real values are negative; scales are logarithmic. In (a) the slope-normal distance is enlarged by approximately 10 times relative to the slope-parallel scale in order to show the structure inside the boundary layer. In (b) the dashed line has slope 2/3. The averaging is over a period $\tau \sim 10\tau_b$ and across the thickness of the velocity boundary layer.

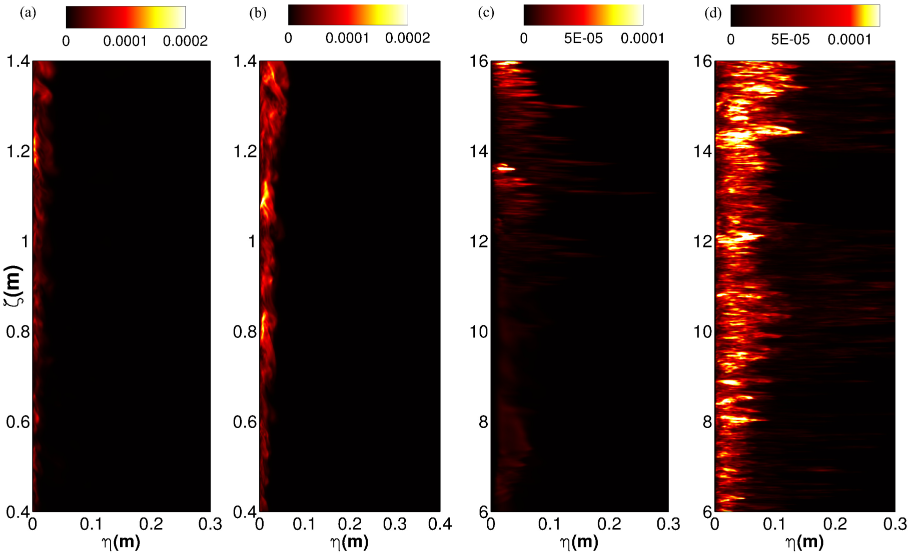

Figure 2.13: The instantaneous distribution of turbulent kinetic energy, K (colour scale in $\mathrm{m}^2/\mathrm{s}^3$) in turbulent boundary layers for slope angle (a) $\theta = 50°$ and (b) $\theta = 90°$ for $L = 1.8$ m and (c) $\theta = 5°$ and (d) $\theta = 20°$ for $L = 20$ m. A middle portion of the domain (the actively turbulent region) is shown and in (c) and (d) the slope-normal distance is enlarged by approximately 10 times relative to the slope-parallel scale in order to more clearly show the turbulent activity in the boundary layer.

lent natural convection beneath a forward facing inclined heated plane [Vliet, 1969], where uniform heat flux was imposed over the whole plane. In that case, the heat transfer coefficient, Nu (the normalised heat transport), varies as the 1/4 power of the flux Grashof number, Gr^*_F. This is effectively the 1/3 power of the Grashof number based on the temperature difference ΔT and modified gravity $g^* = g(\sin\theta)^2$ (where $Gr^* = g^*\alpha\Delta T L^3/\nu^2$ and the extra $\sin\theta$ dependence is due to stratification). The result therefore suggests the heat transfer coefficient in that thermal convection problem follows $Nu \sim (\sin\theta)^{2/3}$, as is observed here for the solutal flux.

The turbulent kinetic energy (K), denoted by $K = (1/2)u_i'u_i'$ with index representing η, y and ζ directions, is the energy associated with the fluctuating motions in the boundary layers. The fluctuating (primed) component $u_i' = u_i - U_i$, is calculated using spanwise spatial average U_i. The turbulent kinetic energy budget can be expressed as

$$\frac{\partial K}{\partial t} + u_j\frac{\partial K}{\partial x_j} = P - \varepsilon + B - \frac{\partial \Gamma}{\partial x_j}, \tag{2.47}$$

where P is the turbulent shear production

$$P = -\overline{u_i'u_j'}\frac{\partial U_i}{\partial x_j}, \tag{2.48}$$

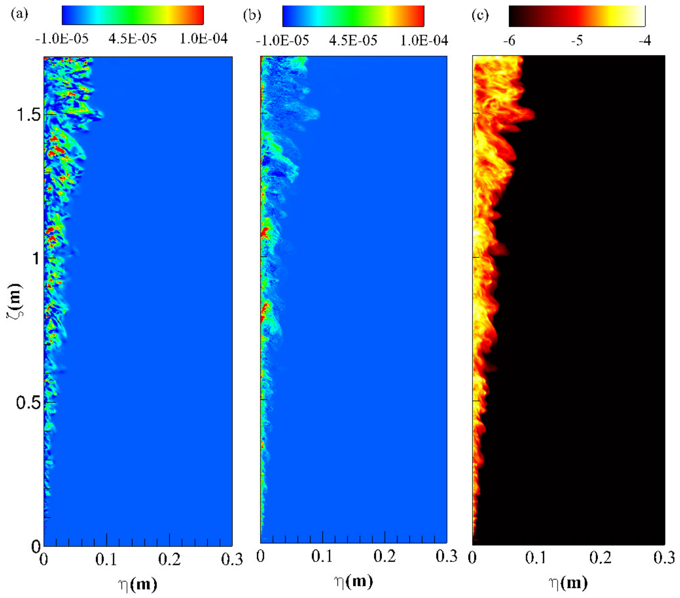

Figure 2.14: Snapshot of rates of (a) turbulent shear production, P ($\mathrm{m}^2/\mathrm{s}^3$), (b) buoyancy production B ($\mathrm{m}^2/\mathrm{s}^3$) and (c) viscous dissipation, ε (expressed in a logarithmic colour scale) for $\theta = 90°$ in 1.8 m domain.

ε is the turbulent dissipation

$$\varepsilon = \nu \overline{\frac{\partial u_i'}{\partial x_j} \frac{\partial u_i'}{\partial x_j}}, \tag{2.49}$$

B is the turbulent buoyancy production

$$B = -g\overline{\rho' u_\zeta'} \sin\theta + g\overline{\rho' u_\eta'} \cos\theta, \tag{2.50}$$

and the term $\partial\Gamma/\partial x_j$ denotes the turbulent advection of K,

$$\Gamma \equiv p' u_i' + \frac{1}{2}\overline{u_i' u_i' u_j'} - \nu \frac{\partial K}{\partial x_j}, \tag{2.51}$$

containing the pressure transport, turbulent transport and viscous transport.

Snapshots of K for the shorter and longer domain are shown in figure 2.13a, 2.13b and 2.13c, 2.13d respectively. For all cases K increases in the up-slope direction and the boundary layer thickens. For a given slope length, K is larger for the steeper ice faces. For the smaller slope, turbulence develops further along the ice interface (figure 2.13c and 2.13d).

The instantaneous turbulent shear production rate P, buoyancy production rate B, and viscous dissipation rate ε are shown in figure 2.14 for the steepest ($\theta = 90°$) ice face and in figure 2.15 for a small slope angle ($\theta = 10°$). The turbulent dissipation rate is always maximum at the ice face at all distances along the slope. A significant

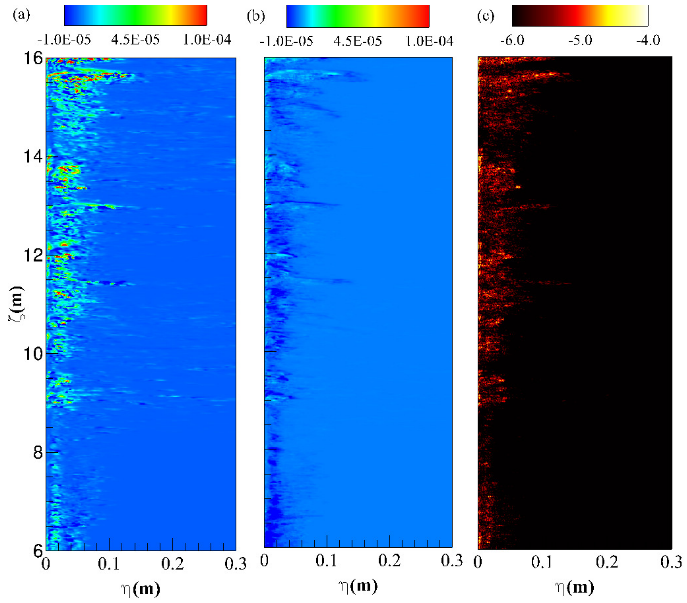

Figure 2.15: Snapshot of rates of (a) turbulent shear production P ($\mathrm{m}^2/\mathrm{s}^3$), (b) buoyancy production B ($\mathrm{m}^2/\mathrm{s}^3$) and (c) viscous dissipation ε (expressed in log scale) for $\theta = 10°$ and $L = 20$ m. The slope-normal distance is enlarged by approximately 10 times relative to the slope-parallel scale in order to show the structure inside the boundary layer.

difference in the relative magnitude of turbulent production (compared with other terms in the energy budget) is observed. For the shallower slopes, turbulent shear production is an order of magnitude greater than buoyancy production, whereas for a vertical ice face the shear production is similar to the buoyancy production. The relative contributions of turbulent fluxes in the production of turbulent kinetic energy K are plotted in figure 2.16b, where the time and area averaged K, dissipation, shear and buoyancy production are denoted by, $\langle K\rangle, \langle\varepsilon\rangle, \langle P\rangle$ and $\langle B\rangle$ respectively, and are calculated as:

$$\langle K\rangle = \frac{1}{2\tau A}\int_A\int_\tau \overline{u_i'u_i'}\,dt\,dA, \tag{2.52}$$

$$\langle P\rangle = -\frac{1}{\tau A}\int_A\int_\tau \overline{u_i'u_j'}\frac{\partial U_i}{\partial x_j}\,dt\,dA, \tag{2.53}$$

$$\langle \varepsilon\rangle = \frac{1}{\tau A}\int_A\int_\tau \nu\overline{\frac{\partial u_i'}{\partial x_j}\frac{\partial u_i'}{\partial x_j}}\,dt\,dA \tag{2.54}$$

and

$$\langle B\rangle = \frac{1}{\tau A}\int_A\int_\tau g(-\overline{\rho' u_\zeta'}\sin\theta + \overline{\rho' u_\eta'}\cos\theta)\,dt\,dA. \tag{2.55}$$

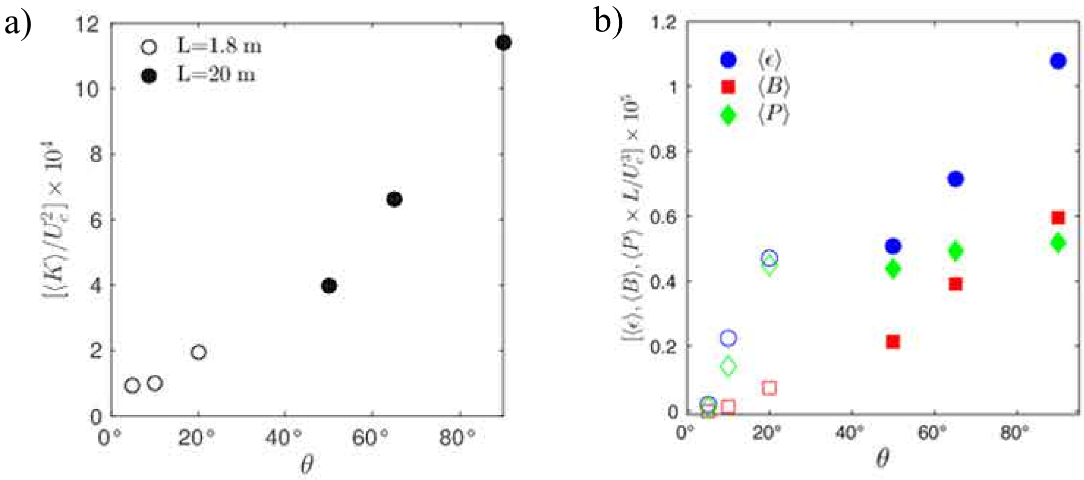

Figure 2.16: Normalised time and area averaged turbulent statistics as function slope angle; (a) turbulent kinetic energy $\langle K\rangle$ is normalised by characteristic velocity scale $U_c \sim (g\beta\Delta SL)^{1/2}$, (b) turbulent dissipation $\langle\varepsilon\rangle$, buoyancy production $\langle B\rangle$, and turbulent shear production $\langle P\rangle$, for 1.8 m domain (filled symbols) and for 20 m domain (open symbols) normalised using the respective domain length L and velocity scale U_c.

The averaging time window is $\tau \sim 10\tau_b$ and A is the area (in the ζ and η plane) containing the boundary layer in the upper-half of the domain length, where the boundary layer is fully turbulent. For steep slopes (figure 2.16a) K is large and the value of $\langle B\rangle$ is comparable or slightly larger than that of $\langle P\rangle$. For small slopes ($\theta \leq 20°$) $\langle P\rangle$ dominates over $\langle B\rangle$.

The production of turbulence, either by velocity shear or buoyancy, is significantly influenced by density stratification and gravity at both limits of ice face inclination. When the slope is steep ($\theta \geq 80°$), turbulent buoyancy flux (predominantly produced in the plume) is less impacted by the weak vertical (stable) buoyancy gradient produced by the solutal boundary layer. In contrast, the buoyancy production for small angles is reduced significantly by two mechanisms. First there is a large reduction in the buoyancy force in the up-slope direction ($g\sin\theta$), which produces the slope-parallel components of $\langle B\rangle$. In addition the development of stable stratification under the sloping ice face causes the turbulent advection in the wall-normal direction to decrease, resulting in smaller buoyancy production. For small slopes the mean shear is large enough to produce turbulence despite the density stratification (while convection is inhibited) and, as a result, the turbulent shear production becomes the dominant mechanism for maintaining turbulence in the inner boundary layer.

2.5 Discussion and Conclusions

This Chapter presents the first DNS of ice dissolution due to convection under a sloping ice face. We have simulated fully turbulent flow at geophysically relevant slopes ($\theta \leq 40°$) at temperature and salinities relevant to Antarctic conditions. The typical Grashof number based on the vertical height of the ice-seawater interface is of the order of $Gr^{\perp} \sim 10^{17} - 10^{19}$, for heights in the range 200 - 800 meters. Although this range is not achievable using DNS with present computational capacity, we have chosen large Grashof numbers ($Gr^{\perp} \sim 10^{10} - 10^{14}$), which are well above the critical $Gr_c^{\perp} \sim 10^9$ for the transition to turbulent convection on a vertical heated wall. The solutions confirm that these conditions ensure a steady but turbulent mean flow. The boundary layer flow changes significantly with the slope. For steep angles a narrow upslope flow of relatively fresh buoyant water develops close to the wall. For small slope angles ($\theta < 20°$), the buoyant up-slope flow is relatively weak due to the reduction of buoyancy force in the along-slope direction. However, the solutions at large Grashof numbers again show a turbulent flow.

Boundary layer properties and ablation rates are dependent on whether the boundary layer is laminar or turbulent. Both the thermal and solutal boundary layer thicknesses increase with decreasing slope angles, resulting in the reduction of heat and salt transport to the interface and consequent reduction of the ablation rate. In the laminar case the ablation rate decreases with along-slope distance as $\zeta^{-1/4}$, consistent with theoretical scaling. In contrast the turbulent cases have ablation rates that are nearly uniform along the slope, as previously found for vertical ice faces [Kerr and McConnochie, 2015; Gayen et al., 2016]. We hypothesize that for domain lengths larger than those achieved in the present DNS, and having a Grashof number greater than the critical value, dissolution rate will be given by the asymptotic dynamics of turbulent boundary layer flow, and the present results can be extrapolated to geophysical scales following the scaling presented here. In that case, for a purely convective boundary layer, the ablation of ice faces into the ocean will follow $V \simeq (\sin\theta)^{2/3}$. This leads to a simple modification of the previously derived dependence of melt rate on the driving temperature difference [Kerr and McConnochie, 2015; Gayen et al., 2016], now taking account of the interface slope as:

$$V \simeq 8.98 \times (\Delta T_L)^{4/3}(\sin\theta)^{2/3} \quad \mathrm{m/yr}. \tag{2.56}$$

An alternative scaling reported by Magorrian and Wells [2016] is based on a buoyant plume model and gives a greater sensitivity of melt rates on θ for small slopes ($V \sim (\sin\theta)^{3/2}$) and an inverse dependence on slope angle ($V \sim 1/\sin\theta$) for near-vertical interfaces. Those trends are not reflected in the present DNS results. The discrepancy may result from a different regime of the convective boundary layer. The model of Jenkins [1991] and Magorrian and Wells [2016] assumes a regime in which the thickness of the laminar sub-layer near the ice face is controlled primarily by shear instability [Grossmann and Lohse, 2000; Wells and Worster, 2008] rather than convective instability as found here. The transition to this shear-dominated regime at steep slopes for saline convection was predicted to occur at $Gr \sim 10^{20}$, which occurs for vertical ice heights of hundreds of metres. At these high Gr, stronger turbulent eddies increase buoyancy spills from the inner to the outer layer. The local buoyancy anomaly at the inner layer decreases and shear dominates the flow. The inner layer thickness decreases with the flow speed and the local Reynolds number asymptotically reaches a constant value (Wells & Worster 2008). The present study uses heights/domain lengths where the boundary layer on near-vertical interfaces remains controlled by turbulent convection. Hence it remains to be demonstrated whether the transition can occur. Further discussion of transition between these two regimes can be found in McConnochie and Kerr [2017].

The turbulent kinetic energy budget shows the presence of statistically steady turbulence in the simulated flow fields for slope angles as small as, $\theta = 5°$. For near vertical slopes ($\theta > 80°$) contributions to turbulent kinetic energy from shear production and buoyancy flux are comparable, with a slightly greater contribution from the buoyancy flux. For small slopes the production of turbulent kinetic energy by buoyancy fluxes is significantly smaller than the turbulent shear production. This potentially implies that the shear associated with large scale ambient geostrophic currents and barotropic tides in the ocean is more likely to contribute to the turbulent transport at the ice face and enhance the melt rate for small slopes.

The present study has focused on the effect of ice face slope on melting that is driven by natural convection. The natural convection on its own can be viewed as a base, or reference, case given that natural convection will always be present irrespective of the magnitude and influence of shear associated with ambient geostrophic currents, internal waves or sub-glacial discharge plumes. The next step will be to include ambient stratification [McConnochie and Kerr, 2016b], subglacial discharge of freshwater [McConnochie and Kerr, 2017a] and ambient shear.

Chapter 3

Effects of ambient current on the melting of the ice shelves

Direct numerical simulations are used to examine the ice-ocean boundary layer and the meltrate in the presence of natural convection and ambient current. A suite of numerical experiments is carried out with imposed far-field horizontal current speeds in the range $U_b = 0 - 2$ ms^{-1}, at ambient (uniform) temperatures in the range $T_b = -1$°C - 2°C, and a weak ambient density stratification (buoyancy frequency, $N = 5 \times 10^{-3}$ s^{-1}). At small current speed ($U_b = 0 - 0.7$ ms^{-1}), the simulations give a meltrate that is insensitive to the ambient current and is well predicted by the convective scaling for melting in a turbulent convective boundary layer [Gayen et al., 2016; Mondal et al., 2019]. For stronger currents the meltrate becomes linearly dependent on U_b and is better represented by the scaling for melting in a shear-driven turbulent boundary layer. A convective boundary layer is always present next to the ice wall and interacts with the mean shear and turbulence is added by the ambient current. At large current speed $U_b \geq 0.07$ ms^{-1}, the resultant mean shear leads to the formation of vortex rolls that are eventually stretched by the resultant mean flow in the mean flow direction. The stretching of turbulence vortex leads to an increased buoyant plume velocities and thinning of the boundary layers. The thinner boundary layers further enhance the diffusive fluxesand result in increased meltrates. The transition from convection-driven melting to shear-driven melting occurs when the local Froude number, surpluses the local Grashof number, based on the salinity boundary layer thickness.

3.1 Introduction

Stability of the Antarctic ice-shelves plays a crucial role in global climate [Paolo et al., 2015] and depends on the processes that govern mass balance including ice-transport from the glacier, snowfall and ablation at the surface, calving of the ice-front and basal melting by oceanic processes. Over recent decades Antarctic ice-shelves are experiencing rapid mass-loss [Picard et al., 2012; Paolo et al., 2016] predominantly caused by the ocean driven melting [Rignot et al., 2013]. Meltrate around the Antarctic basins can go up to 100 m yr^{-1} during the summer season [Paolo et al., 2016]. Fresh melt water flux from the ice shelves, is contributing to the global sea level rise [Rignot et al., 2013] as well as affecting the thermohaline circulation that controls the global heat budget.

Melting is controlled by the turbulent transport of heat and salt at the ice-ocean boundary. Dynamics of this complex process and its functional relationship with the surrounding environment are not well understood. Direct observations within the turbulent boundary adjacent to the ice-ocean interface are difficult and rare. Ocean modelling is an additional tool to understand these phenomena and to estimate the meltrate [Carroll et al., 2016; Schodlok et al., 2016; Sciascia et al., 2013a; DeConto and Pollard, 2016]. As these models often operate to capture large scale ($> O(100m)$) processes reliably, they are unable to resolve the smaller scales including the boundary layer, where the major heat and salt transport are determined by molecular and micro-scale turbulent mechanisms. These models have to rely on small scale parameterizations of the sub-grid scale processes, which are also not coupled to the grid resolutions, resulting in significant uncertainties in the model solutions [Gladish et al., 2012].

The formulations of the ice-ocean parameterisations are based on the conservations of heat (Q_w^H) and salt (Q_w^S) flux as follows:

$$\rho_s V L_f = Q_w^H \quad \text{and} \quad \rho_s V S_{int} = Q_w^S, \tag{3.1}$$

where V, L_f, ρ_s, and S_{int} are the meltrate, latent heat of fusion for ice, density of the ice and the interface salinity, respectively. Based on the common parameterization, heat and salt transport are further expressed in terms of the bulk properties [Holland and Jenkins, 1999],

$$Q_w^H = \rho_w c_w u^* \Gamma_T (T - T_{int}) \quad \text{and} \quad Q_w^S = \rho_w u^* \Gamma_S (S - S_{int}). \tag{3.2}$$

Here c_w is the specific heat of water, Γ_T, Γ_S are the turbulent transfer coefficients of heat and salt respectively. The friction velocity u^* is defined in terms of the shear stress at the ice-ocean interface and replaced with $\sqrt{C_d} U_b$ using simple parameterization based on the grid velocity. In this parameterization the boundary layer turbulence is assumed to be driven by shear instability of ambient current or buoyant plume. Here a buoyant plume represents a contribution of natural convection at the ice-ocean interface either due to the melting of the interface or a subglacial discharge of fresh water [Payne et al., 2007; Jenkins, 1991, 2011a, 2016]. There have been attempts to validate the parameterization under near horizontal ice shelves [Jenkins, 2011a] and sea ice [McPhee, 1992; McPhee et al., 1999]. However, recent study shows that turbulence can be driven by convective instability under sloping [Mondal et al., 2019; McConnochie and Kerr, 2018] as well as vertical ice-shelves [Gayen et al., 2016] and suggests different functional relations.

Recently, laboratory experiments have been conducted to study the interaction of a vertical and sloping ice wall with warm salty water and to examine the melt rate. Meltwater plume develops in presence of a homogeneous ambient fluids [Kerr and McConnochie, 2015; McConnochie and Kerr, 2016, 2018], a uniformly stratified [McConnochie and Kerr, 2016b] and two layer stratified ambient fluid [Sciascia et al., 2014; Ezhova et al., 2018]. Plume becomes turbulent when the effective Grashof number of buoyancy driven flow is large enough [Turner, 1979; Mondal et al., 2019]. When turbulence is produced by convection alone from buoyant plume, study suggests that the ablation velocity scales as $V \sim \Delta T_L^{4/3}$, where ΔT_L is the difference between the ambient temperature T_w and the freezing point at ambient salinity T_L [Kerr and McConnochie, 2015]. Three dimensional Direct Numerical Simulations of the dissolution of the ice-shelf in saline water have focussed on natural convection alone, for a vertical [Gayen et al., 2016] and sloping planar ice face [Mondal et al., 2019]. For a range of typical Antarctic water temperatures and salinities, the computed dissolution rates are in excellent agreement with the laboratory experiments [Josberger and Martin, 1981; Kerr and McConnochie, 2015; McConnochie and Kerr, 2018] and predicted a 4/3 power dependence of turbulent ablation rate on the driving temperature difference. The DNS also showed that the ablation rate is independent of height when the boundary layer is turbulent. For a sloping ice face the meltrate shows a strong dependence on the slope angle with $V \sim \sin^{2/3}\theta$ (where θ is the angle of inclination with the horizontal plane) due to the development of stratification within the boundary layer from the meltwater under the ice face [Mondal et al., 2019].

However in the presence of both the ambient shear and natural convection, the nature of the turbulence becomes complex and is still not well understood. In real oceanic scenario around Antarctica, the ice-sheets are inclined, where convective plume coexists with an ambient geostrophic or tidal current that adds shear force as an additional impact. Recent experiments on a drifting iceberg in oceanic ambient with natural convection have shown that the structure of the boundary layer is influenced by the relative strength of the convection and ambient shear [FitzMmaurice et al., 2017]. Based on the relative strength of convection and the ambient shear the boundary layer turbulence can either be convectively driven or shear driven. An analysis of the boundary layer turbulence transport and classification of different flow regimes are necessary to understand the flow dynamics and to accurately estimate the meltrate. Unfortunately, the observational data are not sufficient to establish a functional form of meltrate at Antarctic ambient conditions, even assuming the predetermined transfer coefficients. Hence, we conduct numerical experiments to study the boundary layer dynamics under a sloping ice face, forced by an ambient current and buoyant plume from convection.

3.2 Problem set up

The flow field is solved in a domain of length L, width W and depth D with ice face placed on the left of the domain as shown in figure 3.1. Flow field is given by $\tilde{\mathbf{u}} = [u_\zeta, v, u_\eta]$, where u_ζ, v and u_η are the velocities in the up-slope (ζ), spanwise (y) and wall-normal (η) directions, respectively. Three dimensional Navier Stokes equations are solved under Boussinesq approximation for an incompressible fluid along with the equations for continuity, flux equations for heat and salt as follows:

$$\nabla \cdot \tilde{\mathbf{u}} = 0 \tag{3.3}$$

$$\frac{\partial \tilde{\mathbf{u}}}{\partial t} + (\tilde{\mathbf{u}} \cdot \nabla)\tilde{\mathbf{u}} = -\frac{1}{\rho_0}\nabla p^* + \nu\nabla^2\tilde{\mathbf{u}} + \frac{\rho^*}{\rho_0}\tilde{\mathbf{g}} \tag{3.4}$$

$$\frac{\partial T^*}{\partial t} + \tilde{\mathbf{u}} \cdot \nabla T^* = \kappa_T \nabla^2 T^* \tag{3.5}$$

$$\frac{\partial S^*}{\partial t} + \tilde{\mathbf{u}} \cdot \nabla S^* = \kappa_S \nabla^2 S^*. \tag{3.6}$$

$$\rho^* = \rho_0(\beta S^* - \alpha T^*), \tag{3.7}$$

where α and β are the thermal expansion coefficients and haline contraction coefficents respectively. Here $\tilde{\mathbf{g}}$ is a vector that depends on the inclination of ice face as,

$$\tilde{\mathbf{g}} = \hat{\zeta}\ \ g \sin\theta - \hat{\eta}\ \ g\cos\theta \tag{3.8}$$

The solution is obtained using a mixed spectral/finite difference algorithm [Gayen et al., 2010, 2015]. The wall-normal spatial derivatives are computed with second order finite difference method. The up-slope (ζ) and spanwise (y) directions are considered periodic and derivatives in this direction are treated with a pseudo spectral method. Heat and salt flux at the ice-ocean boundary is obtained by solving the interface flux balance. The ice-ocean boundary layer is assumed to be planar over the area of simulation runs and is fixed at $\eta = 0$. This implies that the entire domain moves towards the ice face as the ice melts. A planar ice face also means that any effects of curvature and related changes in the Gibbs free energy at the interface are ignored while calculating the heat flux. At the ice-ocean interface we solve the conservation equations for thermal and salinity fluxes as discussed in Mondal et al. [2019] and Gayen et al. [2016]. The ice is assumed to have zero salinity. Hence diffusive salt flux within the ice are also ignored in the present study. The specific heat content and temperature gradients within the ice are also ignored. The interface temperature is a linear function of the seawater salinity at the interface, $T_i = a_s S_i$, where the slope of the liquidus is $a_s = 6 \times 10^{-2}$ °C $\mathrm{g}^{-1}\mathrm{kg}$ is a constant [Holland and Jenkins, 1999].

The interface is sloped at $\theta = 10°$ with the horizontal direction. In order to study the contribution of the ambient current to the meltrate, a uniform ambient flow in the spanwise (across slope) direction, which is always orthogonal to the convective flow in the up-slope direction is imposed (figure 3.1). The flow field is initiated with a tan hyperbolic profile with large wall stress. As the velocity boundary layer develops, the

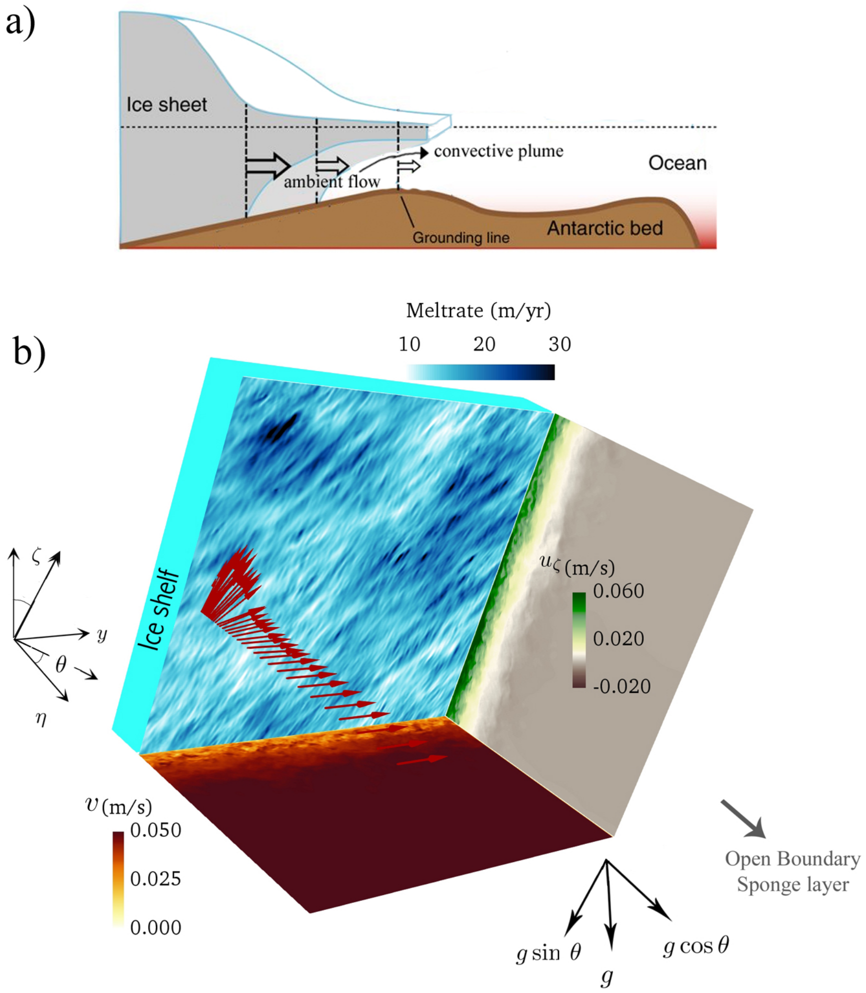
a)
Ice sheet
convective plume
Ocean
ambient flow
Grounding line
Antarctic bed
b)
Meltrate (m/yr)
10
20
30
Ice shelf
u_ζ (m/s)
0.060
0.020
-0.020
ζ
y
θ
η
v (m/s)
0.050
0.025
0.000
Open Boundary
Sponge layer
$g\sin\theta$
g
$g\cos\theta$

Figure 3.1: Simulated flow field with $T_b = 1^\circ$ and $U_b = 0.05$ ms^{-1}. Plume velocity, u_ζ (ms^{-1}) and spanwise velocity v (ms^{-1}) are shown in $\eta - \zeta$ and $\eta - y$ respectively. The spatial variation in meltrate, V (m/yr) is shown over the ice face ($y - \eta$ plane) as viewed through the ice.

Table 3.1: Simulations

U_b (ms^{-1})	T_b (°C)				S_b(g kg^{-1})	N(s^{-1})
	$-1°$	$0°$	$1°$	$2°$		
.00	✓	✓	✓	✓	35	$5{\times}10^{-3}$
0.05	✓	✓	✓	✓	35	$5{\times}10^{-3}$
0.07	✓		✓		35	$5{\times}10^{-3}$
0.10	✓	✓	✓	✓	35	$5{\times}10^{-3}$
0.15	✓		✓		35	$5{\times}10^{-3}$
0.20	✓		✓		35	$5{\times}10^{-3}$

wall stress drops and equilibrates to a quasi-steady value. Over this time-interval the wall-normal profiles of the averaged plume velocity for large ambient velocity forcing (U_bҰ0.15 ms^{-1}) shows prominent log-layer (figure 3.4b). The strength of the ambient current is considered as a primary parameter of the numerical experiment. The simulations are all performed at four different ambient temperatures, $T_b = -1°$C, 0°C, 1°C and 2°C, respectively. The ambient salinity is kept fixed at 35 g kg^{-1} with an ambient stratification, $N = 5 \times 10^{-3}$ s^{-1} which is close to a value observed under the ice-cavities of Antarctica. The simulations are carried out with a fixed Prandtl number, Pr=14 while the Schmidt number is kept at Sc=500 at the domain interior, based on a value of dynamic viscosity, $\nu = 1.8 \times 10^{-6}$ m^{2}s^{-2}, thermal diffusivity, $\kappa_T = 1.285 \times 10^{-7}$ m^2 s^{-1}, salinity diffusivity, $\kappa_S = 7.2 \times 10^{-10}$ m^2 s^{-1} at the boundary and $\kappa_S = 3.6 \times 10^{-9}$ m^2 s^{-1} at the interior. We also fix $g = 10$ m s^{-2}, specific heat $c_w = 4184$ J kg^{-1} K^{-1}, latent heat of fusion $L = 335$ kJ K^{-1}. Various cases are simulated, as listed in table 1.

The domain is 3 m long (ζ), 3.5 m wide (y) and 6 m deep (η) with number of gridpoints 512 and 128 and 512 respectively. Variable grid spacing with a hyperbolic stretching function is used in the wall-normal direction. The smallest grid spacing is kept at $\Delta\eta = 0.0003$ m next the ice-ocean interface, sufficient to resolve the diffusive boundary layer.We compute the friction velocity,

$$u^* = \sqrt{\rho_0 \nu \left(\frac{du_\zeta}{d\eta}\right)^2 + \left(\frac{dv}{d\eta}\right)^2}, \tag{3.9}$$

representing the stress at the ice wall. In wall units (as defined in the caption of figure 3.4) the grid spacings vary from $\Delta\eta^* = 0.5$ for low to moderate shear cases upto $\Delta\eta^* = 1.2$, $\Delta y^* = 30.41$, $\Delta\zeta^* = 23.5$ for high shear cases ($U_b > 0.07$ ms^{-1}). Away from the ice wall an open boundary is considered on the right-hand side of the domain with a sponge layer between $\eta = 2.5 - 3$ m. Detail description of sponge layer implementation is given in Gayen et al. [2016]; Mondal et al. [2019].

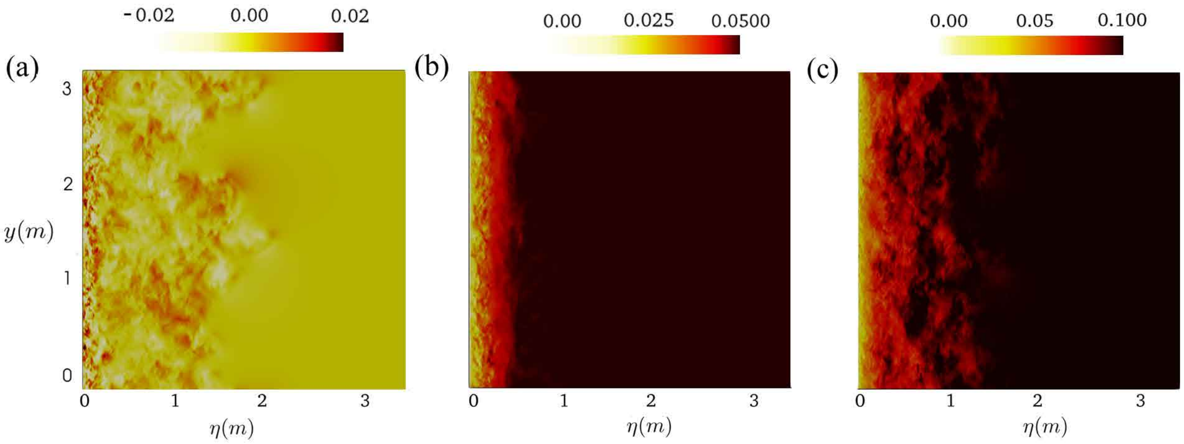

Figure 3.2: Snapshot of the spanwise velocity field, v (ms^{-1}) over $y - \eta$ plane for a) $U_b = 0.0$ ms^{-1} and b) $U_b = 0.05$ ms^{-1} and c) $U_b = 0.1$ ms^{-1}. Data taken for $T_b = -1°\mathrm{C}$.

3.3 Results

For no ambient current the boundary layer under a sloping ice face is formed by a buoyant plume produced from fresh meltwater [Mondal et al., 2019]. In presence of both the convection and an ambient current, the boundary layer flow becomes more complex. The snapshots of the flow field for spanwise velocity, up-slope velocity and meltrate patterns on the ice faces are shown in figure 3.1. Melting of the ice face drives a fresher, more buoyant convective plume that becomes turbulent as shown by the up-slope velocity field in $\zeta - \eta$ plane. As this convective flow moves upslope it entrains surrounding saltier and warmer fluid and a prominent plume forms. The ambient flow in the spanwise direction and the associated boundary layer is shown in $y - \eta$ plane. Thus flow next to the ice wall is produced by two orthogonal flows (convective plume and ambient current) as indicated by the arrowheads.

A comparison of the spanwise velocity field for different ambient forcings is shown in figure 3.2. The surface contour plot of the spanwise velocity field shows that the turbulent fluctuations are produced by natural convection at the sloping ice face (figure 3.2a). In presence of the ambient current, the random fluctuations disappear and a distinct wall boundary layer develops. For a fixed ambient current the width of the boundary layer remains constant over a quasi-steady state and the diffusive fluxes become constant. As the ambient current increases the boundary layer becomes more turbulent and spreads in the wall-normal direction (figure 3.2b and 3.2c respectively).

The plume structures are better understood in figure 3.3. Figure 3.3a represents the boundary layer plume for a purely convective flow. On the other hand, figure 3.3b and 3.3c represents a moderately forced ($U_b = 0.05$ ms^{-1}) and a strongly forced ($U_b = 0.1$ ms^{-1}) boundary layers, respectively. For figure 3.3a and 3.3b, the plume structures are quite similar with a slightly higher plume velocity for the later. Com-

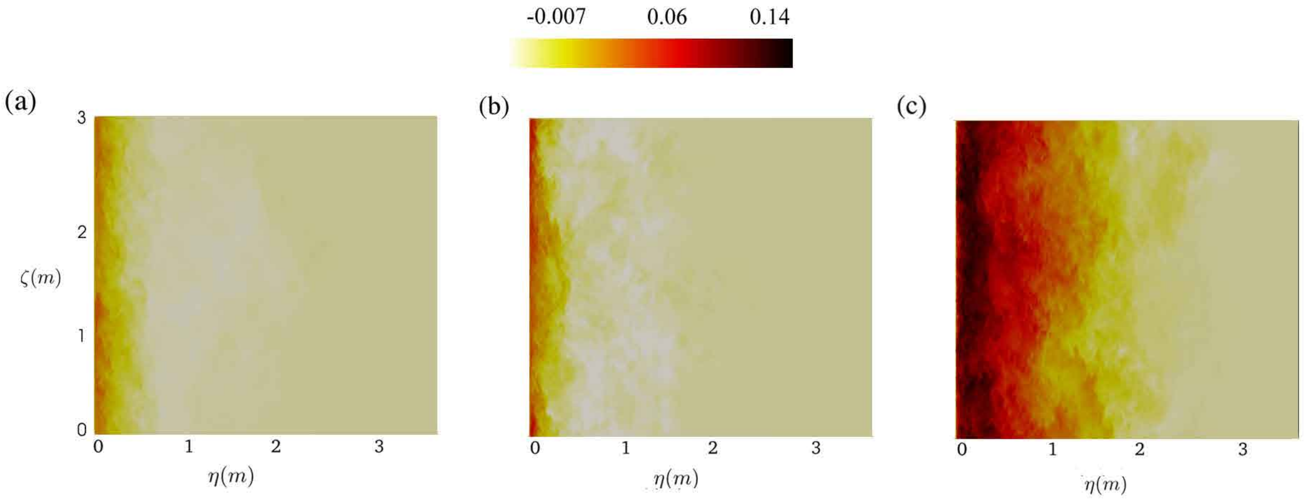

Figure 3.3: Snapshots of up-slope velocity, u_ζ (ms^{-1}) in $\zeta - y$ plane for a) $U_b = 0$ ms^{-1} (purely convective flow), b) $U_b = 0.05$ ms^{-1} and c) $U_b = 0.1$ ms^{-1} respectively. Ambient conditions similar to figure 3.2.

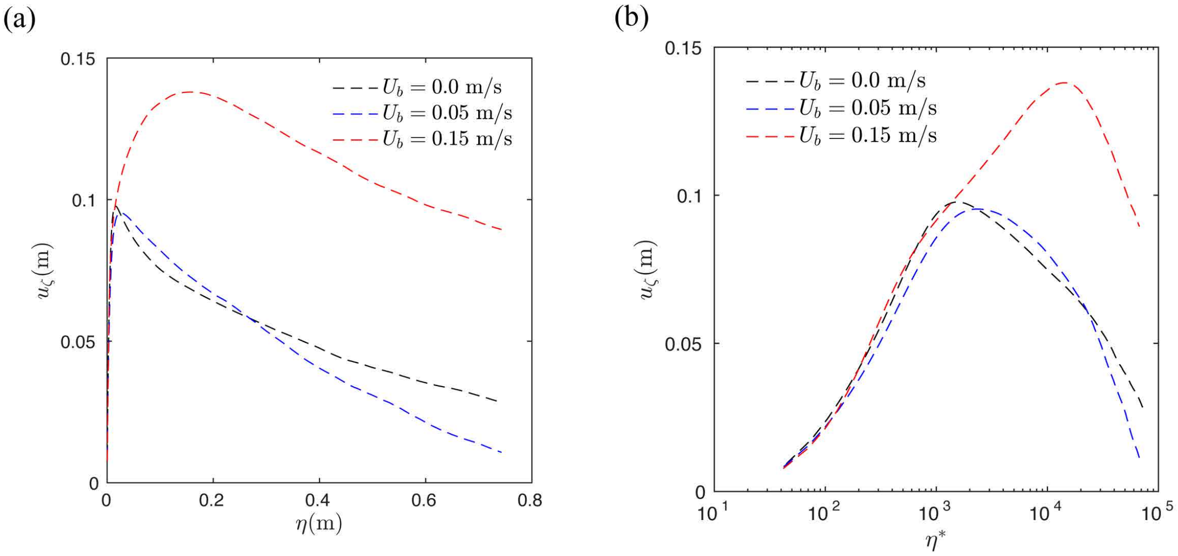

Figure 3.4: a) wall-normal profile of the u_ζ for different ambient currents as a function of wall normal distance. b) same plots over a friction coordinate, $\eta^+ = \eta * u^*/\nu$. Where u_τ is the friction velocity at the wall given by $u^* = \sqrt{\tau/\rho}$, $\tau = du_\zeta/d\eta$.

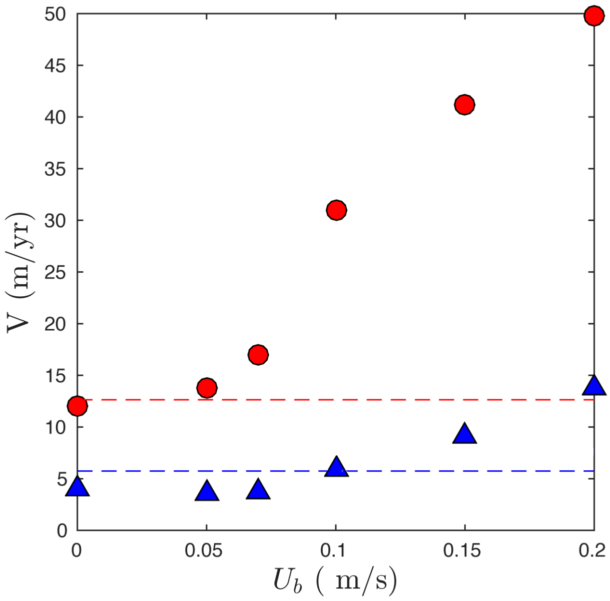

Figure 3.5: Meltrate V (μms^{-1}) as a function of ambient flow, U_b (ms^{-1}) for a slope angle, $\theta = 10°$ and two different background temperatures, $T_b = -1°$C (blue dot) and $T_b = 1°$C (red dot) respectively. $U_b = 0$ ms^{-1} corresponds to a purely convective flow field. The red and blue dashed line represents the theoretical estimation of the meltrate based on the convective scaling [Mondal et al., 2019].

pared to them, figure 3.3c is noticeably different. The average boundary layer width increases from 0.5 m for $U_b = 0.05$ ms^{-1} to upto 1.8 m for $U_b = 0.1$ ms^{-1} and the corresponding plume velocities are $U_\zeta = 0.08$ ms^{-1} and 0.15 ms^{-1}, respectively at the same time instant of $T = 1.42$ hr.

Details of the plume structure is investigated from the average profiles of the plume velocities in the wall-normal direction for different ambient currents (figure 3.4a). Black, blue and red striped lines represent the plume velocity for purely convective ($U_b = 0$ ms^{-1}), weakly forced ($U_b = 0.5$ ms^{-1}) and strongly forced ($U_b = 0.15$ ms^{-1}) boundary layers respectively. Similar to figure 3.3, the profiles for $U_b = 0$ ms^{-1} and $U_b = 0.05$ ms^{-1} look similar with similar maximum plume velocity ($u_\zeta \simeq 0.1$ ms^{-1}) but slightly wider plume width for the later. With higher forcing ($U_b = 0.15$ ms^{-1}), the plume profile is different and the plume is much wider. In figure 3.4b the plume velocities are plotted in the frictional co-ordinate with wall-normal axis in the logarithmic scale. The region right next to the wall is diffusion dominated and is characterised by the exponential part of the profile in the logarithmic scale. Right next to this layer, a logarithmic layer is formed for $U_b = 0.15$ ms^{-1}, as shown by the linear part of the profile in logarithmic scale. This is the typical characteristic of a shear driven boundary layer.

In figure 3.5, the averaged meltrate is plotted as a function of the ambient current strength. These meltrates are estimated at the mid-deph of the periodic up-slope

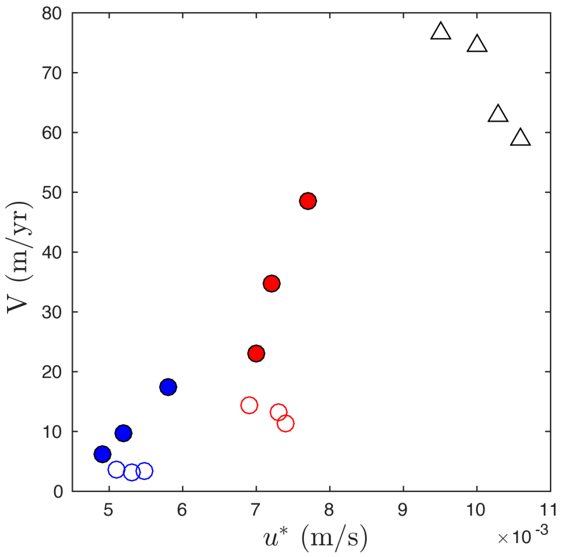

Figure 3.6: Meltrate V (μ ms^{-1}) as a function of friction velocity, u^* (ms^{-1}) with $T_b = -1$°C and 1°C respectively for a slope angle $\theta = 10°$. Blue and red filled circles (at respective T_b as in figure 3.5) correspond to simulated meltrates where boundary layer is shear driven ($U_b >> 0.07$ ms^{-1}) , while the open symbols represents when the flow convectively driven. Black triangles are the simulated meltrate for a convective only case, with $T_b = 2.3$°C, over a range of slope angle, $\theta = 50° - 90°$, where data are taken from Mondal et al. [2019].

direction from the diffusive fluxes based on equation (4.6) and (2.13) at the ice wall by spatially averaging in the span-wise direction and temporally averaging for at least 100 times of the buoyancy time period. The averaging is done over the temporal window when the stress at the ice wall is at quasi-steady state, represented in the temporal profile of the friction velocity, u^* (not shown in here). Red dots and blue triangles represents the estimated meltrate for ambient temperatre, $T_b = 1°$ C and $-1°$ C, respectively. For a given U_b, larger T_b drives more heat and salt transfer across the interface, resulting in higher overall meltrate. The dashed line on the plot represents theoretically estimated values of the meltrate when the boundary layer is purely convective [Mondal et al., 2019], represented by

$$V = 8.98 \times (\Delta T)^{4/3} \sin^{2/3}\theta \text{ ms}^{-1}. \tag{3.10}$$

The estimated meltrates for $U_b = 0$ ms^{-1} for the two respective ambient temperatures over the present re-entrant domain show slightly lower values compared to the meltrate at same T_b from a fixed domain (represented by the dotted line on figure 3.5). This could be an artifact of the periodic domain where the over-freshening of the inner layer by the re-entrant, freshwater laden plume acts to lower the scalar gradiant at the ice wall that results in a low diffusive heat and salt flux.

Over the lower velocity range ($U_b \leq 0.07$ ms^{-1}) meltrates are found to be less

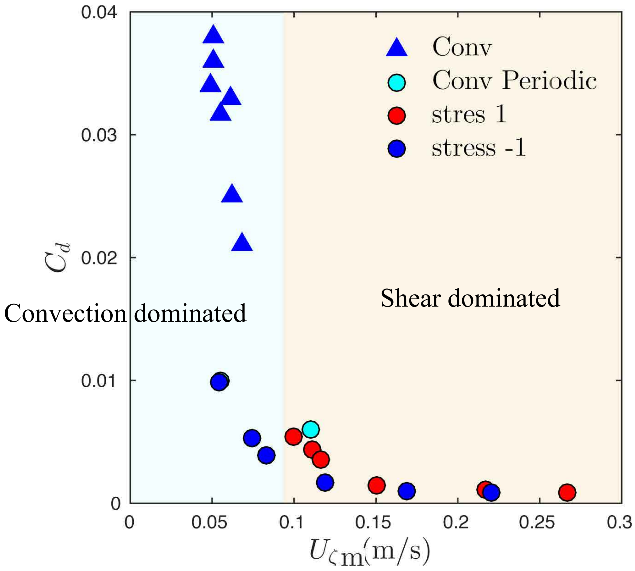

Figure 3.7: Estimated drag coefficient, C_d based on the DNS data as a function of the mean velocity at the far field $U_{\zeta m} = \sqrt{U_b^2 + U_\zeta^2}$. Blue triangle represents C_d for the convective plume over a closed domain with varying slope angles, cyan circle represents the same for a periodic domain, blue and red circles represent C_d for a boundary layer forced by an ambient flow orthogonal to the convection direction for ambient temperature $T_b = -1°$ C and $1°$ C respectively. Convection dominated region and shear dominated region are represented by the green and orange shadow respectively.

sensitive to U_b with magnitudes similar to a purely convective boundary layer. With increasing forcing a change in flow regime is observed and the meltrate starts to increase linearly with increasing U_b. For higher T_b this transition occurs at a lower U_b value. Figure 3.5 clearly indicates two different regime of meltrate. In higher velocity regime the estimated meltrates are well co-related with the ambient current speed. However the correlation breaks down in the lower velocity range where they are more likely to follow the convective scaling law (equation 3.10).

In figure 3.6, the estimated meltrates are plotted as a function of u^*, for $T_b = -1°$C (blue dots) and $1°$C (red dots) respectively. When the ambient flow is well above $U_b \geq 0.07$ ms^{-1}, the meltrates are well correlated with u^* for both the T_b values. On the contrary, when the ambient flow is weaker, the meltrates are no longer correlated to the u^*, as represented by the hollow circles in figure 3.6. The hollow black triangles in figure 3.6 represents the meltrate for a convective flow field at $T_b = 2.3°$C on a fixed domain where the slope angles are varied. These meltrates are also uncorrelated and independent to u^*.

Based on the numerical results we also calculate the drag coefficient $C_d \sim u^{*2}/U_{\zeta m}^2$ where $u^* = \sqrt{\tau/\rho}$ is the friction velocity, τ being the stress at the wall and $U_{\zeta m}$ is the resultant velocity next to the ice-wall based on maximum plume velocity, U_ζ and

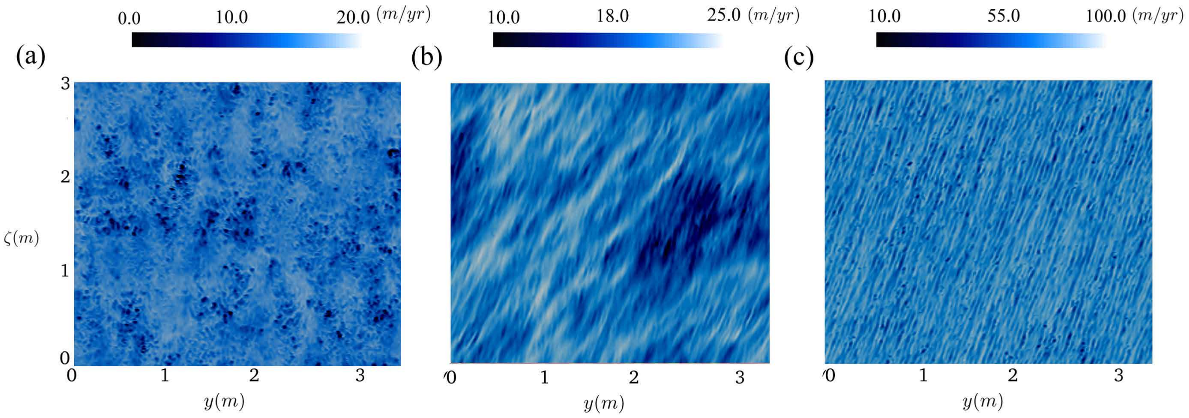

Figure 3.8: Instantaneous snapshot of meltrate (ms^{-1}) at $T_b = -1°$ C, estimated from the thermal flux at the ice interface ($\zeta - y$ plane) for a) $U_b = 0$ ms^{-1} (purely convective flow), b) $U_b = 0.05$ ms^{-1} and c) $U_b = 0.15$ ms^{-1} respectively.

ambient current U_b as $U_{\zeta m} = \sqrt{U_b^2 + U_\zeta^2}$, as used in the ocean models for different flow scenario. In figure 3.7, C_d is plotted as a function of the mean velocity, $U_{\zeta m}$. The meltrates over a periodic domain with a fixed slope angle $\theta = 10°$ (circles) show a trend consistent with the meltrate distribution in figure 3.5. At higher mean flow ($U_{\zeta m}$) the boundary layer is shear driven and C_d is assuming a constant valus of 0.001. With lower ambient current the mean flow at the background decreases and the flow is becoming convection dominated. In such cases C_d is no longer a constant rather increasing with decreasing $U_{\zeta m}$. A recent paper by Based on a recent numerical study by Ezhova et al. [2018] at a subglacial discharge plume over a vertical ice-face also reported a range C_d much larger than the canonical value 0.001. The blue triangles in figure 3.7 represents estimated C_d over a fixed domain where the slope of the ice-interface is varied. Local stratification from the meltwater increase the stress at the ice wall by suppressing the velocity boundary layer in the wall normal direction as a result the effective u^* increases. At the same time stratification under the slope causes the meltrate to decrease [Mondal et al., 2019]; to compensate C_d increases upto 0.04. Unfortunately in the large-scale models a constant C_d value is used, mostly suited for a shear driven regime. Over lower ambient current and for a convective boundary layer these models mostly under-predict the meltrate with a lower C_d value.

The spatial distribution of meltrate at the ice-interface reflects the non-linear nature of the turbulence under different flow conditions. Figure 3.8a represents the surface contour of the meltrate for a purely convective flow-field ($U_b = 0$ ms^{-1}). The meltrate is evenly distributed over the ice-interface and no distinct pattern can be found. In presence of an ambient current, consecutive high and low melt regions emerges at the ice face. These streak-like structures, are closely aligned with the di-

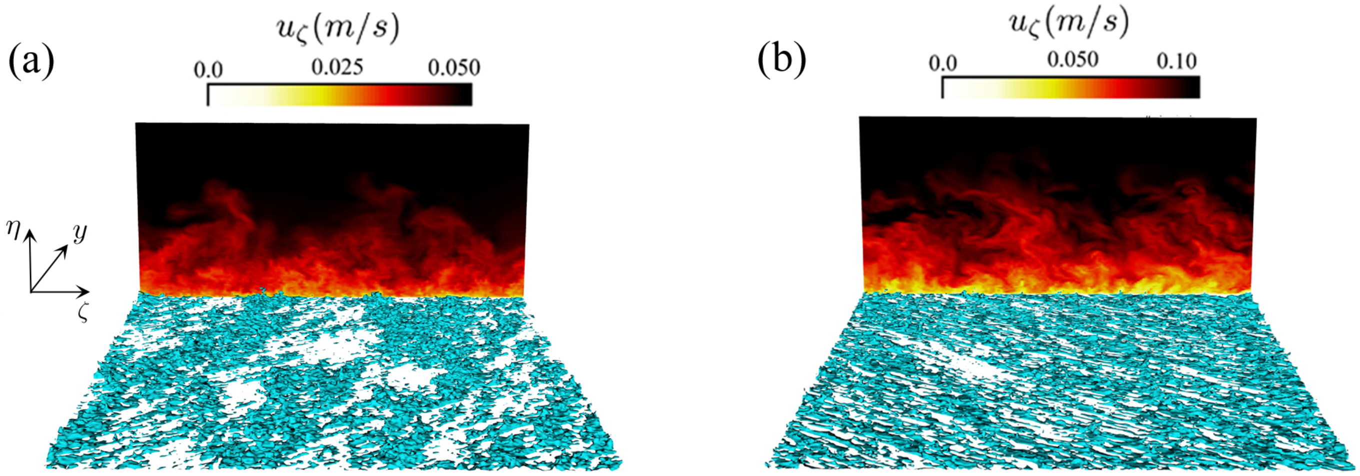

Figure 3.9: Plots of the iso-surfaces of spanwise vorticity (ω_y), along with the spanwise velocity (v ms^{-1}) in the ζ direction for a) $U_b = 0.05$ ms^{-1} and b) $U_b = 0.1$ ms^{-1}.

rection of the mean shear and are caused by the resultant flow at the boundary. For a moderately forced boundary layer (ambient current $U_b = 0.05$ ms^{-1}) the patterns are wider and sparsely placed (figure 3.8b). At large forcing with $U_b = 0.1$ ms^{-1}, these streaks like pattern become thinner, distinct and highly dense as shown in figure 3.8c. The meltrate in atleast 4 times higher and the streaks are more aligned to the vertical direction in presence of a stronger plume velocity.

The turbulence vortex structure at the boundary layer helps to better understand the meltrate pattern and boundary layer flow. In figure 3.9, we examine the iso-surface of vorticity in the spanwise direction. The $\eta - \zeta$ plane represents the instantaneous snap-shot of the spanwise velocity, in the direction of U_b, while the $y - \zeta$ plane represents a plane parallel to the ice-face at the vicinity of the ice-wall. Figure 3.9a and 3.9b represents the vortex structures for weakly shear driven ($U_b = 0.05$ ms^{-1}), and fully shear-driven ($U_b = 0.15$ ms^{-1}) boundary layer respectively, along with the spanwise velocity field. When the ambient current is weak, the vortex structure is less prominent. With stronger spanwise flow relatively smaller scale appears and the vortex tubes are elongated and stretched in the resultant flow direction via vortex stretching mechanism [Kundu and Cohen, 1990]. As a result finer vortex structures appear on the ice-face compared to $U_B = 0.05$ m s^{-1}.

This mechanism is explained further using schematic figure 3.10 and following equation.

$$\frac{d\omega_y}{dt} = U_{\zeta m}\frac{\partial \omega_y}{\partial \zeta m} \tag{3.11}$$

Here ω_y is the vorticity in the spanwise direction a $U_{\zeta m}$ is the resultant of the ambient and plume velocity in the mean flow direction ζm over the ice face(as defined in

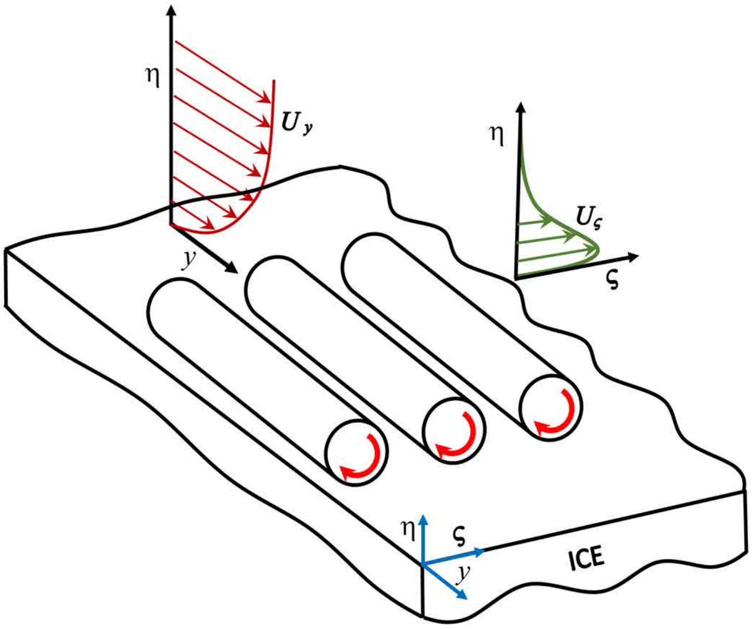

Figure 3.10: Schematic of the vortex stretching mechanism in the flow direction as a result of the interacting convective and shear boundary layer.

the caption of figure 3.7). Stress at the ice wall creates vortex rolls that are stretched and elongated by the mean flow. As these vortex tubes are streched in the mean flow direction the vortex tubes become thinner. By the conservation of angular momentum the eddy turnover rate also increases. Faster eddy transport enhances the turbulent fluxes at the ice-interface as shown in the diagram 3.10. As a result thinner and stronger stripes of high and low meltrate band appear. The increase in vorticity in the spanwise direction ($\omega_s = u_s/\delta$) implies either a decrease in the thickness of the boundary layer (δ) and/or an increase in the plume velocity (u_s). Both these effects can increase the overall heat flux and hence the meltrate.

Figure 3.11 shows the snapshot of the turbulent kinetic energy (*tke*) with increasing strength of the ambient current. Figure 3.11a represents the *tke* field for a purely convective flow. With stronger U_b *tke* increases at the boundary layer (figure 3.11 b, c). For all three cases a *tke* hotspot is observed right next to the ice wall. The wall-normal profile of the spanwise and up-slope averaged *tke* for the respective ambient currents is shown in the bottom panel of figure 3.11(d, e, f). For $U_b = 0$ (figure 3.11d) *tke* peaks close to the ice-interface, where convective flow creates high shear at the wall. The shear sharply drops to half of its value within $\eta = 0.02$ m. Over the rest of the plume almost an uniform *tke* prevails and gradually drops to zero at the edge of the plume. With a low ambient forcing ($U_b = 0.05$ ms^{-1}, figure 3.11e) the*tke* increases and spreads in the wall-normal direction upto $\eta = 0.8$ m. In contrast to this, for $U_b = 0.1$ ms^{-1} the profile is strikingly different. The average *tke* is almost 4 times higher and has a value 3×10^{-4} m^{2}s^{-2} next to the ice-interface, that drops to 10^{-4} m^{2}s^{-2} within $\eta = 0.03$ m. Over this shear driven boundary layer the energetic turbulent eddies transport heat and salt at the ice-ocean boundary and drive a strong convective plume where, *tke* is produced due to high shear at the wall by the combined effects of ambient flow and the convective plume.

The wall-normal profile of different component of the *tke* budget for a purely convective ($U_b = 0$ ms^{-1}) and shear dominated ($U_b = 0.1$ ms^{-1}) boundary layer are shown in figure 3.12. Figure 3.12a shows that for the purely convective boundary layer with $\theta = 10°$, the turbulence is still shear driven. Closer to the wall there is a significant contribution of the buoyancy towards the net turbulent production. Little away from the wall the buoyancy production becomes negative. In contrast, for a highly sheared turbulent boundary layer there is a negligible contribution of the buoyancy production towards the net turbulent production.

3.4 Discussion and Scaling analysis

The buoyant melt water forms a momentum boundary layer adjacent to the ice wall. The ambient flow in the spanwise direction creates a shear layer that encompasses the entire convective layer. Very close to the ice-interface, diffusive sublayers (viscous, solutal and thermal) are formed. Properties of the sublayer control the salt and heat flux at the interface. To understand the boundary layer dynamics, we investigate into the velocity and salinity profiles from the ice wall by revisiting the momentum

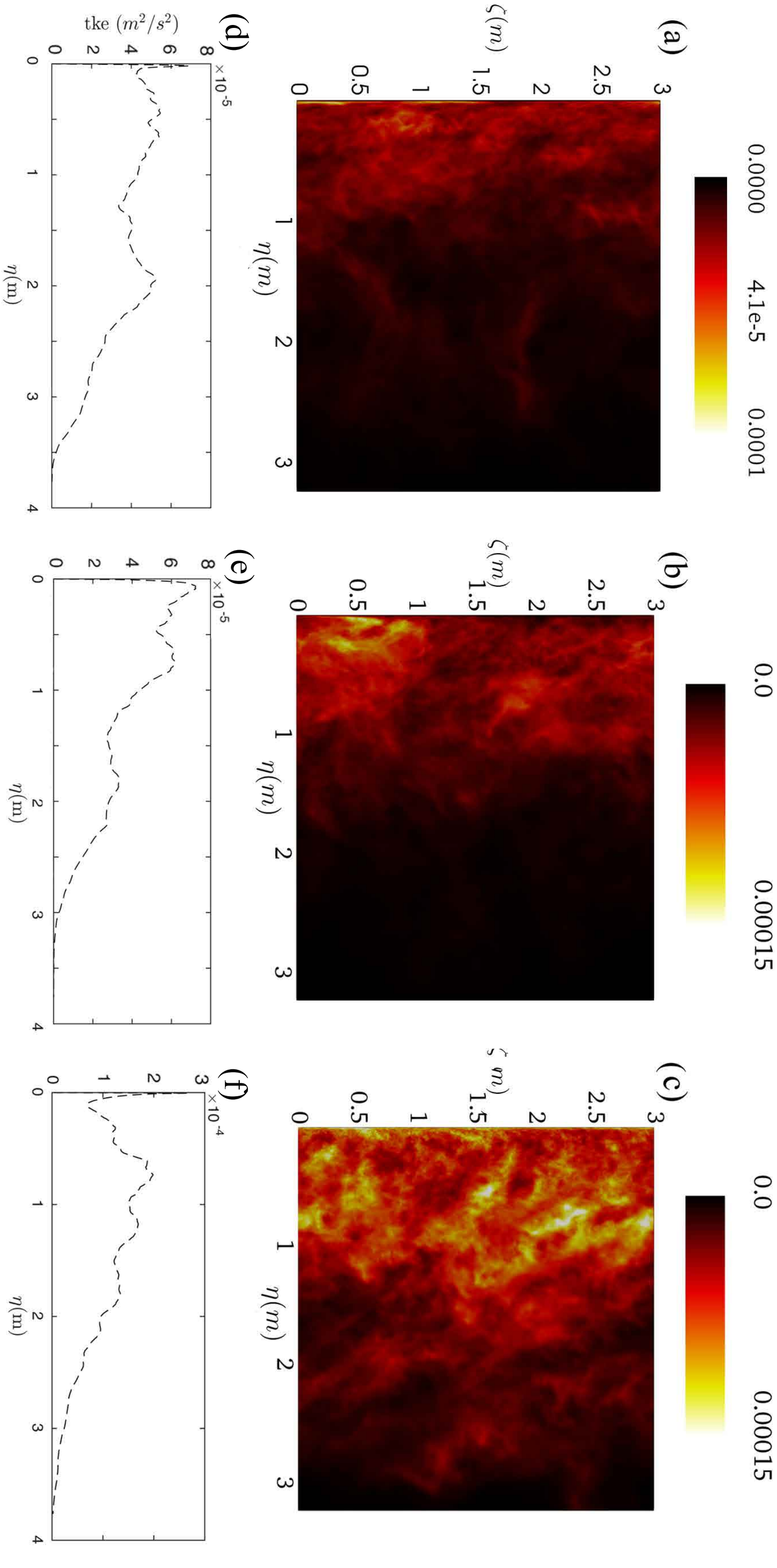

Figure 3.11: Instantaneous snapshot of the tke in the $\zeta - \eta$ plane for a) $U_b = 0$ ms^{-1}, b) $U_b = 0.05$ ms^{-1}, c) $U_b = 0.1$ ms^{-1} (top panel). Time and domain averaged *tke* as a function of the wall-normal distance (η) is shown in d), e) and f).

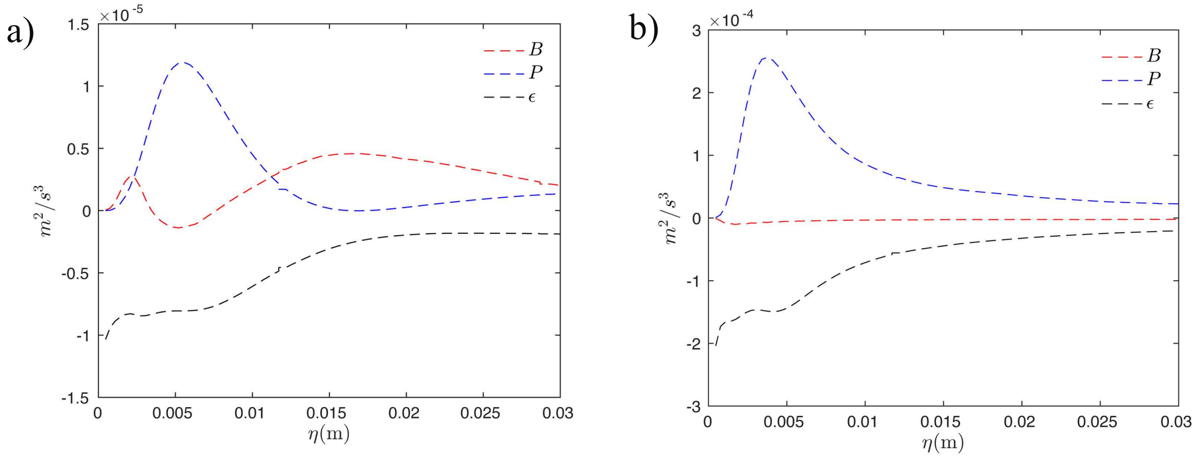

Figure 3.12: Time and spatial averaged buoyancy production (B), turbulent shear production (P) and dissipation (ϵ) as a function of the wall-normal distance (η), for a) purely convective flow field ($U_b = 0$ ms^{-1}) and b) forced flow field ($U_b = 0.1$ ms^{-1}).

balance. Wall-normal profiles of salinity anomaly and the mean velocity for a purely convective ($U_b = 0$ ms^{-1}) and shear driven ($U_b = 0.10$ ms^{-1}) boundary layers are shown in figure 3.13a and 3.13b, respectively. For convective boundary layer, the viscous sublayer is O(0.001)m thick, which is almost twice as wide compared to the shear driven boundary layer. Beyond this layer there is a significant residual salinity anomaly spanning upto $\eta = 0.1$ m and the plume mean velocity peaks at the outer edge of this region. In contrast, for the shear driven boundary layer (figure 3.13b) the salinity anomaly becomes negligible beyond $\eta = 0.005$ m while the velocity peak occurs at $\eta = 0.02$ m. Within the region $\eta = 0.005 - 0.1$ m, a prominent velocity log-layer exists. We define the inner layer as the region over which salinity anomaly is non-zero and that encompasses the logarithmic layer. We conclude that buoyancy plays no role in this region. Beyond this logarithmic region the salinity anomaly is absent and buoyancy again has no contribution to the flow.

The momentum equation within the inner layer can be written as

$$\frac{\partial U_i}{\partial t} + U_j \frac{\partial U_i}{\partial x_j} + \simeq -\frac{\partial P}{\partial x_i} + g(\beta S^* - \alpha T^*)\delta_{i3} + \nu \nabla^2 U_i - \frac{\partial (u_i u_j)}{\partial x_i}. \tag{3.12}$$

Here, U and u are the mean and fluctuating component, the subscripts i, j, k correspond to η, y and ζ directional components respectively. Taking the curl of equation (3.12)

$$\frac{\partial \vec{\omega}}{\partial t} + \vec{\nabla} \times (\vec{\omega} \times U) = -\vec{\nabla} \times \left(\vec{g} \frac{\rho^*}{\rho_0} \right) + \nu \nabla^2 \vec{\omega} \tag{3.13}$$

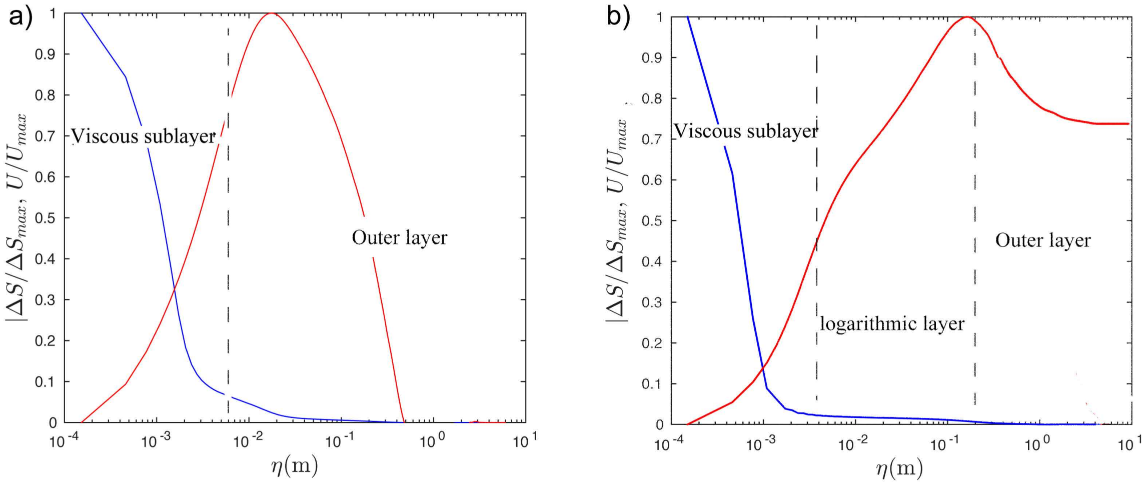

Figure 3.13: Domain averaged profile of normalised salinity anomaly(blue) and normalised mean velocity, $U = \sqrt{U_\zeta^2 + U_b^2}$ (red) as a function of the wall-normal distance (η), for (a) purely convective boundary layer and (b) $U_b = 0.1$ ms^{-1}. The horizontal axis is logarithmic. Based on the profile of velocity the boundary layer is divided into viscous sublayer (characterised by uniform velocity gradiant), logarithmic inner layer (characterised by logarithmic velocity profile) and outer layer.

. Here, ω is the total vorticity, comprised of the fluctuating (ω') and mean (Ω) component, $\omega = \omega' + \Omega$. In index form (3.13) can be simplified as

$$\frac{\partial \omega_i}{\partial t} + U_j \frac{\partial \omega_i}{\partial x_j} - \omega_j \frac{\partial u_i}{\partial x_j} \simeq \epsilon_{i,j} \frac{g_i}{\rho_0} \frac{\partial \rho^*}{\partial x_j} + \nu \nabla^2 \omega_i \tag{3.14}$$

The 2nd and 3rd terms are the vortex tilting and vortex stretching respectively, both of which scales as U_c^2/δ^2. Here, U_c is the characteristic velocity of the system and δ is the thickness of the velocity boundary layer. For a quasi-steady turbulent flow the first term in (3.14) can be dropped. Considering the first order effect only, we retain the vortex streatching term of equation 3.14. If the flow is convectively driven the dominant component of the last term of equation 3.14 is

$$\frac{g \sin\theta \beta \Delta S}{\delta}. \tag{3.15}$$

Therefore equation 3.14 can be simplified as,

$$\frac{U_c^2}{\delta^2} \sim \nu \nabla^2 \omega + \frac{g \sin\theta \beta \Delta S}{\delta}. \tag{3.16}$$

Here δ is the thickness of the salinity boundary layer. For a turbulent convective

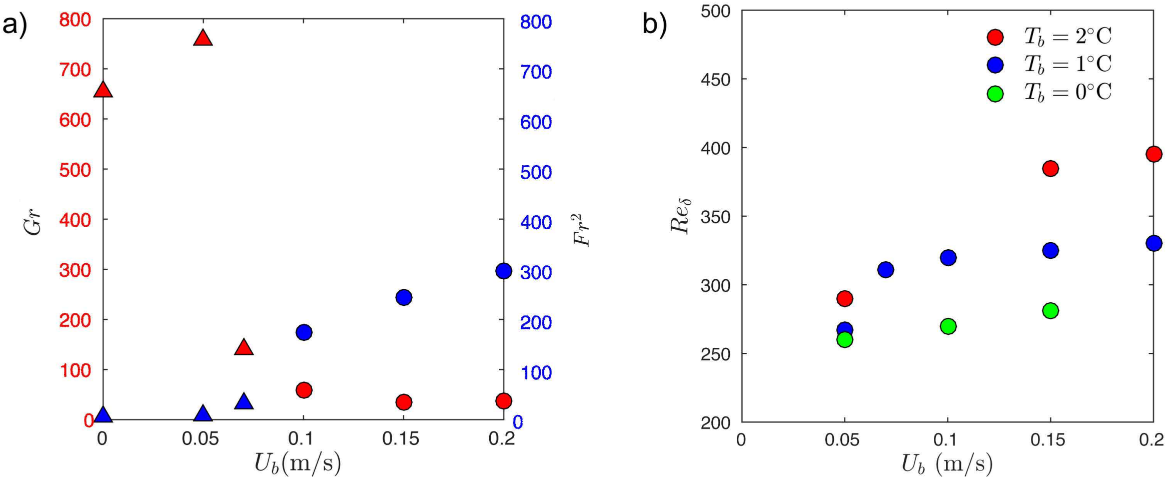

Figure 3.14: (a)Local Froude number, Fr^2_{local} and Grashof number, Gr_{local} plotted as a function of ambient velocity U_b for $T_b = 1°$ C. The triangles and circles represent a convection dominated and shear dominated flow field respectively. (b) Local friction Reynolds number is plotted as a function of background velocity U_b, estimated for three different ambient temperature, $T_b = 0°$ (green dots), $T_b = 1°$ (blue dots) and $T_b = 2°$ (red dots) respectively.

boundary layer the characteristic velocity scales with plume velocity $U_c \sim U_\zeta$. The effective balance in the above equation occurs between

$$\frac{U_\zeta^2}{\delta^2} \sim \frac{g \sin\theta \beta \Delta S}{\delta}. \tag{3.17}$$

This gives back the convective scaling found in (2.16) in Chapter 2. In contrast, for a strong ambient current turbulent activities at the ice wall are predominantly caused by the shear at the ice wall. Here the characteristic velocity scales with the ambient current $U_c \sim U_b$. In such cases turbulent eddies are uncorrelated to the the buoyancy anomaly. Vigorous mixing in the inner layer makes the buoyancy an insignificant component in the momentum equation. Within the logarithmic layer, viscous force starts to dominate over the buoyancy force.

$$\nu \nabla^2 \omega > \frac{g \sin\theta \beta \Delta S}{\delta}. \tag{3.18}$$

The above relation is further simplified as

$$\frac{\nu U_b^2}{\delta^2} > g \sin\theta \beta \Delta S \tag{3.19}$$

$$\text{or, } \frac{U_b^2}{g\beta\Delta S\delta} > \frac{g\sin\theta\beta\Delta S\delta^3}{\nu^2}. \tag{3.20}$$

If we define local Froude number as $Fr_{local} = U_c^2/g\beta\Delta S\delta$ and local Grashof number as $Gr_{local} = g\sin\theta\beta\Delta S\delta^3/\nu^2$, (3.20) reduces to

$$Fr_{local}^2 > Gr_{local}. \tag{3.21}$$

Above scaling is validated by plotting the local Froude number as a function of the local Grashof number in figure 3.14a for $U_b = 1$ ms^{-1} with $T_b = 1$°C. Here both the Fr_{local} and Gr_{local} are calculated based on the salinity boundary layer thickness, δ_S. For an $U_b > 0.07$ ms^{-1}, the Gr_{local} is below 180 and is dominated by the local Fr_{local}. Once the flow is fully shear driven regime, the thickness of the diffusive sublayer and hence the meltrate is controlled by the effective balance between inertial and viscous force,

$$\frac{U_b^2}{\delta} \simeq \nu\frac{U_b}{\delta^2}. \tag{3.22}$$

or,

$$\delta \sim \frac{\nu}{U_b} \implies Re_\delta = \frac{U_b\delta}{\nu} \sim constant \tag{3.23}$$

In figure 3.14b, the Reynolds number, Re_δ based on boundary layer thickness is plotted as a function of the ambient flow, U_b. With increasing values of U_b, the flow becomes shear driven and is predicted by equation 3.23. Re_δ asymptotically reaches a constant values for each driving temperature as shown in figure 3.14b. The above scaling is similar to what was suggested by Wells and Worster [2008] for a thermally driven convective boundary layer from iso-thermally heated vertical plate at very large $Gr > 10^{21}$. The above results indicate that for the shear-driven melting boundary layer under the larger current velocities, thickness of the boundary layer is uncoupled from the scalar fluxes and is indifferent to the buoyancy force.

3.5 Conclusions

The direct numerical simulations show that turbulent heat transfer rate depends on the ambient current speed and the convective boundary layer dynamics. Two flow regimes were found depending on the relative contributions of convection and mean shear towards the production of the boundary layer turbulence. When the boundary layer is convectively driven under a moderate ambient current, meltrate is indpendent of the strength of the ambient current and is given by the convective scaling [Mondal et al., 2019]. In this regime the meltrate is dependent on the thermal forcing and the ice face inclination. For a convective boundary layer the buoyancy anomaly produces an up-slope plume flow. The turbulent transport at the wall is controlled by the turbulent eddy lengthscale at the inner boundary layer. As this flow is driven by buoyancy anomaly the maximum velocity always tends to occur closer to the ice wall. The size of the eddies at this inner layer scales with the thickness of the velocity boundary layer which tends to remain constant with height. However with added forcing by the ambient current, momentum disperses in the wall-normal direction. Beyond a critical speed of the ambient current, the dispersion of the salinity gradient weakens the buoyancy anomaly to such an extent that buoyancy has negligible contribution towards turbulent production. The stress at the wall is then determined by the ambient flow strength. The balanace between viscous, buoyancy and Reynolds stress sets the width of the viscous sublayer which in turn controls turbulent meltrate of the ice wall. The simulations show that this transition occurs when the ambient current speed is $U_b \geq 0.07$ ms^{-1}. In this shear driven regime the meltrate can be represented as,

$$V \sim C_d^{1/2} u^* \Delta T. \tag{3.24}$$

where, C_d is a constant drag coefficient with a value 0.001. Over a shear driven ice-ocean boundary layer, vortex rolls form at the ice wall that are advected and stereteched in the mean flow direction. Increase in vorticity due to vortex stretching is followed by an increase in plume velocity and a reduced thickness of the boundary layer that results in an increased meltrate. For a convectively driven flow, the local stratification caused by the melt water suppresses the formation of such vortex structures and the turbulent transports are predominantly contributed by the plume velocity. The turbulent kinetic energy budget shows that for a shear driven boundary layer turbulence is mostly produced by the shear production. On the otherhand, in a convection driven boundary layer turbulence is contributed both by buoyancy production and shear production. In a geophysical scenario the tidal currents under Antarctic Ice cavities are often less than 0.07 ms^{-1} with background temperature $T_b = -1°$C [Padman et al., 2018]. In such cases convection plays a dominant role and the meltrate follows the convective parameterization (3.10).

We conclude that the ice-ocean parameterizations should incorporate both the effects of convection and ambient shear as represented by equation 3.10 and 3.24 respectively. A simple approach would be to use a heaviside function that estimates meltrate either by convective scaling or shear driven scaling based on ambient flow condition. A modified parameterisation is likely to improve the estimations of the meltrate of the basal area under Antarctic ice-shelves.

Chapter 4

Effects of subglacial discharge under sloping ice shelves of Antarctica

Direct numerical simulations are used to study the effects of subglacial discharge under a sloping ice-shelf. Numerical experiments are carried out in a uniform ambient temperature, $T_b = 2.3°\text{C}$ and salinity $S_b = 35$ g kg^{-1} at different discharge rates from a line source. The slope of the ice-shelf is varied from vertical ($\theta = 90°$) to shallower slopes with $\theta = 50°$. For a non-dimensional buoyancy, $B^* \geq 5$ the plume velocity is almost independent with the along-slope distance for a fully developed boundary layer flow. Estimated plume velocity is well predicted by the modified theoretical scaling based on the plume theory. Over steeper angle, the simulated meltrates are more sensitive to the source buoyancy and are predicted by the buoyant plume model. Over shallower angles the effects of B_s becomes less significant due to the development of local stratification at the ice wall in presence of fresher discharge from melting of ice face.

4.1 Introduction

The melting of the polar ice caps has an important impact on the ocean circulation and the global climate. Ocean driven melting is one of the major drivers of the mass loss in both Antarctica and Greenland Rignot et al. [2013]. The meltwater flux from tidewater glaciers in Greenland and Antarctica is a significant contributor to global sea level rise and is impacting the global thermo-haline circulation Golledge et al. [2019]. Despite the importance of ocean driven ice sheet melting, our understanding of the fundamental processes of the boundary layer dynamics is not complete Rignot et al. [2019]. In particular, there remains a degree of uncertainty regarding the transport of heat and salt from the ambient ocean to the ice face van Wessem et al. [2018]. Since these transports directly control the meltrate of the ice face it is important to fully understand how they are affected by flow properties and ice-ocean geometry.

Although mass loss from Greenland and Antarctica are causing comparable amounts of global sea level rise there are several important differences between the two ice caps. There are two related differences that are important for this study. First, air temperatures around Greenland tend to be warmer than those around Antarctica leading to greater surface melt Serreze and Barry [2011]. As such, the hydrology of

Greenland is more dynamic and is generally seen as a more important component of the local climate. Second, Greenlandic glaciers typically terminate in near vertical ice cliffs Rignot et al. [2015]; Moyer et al. [2017] while Antarctic glaciers typically terminate in near horizontal floating ice shelves. These two differences mean that although the two ice caps are being driven by similar forcing (increasing global temperature), the response of the glaciers and, in particular, the ice-ocean interactions can be dynamically very different.

Around Greenland, a significant portion of the ice melt is co-located with areas of subglacial discharge. Meltwater from the surface of the ice sheet flows to the base of the ice sheet and through a network of subglacial channels and lakes until it reaches the surrounding fjords. The meltwater is then released as a freshwater plume that rises up the glacier face due to its own buoyancy. As a result of high flow velocities, and associated entrainment, these subglacial plumes are associated with elevated meltrates and as such have been the subject of much recent interest.

Observations of subglacial plumes in Greenland have shown that the meltwater can be released at the grounding line as either a point source or a distributed (line) source Hewitt [2019]. The subglacial discharge is typically assumed to be released of fresh water, at (or very close to) the local freezing point. After being released into the fjord, the freshwater rises as a turbulent plume, entraining ambient fluid as it rises. The entrainment of ambient fluid into the plume acts to transport heat and salt to the ice face and is responsible for the enhanced meltrate. Typically, the buoyancy flux of the discharged fluid is much greater than that added as the ice melts such that the buoyancy flux of the plume can be considered uniform with depth Motyka et al. [2013]; Salcedo-Castro et al. [2011]; Sciascia et al. [2013b]; Beaird et al. [2015]; Fried et al. [2015].

Numerical models have frequently been used to study the melting caused by subglacial plumes around Greenland. Such models typically utilise numerical grids that are larger than the scale of the underlying processes. In particular, the ice-ocean interactions are heavily parameterized and the dynamics are simplified. Ice-ocean interactions are modelled using the "three-equation model" which allows the meltrate to be predicted based on larger scale flow variables Holland and Jenkins [1999]. Use of the three-equation parameterization implicitly assumes that the boundary layer structure is controlled by shear McConnochie and Kerr [2017] and models the turbulent transport of heat and salt with constant thermal and saline Stanton numbers. This parameterization is often uncoupled to the grid resolution which results in large uncertainties in the prediction of flow properties including the meltrate Gwyther et al. [2015].

The three-equation model has been used to model the melting caused by subglacial plumes in the form of two-dimensional wall plumes Carroll et al. [2015] and cylindrical line plumes Slater et al. [2016b, 2017] with the plume velocity estimated from plume theory. Results from these numerical studies are consistent with field observations that link regions of subglacial discharge with elevated meltrates. In the case of a line discharge, simulations suggest that both the plume velocity and the meltrate will increase like the discharged buoyancy flux to the 1/3rd power.

Regional scale numerical studies are able to predict meltrates and plume properties based on the parameterizations contained within the models. However, they have limited ability to test those parameterizations or to probe the underlying physical processes. For this reason laboratory or turbulence resolving simulations are needed to investigate ice-ocean interactions from a more fundamental perspective. Although such studies are, by necessity, conducted at much smaller scales than those that are geophysically relevant, they are able to test the small scale processes that are parameterized in larger scale numerical models.

Two recent experimental studies have investigated the particular case of a subglacial discharge applied at the base of a vertical ice face McConnochie and Kerr [2017a]; Cenedese and Gatto [2016]. Consistent with numerical simulations, the experiments demonstrate that the presence of a subglacial discharge increases the turbulent transfer rate and leads to more rapid melting of the ice face. Experiments also showed that beyond a threshold value of the source buoyancy, the dynamics of the plume become independent of the distributed wall buoyancy from the melting ice face alone. McConnochie and Kerr [2017a] developed a model for plume properties (e.g. plume width, velocity, volume flux, and momentum flux) based on two-dimensional line plume theory Fischer et al. [2013]. Both the model and experimental results agree with regional scale numerical results to show that over a vertical ice-interface, the observed plume velocity and the meltrate increase like the source buoyancy to the 1/3 power Straneo and Cenedese [2015].

Although subglacial discharges are typically associated with Greenland rather than Antarctica, there is reason to believe that they could be important to the melting of Antarctic ice shelves as well. Based on satellite laser altimetry data, at least 145 subglacial lakes are distributed around Antarctica Fricker et al. [2007]; Siegert [2005]; Gray et al. [2005]; Wingham et al. [2006]. Most of these subglacial lakes are small (area less than 100 km^2) and are produced from fresh meltwater. Large sporadic releases of subglacial water from these lakes can result in drainage rates up to 100 m^{3}s^{-1} Fricker et al. [2007]. This huge discharge of fresh water can be released at the base of an ice shelf where it would flow up the ice-ocean interface as a fast moving buoyant plume. Just as in Greenland fjords, these locations would be expected to experience enhanced meltrates. It has been proposed that enhanced melting at such plume locations could undercut the ice base and channelise the meltwater laden plume producing a positive feedback mechanism where locally enhanced meltrates would be maintained Berger et al. [2017]; Fricker et al. [2009]; Le Brocq et al. [2013]; Marsh et al. [2016]; Rignot and Steffen [2008]; Sergienko [2013].

Field observations of subglacial discharges are extremely limited around Antarctica due to unpredictable nature of the discharge. As noted, most of the subglacial conduits at the West Antarctic Ice Shelf are formed under a sloping ice face Berger et al. [2017]; Fricker et al. [2007], where the plume dynamics are even more complex than for a vertical ice face. There are very few high resolution observations available under these plume channels and the dynamics of the subglacial discharge plume are not well understood. Fricker et al. [2009] Fricker & Scambos 2009, reported measurements of the meltrate in the lower part of the Mercer and Whillans ice stream in

West Antarctica of 24±3 m yr^{-1}, compared to the background meltrate of 4 m yr^{-1}. Observations at Lake Conway of Mercer ice-stream [Le Brocq et al., 2013] reported an average meltrate of 4.8 m yr^{-1}.

It is expected that many of the dynamic features of a subglacial discharge will be unchanged in the context of an Antarctic ice shelf. However, there are several crucial differences. First, the length scales of the flow are much larger in Antarctica. As a result, the buoyancy flux due to melting will become important at some point along the ice shelf. Secondly, the sloping ice face will have a significant effect on the dynamics of the plume. A sloping ice face will result in a component of gravitational force normal to the direction that the plume flows and as such the plume is likely to become stratified. How this stratification affects the transport of heat and salt from the ambient fluid to the ice face, and hence the meltrate, is currently unclear.

Recent experimental McConnochie and Kerr [2018] and direct numerical simulation (DNS) Mondal et al. [2019] studies have investigated the effect of slope on the melting of an ice face into initially quiescent salt water. It has been shown that the meltrate is a strong function of the ice angle with shallower slopes experiencing significantly reduced meltrates. The DNS results show that under a sloping interface, a stable stratification develops in the plume and this has been used to explain the reduced meltrate. These results are also consistent with recent large eddy simulations which highlighted the possibility of a strongly stratified regime where the meltrate is significantly reduced Vreugdenhil and Taylor [2019].

Despite the observed importance of both slope and subglacial discharge on the meltrate of a planar ice face, the combined effect of both slope and subglacial discharge has never been investigated. Given the possibility of subglacial discharge flows beneath Antarctic ice shelves, there is a need to understand how the meltwater plume and meltrate of the ice could be affected. In this study, we present the first direct numerical simulations of melting under a sloping planar ice interface in the presence of an external freshwater plume. The simulations are designed as a model for a subglacial discharge event. However, it is worth noting that the simulations also shed light on the ice-ocean interactions at large distances from the grounding line without a subglacial discharge. Such large distances are not feasible in direct numerical simulations or laboratory experiments but they are characterised by large buoyancy fluxes in the under-ice plume. As such, the simulations presented hereafter have the secondary purpose of assessing the flow under an ice-shelf at large distances from the grounding line.

4.2 Problem formulation

The flow field is solved in a rectangular domain of a length L, in the direction parallel to the ice face, depth W, normal to the ice face and a width D in the spanwise direction as shown in figure 4.1. The ice-wall is placed on the left side of the domain while an open boundary is placed on the opposite far right of the melting interface. The whole domain is rotated with respect to the horizontal direction by an angle θ,

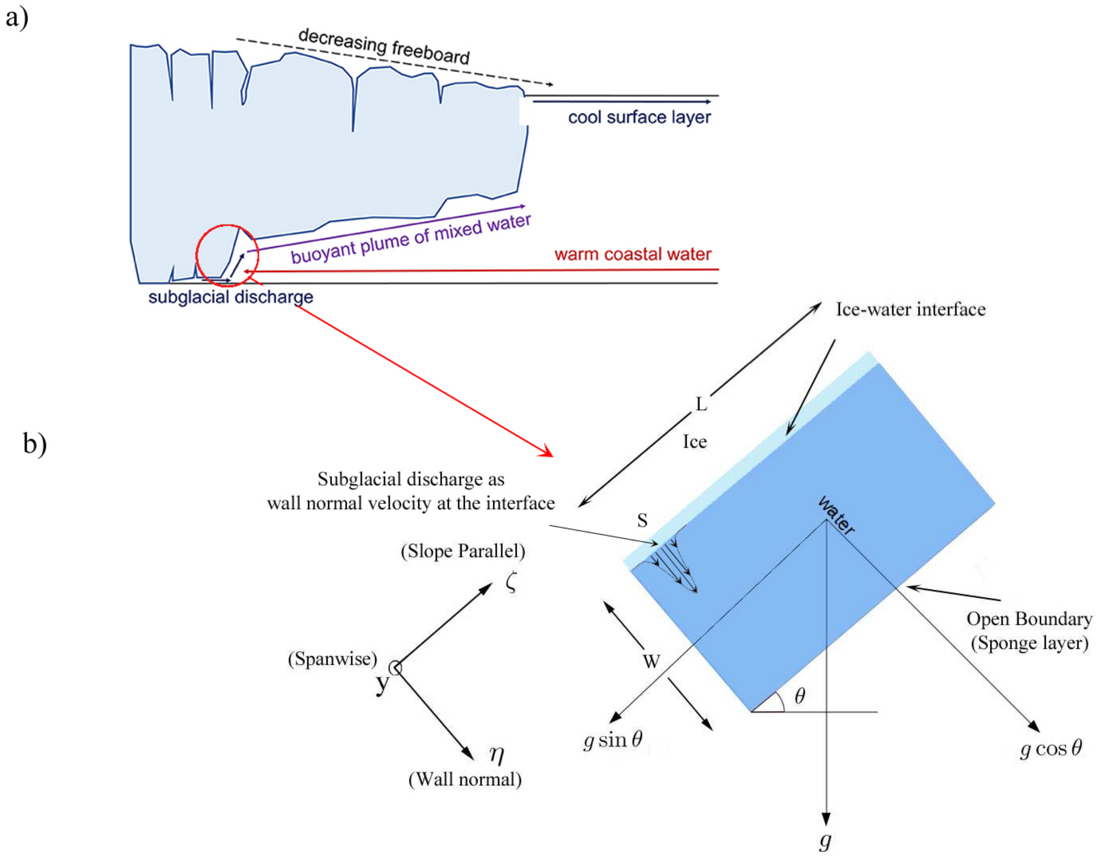
a)
decreasing freeboard
cool surface layer
buoyant plume of mixed water
warm coastal water
subglacial discharge
b)
Ice-water interface
L
Ice
Subglacial discharge as
wall normal velocity at the interface
S
water
(Slope Parallel)
ζ
(Spanwise)
y
η
(Wall normal)
W
θ
$g \sin \theta$
Open Boundary
(Sponge layer)
$g \cos \theta$
g

Figure 4.1: a) Real world schematic of subglacial discharge at the grounding line of a sloping ice-shelf [Moyer et al., 2017]. b) Schematic of the simulation domain. The ice face of length L is in contact with seawater beneath at ambient temperature T_w and salinity S_w. The ice face is sloped at an angle $\theta = 10°$ with the horizon. The discharge flux is added from the side boundary near base by prescribing wall-normal velocity with a Gaussian profile. The far right of the ice-wall is an open boundary where a sponge layer is placed [Mondal et al., 2019].

while the gravity direction is always acting downward. The flow filed is represented by $\tilde{\mathbf{u}}$=[u_η, v, u_ζ] where u_η, v and u_ζ are in the wall-normal (η), spanwise (y) and along-slope (ζ) direction respectively. Co-ordinate systems and velocities are measured relative to the fixed planar ice-water interface as discussed in [Mondal et al., 2019]. We solve the incompressible continuity, Navier-Stokes, heat and salt flux equations as follows

$$\nabla \cdot \tilde{\mathbf{u}} = 0 \tag{4.1}$$

$$\frac{\partial \tilde{\mathbf{u}}}{\partial t} + (\tilde{\mathbf{u}} \cdot \nabla)\tilde{\mathbf{u}} = -\frac{1}{\rho_0}\nabla p^* + \nu \nabla^2 \tilde{\mathbf{u}} + \frac{\rho^*}{\rho_0}(\hat{i_\eta}\frac{\rho^*}{\rho_0} g \cos\theta - \hat{i_\zeta}\frac{\rho^*}{\rho_0} g \sin\theta) \tag{4.2}$$

$$\frac{\partial T^*}{\partial t} + (\tilde{\mathbf{u}} \cdot \nabla)T^* = \kappa_T \nabla^2 T^* \tag{4.3}$$

$$\frac{\partial S^*}{\partial t} + (\tilde{\mathbf{u}} \cdot \nabla)S^* = \kappa_S \nabla^2 S^*. \tag{4.4}$$

Here ρ_0 is the reference density of pure water at 0°C and p^*, T^*, S^* and ρ^* denote the deviation from the ambient hydrostatic pressure, temperature, salinity and density respectively. Also ν is the kinematic viscosity, κ_T and κ_S are the thermal and salinitity diffusivity respectively. We assume a linear equation of state, $\rho^* = \rho_0(\beta S^* - \alpha T^*)$, where α is the thermal expansion, β is the haline contraction coefficient.

The interface flux conditions are solved based on three relations (detailed description of the interface conditions including retreat of inter surface which denoted by meltrate V are found in Gayen et al. [2016] and Mondal et al. [2019]). Freezing point at the ice-interface is assumed to a linear function of interface salinity,

$$T_{int} \simeq a_s S_{int}, \tag{4.5}$$

where a_s is the slope of the liquidus line, $a_s = -6 \times 10^{-2}$ °C g^{-1}kg (Holland & Jenkins 1999). Interface thermal flux balance is considered with ignoring the heat flux into the ice as,

$$\rho_w c_w \kappa_T \frac{\partial T}{\partial \eta}\bigg|_{\eta=0} = \rho_s V L_f, \tag{4.6}$$

where V is the meltrate, L_f is the latent heat of fusion, ρ_s, ρ_w are the density of ice and water. Similarly the salt flux equation at the ice-interface is approximated as,

$$\rho_w \kappa_S \frac{\partial S}{\partial \eta}\bigg|_{\eta=0} = \rho_s V S_{int}. \tag{4.7}$$

The diffusive salt flux in the ice is neglected compared to the diffusive flux at the interface and in the water. We also neglect the effect of mean gradiant $du_\eta/d\zeta|_{\eta=0}$ and ignore the spatial and temporal variations of $u_\zeta|_{\eta=0}$. A sponge layer is applied at the open boundary between $0.5W \leq \eta \leq W$, where along-slope, span-wise velocities and scalar fields are relaxed towards the background state.

The subglacial discharge is added to the domain as an interface condition by prescribing wall-normal velocity with a Gaussian profile from the side boundary near the base as shown in figure 1. The peak discharge point is located at a height of 0.06 m from the bottom of the domain. The discharge flux is initiated by wall-normal velocity that supplies fresh water into the numerical domain at the interface ice-temperature and ice salinity. The discharge flux is added from the side boundary near base. The ejection velocity, u_{eject} of freshwater in the numerical domain is at least an order of magnitude smaller than the maximum plume velocity. In this way it is ensured that the $u_{eject.}$ has negligible contribution to u_ζ at the discharge sight. The gaussian velocity profile with a half width $b = 0.025$ m, maintained for all the simulations. The wall buoyancy flux (B_w) and the discharge buoyancy flux (B_s) are calculated per unit width of the domain using melt rate and ejection velocity as

$$B_w = \frac{1}{L}\int_0^L (V(\zeta)g\frac{\rho^*}{\rho_0})d\zeta, \tag{4.8}$$

$$B_s = \frac{1}{b}\int_0^b (u_{eject}(\zeta)g\frac{\rho^*}{\rho_0})d\zeta. \tag{4.9}$$

Here the unit of the fluxes is m^{2}s^{-3}. The discharge flux is controlled by varying the ejection velocity of the discharge water from 0.3 mm s^{-1} up to 10 mm s^{-1}. Following McConnochie and Kerr [2017a], we define a non-dimensional buoyancy parameter B^* based on total buoyancy flux relative to the wall buoyancy flux from melting the interface,

$$B^* = \frac{B_w + B_s}{B_w}. \tag{4.10}$$

The physical dimension of the domain is kept at $L = 1.8$ m, $W = 0.5$ m and $D = 0.05$ with corresponding grind points $1150 \times 256 \times 64$, in the η, y and ζ directions, respectively with grid stretching in the η direction. Present grid adequately resolve both the thermal and salinity boundary layers along microscales for salinity turbulence. We use the grid convergence criteria proposed by Gayen et al. (2014, 2016) and Mondal et al. [2019]. The simulations are conducted over the slope angle, $\theta = 30^\circ - 90^\circ$. The ambient conditions are maintained at fixed temperature $T_w = 2.3^\circ$C and salinity $S_w = 35$ g kg^{-1} for all the cases. The subglacial discharge velocity is varied from $u_{eject} = 0.003$ ms^{-1}- 0.01 ms^{-1}. The corresponding buoyancy flux is estimated as $B_s \simeq 3 \times 10^{-4}$ m^{3}s^{-3} for $\theta = 50^\circ$ and $B^* = 1$ to $B_s \simeq 1.5 \times 10^{-3}$ m^3/s^3 for $\theta = 90^\circ$ and $B^* = 10$. We use $g = 10$ m s^{-2}, $\kappa_T = 1.285 \times 10^{-7}$ m^2 s^{-1}, $\kappa_S = 7.2 \times 10^{-10}$ m^2 s^{-1}, $c_w = 3985$ J kg^{-1}K^{-1}, $\nu = 1.8 \times 10^{-6}$ m^2 s^{-1}, $\alpha = 6 \times 10^{-5} K^{-1}$ and $\beta = 8 \times 10^{-4}$ g^{-1}kg taken from the physical properties of aqueous NaCl solutions at the far field temperature and salinity (Washburn 1926; Weast et al. 1989). The estimated Grashoff number (relative strength of buoyancy to viscous force, defined as in equation 2.8) in the simulation ranges from $Gr \simeq 1.3 \times 10^{10}$ for $\theta = 20°$ upto $Gr \simeq 10^{13}$ for $\theta = 90°$. Gr, used in these simulations is well above the critical $Gr_c \geq 10^9$ as defined in (2.8) and (2.15), to have a turbulent flow over the domain length [Holman, 2010; Josberger and Martin, 1981].

4.3 Scaling theory

The discharged fresh water from the bottom of the domain along with the fresh meltwater from the ice block drives a buoyant plume and moves in the upslope direction. The average properties of a plume such as plume width, velocity, volume and momentum fluxes are estimated using the conservation laws. Here we revisit the two dimensional wall plume theory by Fischer et al. [2013] in order to derive the average properties of a plume rising from the sloping ice face. Based on the 2D plume theory, the buoyancy flux B_s is applied next to a vertical wall, the average plume velocity is described as

$$\overline{u_{pl}} = 1.66 B_s^{1/3}, \tag{4.11}$$

where velocity is independent of height and only depends on the source buoyancy. The plume width and the volume flux Q, at a height z can be written as,

$$b_{pl} = 0.036z, \tag{4.12}$$

$$Q = 0.34 B_s^{1/3} z, \tag{4.13}$$

z is the height of the plume. Here the prefactors used for the velocity and volume flux depends upon the coefficients of entrainment and drag coefficient. The typical value of the entrainment coefficient based on the average plume velocity is $0.1 - 0.08$ [Ellison and Turner, 1959; Grella and Faeth, 1975; Sangras et al., 1998]. The rate of entrainment is proportional to the plume velocity where the rate of proportionality is know as the entrainment coefficient.

Based on experimental measurements for a vertical plume of buoyant fresh water flowing in an ambient salty water the entrainment coefficient is measured to be 0.071 using a top hat profile of velocity McConnochie and Kerr [2017a]. However for a sloping interface, Ellison and Turner [1959] showed that this entrainment coefficient is not constant, instead a function of the local Richardson number. Recently McConnochie and Kerr [2017a] have modified the line plume theory by considering a fresh water discharge from a line source at the bottom of a vertical ice-block. They reported that the plume velocity and volume flux scale as,

$$u_{pl} = \left(\frac{B_s}{\alpha + C_D}\right)^{1/3}, \tag{4.14}$$

and

$$Q = \frac{\alpha B_s^{1/3} z}{(\alpha + C_D)^{1/3}}, \tag{4.15}$$

respectively. In one hand the ice-wall imposes a drag force on the plume, on the other hand the released buoyant water from melting ice-wall supplies momentum to the flow. Therefore, the buoyancy from the melting acts as a momentum source to the plume and the ice-wall acts as a momentum sink which is further represented by a quadratic drag law. On the outer edge of the plume turbulent entrainment of the ambient fluid takes place.

We derive the plume properties for a freshwater discharge under a sloping ice face. At an along-slope length ζ, the plume has a width of $b_p l$. If we assume that over a slope angle θ, the entrainment coefficient is represented as $\alpha \sin\theta$, the conservation of buoyancy flux, volume flux and momentum flux gives:

$$B_s = b_{pl} u_{pl} \Delta_T. \tag{4.16}$$

$$\tag{4.17}$$

$$\frac{dQ}{d\zeta} = \frac{d(b_{pl} u_{pl})}{d\zeta} = \alpha \sin\theta u_{pl} \tag{4.18}$$

$$\frac{dM}{d\zeta} = \frac{d(b_{pl} u_{pl}^2)}{d\zeta} = b_{pl} \Delta_T \sin\theta - C_d u_{pl}^2 \tag{4.19}$$

where M is the plume momentum flux and Δ_T is the top-hat plume buoyancy. We assume that the length of the domain and the plume velocity remain unchanged ($du_\zeta / d\zeta \simeq 0$). The stress at the ice-wall is assumed to follow a quadratic drag law and is represented as $C_d u_{pl}^2$, with a drag coefficient C_d. Based on equation 4.11 and 4.13 the functional form of the plume width, and the plume velocity can be written in the following form,

$$b_{pl} = c_1 \zeta \tag{4.20}$$

$$\overline{u_{pl}} = c_2 B_s^{1/3}. \tag{4.21}$$

Here c_1, c_2 are constants to be determined. The top-hat plume buoyancy can be

θ	B^*	C_d	α	c2
50°	3	0.030	0.005	1.19
50°	5	0.030	0.010	1.19
50°	7	0.028	0.015	1.19
65°	3	0.028	0.025	1.20
65°	5	0.022	0.030	1.20
65°	7	0.022	0.037	1.20
65°	10	0.022	0.040	1.20

Table 4.1: Estimation of the coefficient c2 based on the simulation parameter.

written as

$$\Delta_T = \frac{B_s^{2/3}}{c_1 c_2 \zeta}. \tag{4.22}$$

Using (4.18) and (4.19) we solve for the constants which are

$$c_1 = \alpha \sin\theta. \tag{4.23}$$

and

$$c_2 = \left(\frac{\sin\theta}{\alpha \sin\theta + C_d} \right)^{1/3}. \tag{4.24}$$

Based on equation (4.23) and (4.24) the final expressions for the plume width and the top-hat plume velocity are,

$$\overline{b_{pl}} = \alpha \sin\theta\zeta \tag{4.25}$$

and

$$\overline{u_{pl}} = \left(\frac{\sin\theta}{\alpha \sin\theta + C_d} \right)^{1/3} B_s^{1/3}. \tag{4.26}$$

The constants are evaluated based on the simulation data over different slope angles as reported in table 1. Here the entrainment coefficient for $\theta = 90°$ is considered as $\alpha = 0.75$ [McConnochie and Kerr, 2017a].

4.4 Result

Melting of an ice face in relatively warmer and saltier water drives a buoyant plume in the up-slope direction. Discharge of fresh water at the bottom of the ice-wall acts as an additional buoyancy source resulting in a stronger plume. As the fresher plume rises up against the wall, it entrains ambient water at the outer edge and the plume gets wider. Figure 4.2a - 4.2c shows the snapshots of the along-slope flow field u_ζ, at

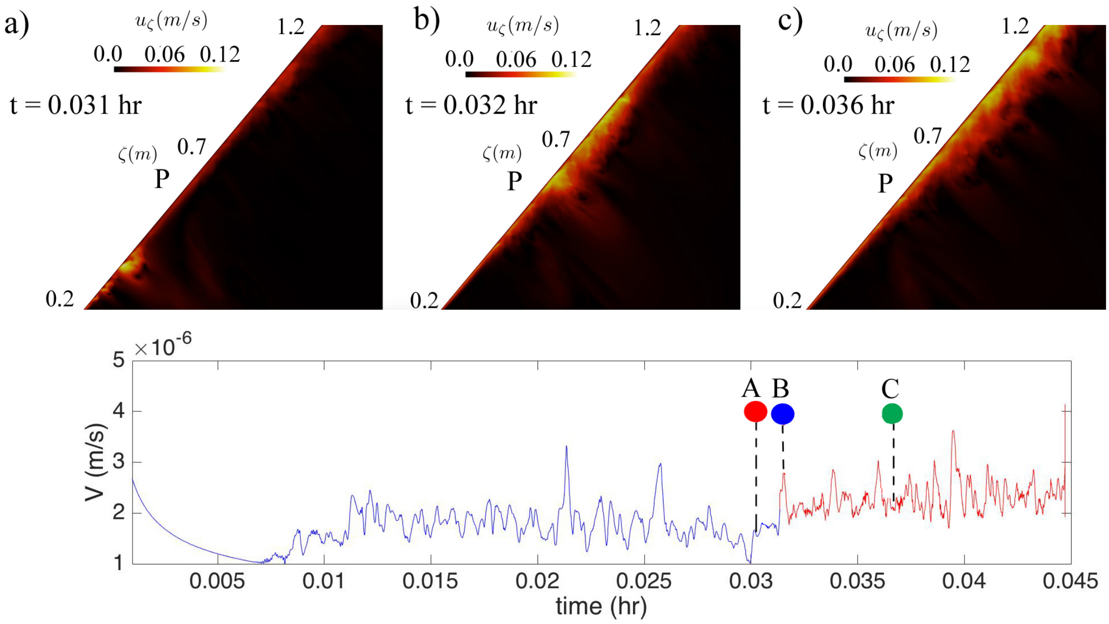

Figure 4.2: Top panel: Snapshots of the along-slope velocity, u_ζ (ms^{-1}) during the passing of the discharge front along the ice face with inclination $\theta = 50°$ at an ambient temperature $T_b = 2.3°$C and ambient salinity $S_b = 35$ g kg^{-1}. a), b) and c) are the snapshots taken at time instants 0.03 hr, 0.032 hr and 0.036 hr respectively, after the initiation of the discharge. Temporal evolution of the spanwise averaged meltrate V (μms^{-1}) at a point P which is at $\zeta = 0.6$ m above the bottom of the domain at the ice-interface. Respective time instants of the flow snapshots are shown on the plot with red (point A, before the discharge), blue (point B, immediately after the discharge) and green (point C, after discharge) dots, respectively.

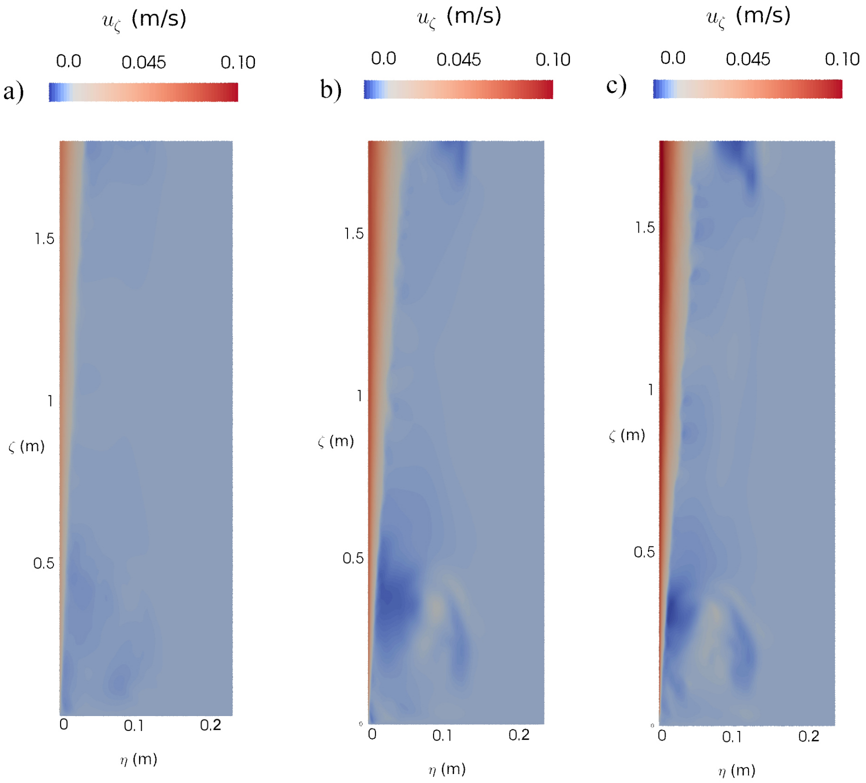

Figure 4.3: Contour of temporal and spanwise averaged along-slope velocity u_ζ (ms^{-1}) for $\theta = 50°$ with similar ambient condition as in figure 4.2, for a) $B^* = 1$, b) $B^* = 5$ and c) $B^* = 7$, respectively.

different time instants to demonstrate the discharge event when constant discharge volume flux, Q (8×10^{-4} m^3s^{-1} for the present case) is maintained at the discharge location with a corresponding $B^* = 5$. After initialization of the discharge from bottom a density front is developed at the lower part of the domain, forming energetic eddies as shown in figure 4.2a. As the density front sweeps across the boundary layer, the along-slope velocity increases resulting in an enhanced turbulence activity. The initial density front separates into two fronts. The faster moving primary front propagates along the interface, while the secondary front entrains ambient fluid and widens the plume in the wall normal direction. Figure 4.2c shows the flow field at $t = 0.36$ hr which corresponds to a later state. The boundary layer becomes more energetic and plume is roughly 5 times wider prior to the discharge event. From the discharge location the width of the plume grows with the along-slope distance. A temporal evolution of the averaged meltrate is measured 0.6 m away from the discharge location as shown in figure 4.2. The average meltrate is increased by 34%, from an initial value of $V = 1.4$ μms^{-1} to an enhanced value of $V = 1.87$ μms^{-1} after the discharge event.

Boundary layer flows and structures settle down to a equilibrium state after the

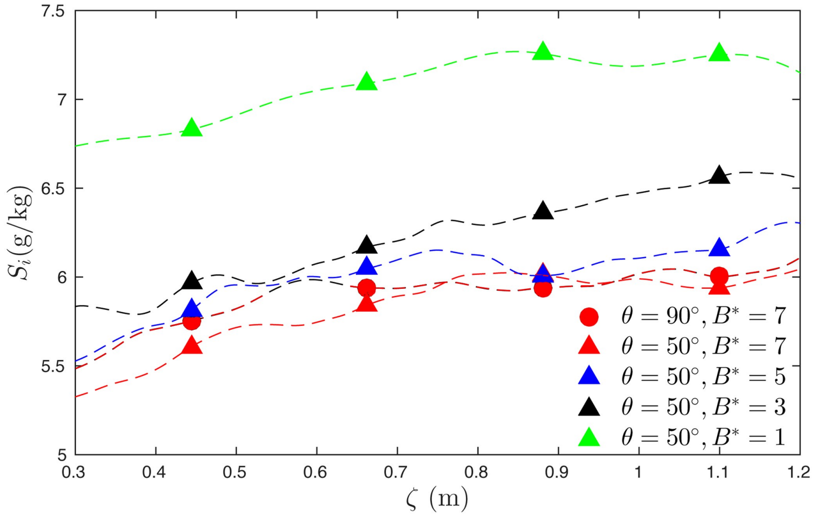

Figure 4.4: Along-slope profiles of the temporally averaged (over 100 buoyancy period) interface salinity, S_i (g kg^{-1}). Triangles and circles represent $\theta = 50°$ and $\theta = 90°$ respectively at different B^* values. $B^* = 1$ represents no discharge case. Uniform ambient temperature, $T_b = 2.3°$ C and salinity, $S_b = 35$ g kg^{-1} is used here.

discharge event. The spatial and temporal averaged plume structures for a $\theta = 50°$ over different B^* values are shown in figure 4.3. Figure 4.3a represents a flow driven only by the distributed wall buoyancy ($B^* = 1$). As the plume flows over the ice face it becomes wider compared to the non-discharge case. The plume velocity increases with increasing discharge flux. A downwelling is observed in the lower part ($\zeta < 0.5$ m) of the domain by the negatively buoyant cold water adjacent to the discharge plume.

Along-slope profiles of interface salinity, S_i for two different slope angles, ($\theta = 50°$ and $\theta = 90°$) are shown in figure 4.4 with different source buoyancy at the quiescent ambient. The profile of a zero source buoyancy flux ($B^* = 1$) is almost independent of the along-slope distance with an average value of $S_i = 6.8$ g kg^{-1}. With added buoyancy ($B^* \geq 3$), S_i gradually increases from the bottom of the domain. Over this region the flow is still transitioning into turbulence and the main plume is entraining a large amount of ambient salt water. The transition length typically varies from $\zeta = 0.8$ m for $\theta = 90°$ to $\zeta = 1$ m for $\theta = 50°$. For $B^* = 1$, the averaged S_i over the top-half of the domain is 38% higher for with $\theta = 50°$, compared to $B^* \geq 3$.

Averaged along-slope (ζ) profile of the maximum plume velocity as function of the along-slope distance for different discharge cases are shown in figure 4.5. For a purely distributed wall buoyancy (shown by the green triangles) the plume velocity consistently increases with ζ. With added source buoyancy the plume is gradually becoming length independent with increasing B^*. For $B^* \geq 5$ the plume velocity is almost becoming independent of ζ. This feature is more prominent for a vertical ice face. With higher source discharge the plume velocity becomes less dependent on the along-slope length (comparing $B^* = 3$ and $B^* = 7$ for $\theta = 50°$).

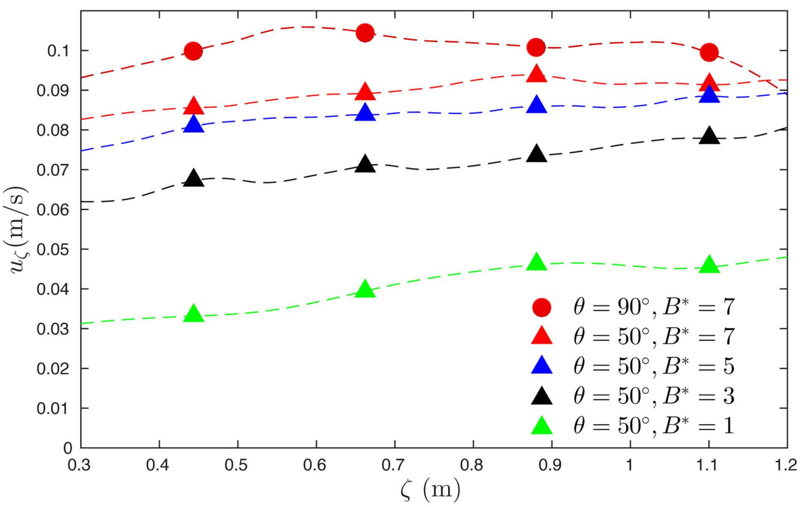

Figure 4.5: Temporally averaged along slope profile of maximum plume velocity, u_η over the plume witdth $b_T(\zeta)$ at an along slope distance ζ. The averaging is done for 100 buoyancy periods once the initial gravity current front has subsided. Symbols and ambient conditions as in figure 4.4.

Figure 4.6a represents the wall-normal profile of the plume velocity for a vertical and inclined interface. For a vertical interface, a top-hat velocity profile is observed and the plume is much wider. Similar profiles are absent with $B^* = 7$. The solid line represents the boundary layer structure for $\theta = 50°$. It is noted that the thickness of the velocity boundary layer shrinks with the increasing B^* value. For $B^* = 3$ as shown by the black line in figure 4.6a disperses momentum more gradually and the outer edge of the boundary layer is at $\eta = 0.2$ m. Compared to this when $B^* = 7$ and $\theta = 50° theouteredgeoftheplumeendsat \eta = 0.05$ m. Figure 4.6b shows profiles of the averaged along slope velocity replotted as a function of the wall co-ordinate. The plot reveals that the shear at the ice-wall is still higher for $\theta = 50°$ when compared to a vertical wall. For shallower slopes the maximum plume velocity is more sensitive to the B^*. Based on (4.26) and table 1,

$$\frac{\overline{u_{\zeta,\theta=50°}}}{\overline{u_{\zeta,\theta=90°}}} = \frac{k.B^{*1/3}}{1.09k.B^{*1/3}}, \tag{4.27}$$

where k is estimated as 1.44. The red and black line correspond to theoretical scaling for u_ζ for $\theta = 90°$ and $\theta = 50°$ respectively. The theoretical estimation matches quite well with the simulated values.

In figure 4.7, the steady state plume velocity is plotted as a function of the B^* for $\theta = 50°$, $65°$ and $90°$. The plume velocities increases with applied B^* value. The plume velocities are well represented by the theoretical scaling (4.26 (as shown by the red curve), for steeper slope angles. For shallower slopes the mean plume velocity is less sensitive than the source buoyancy.

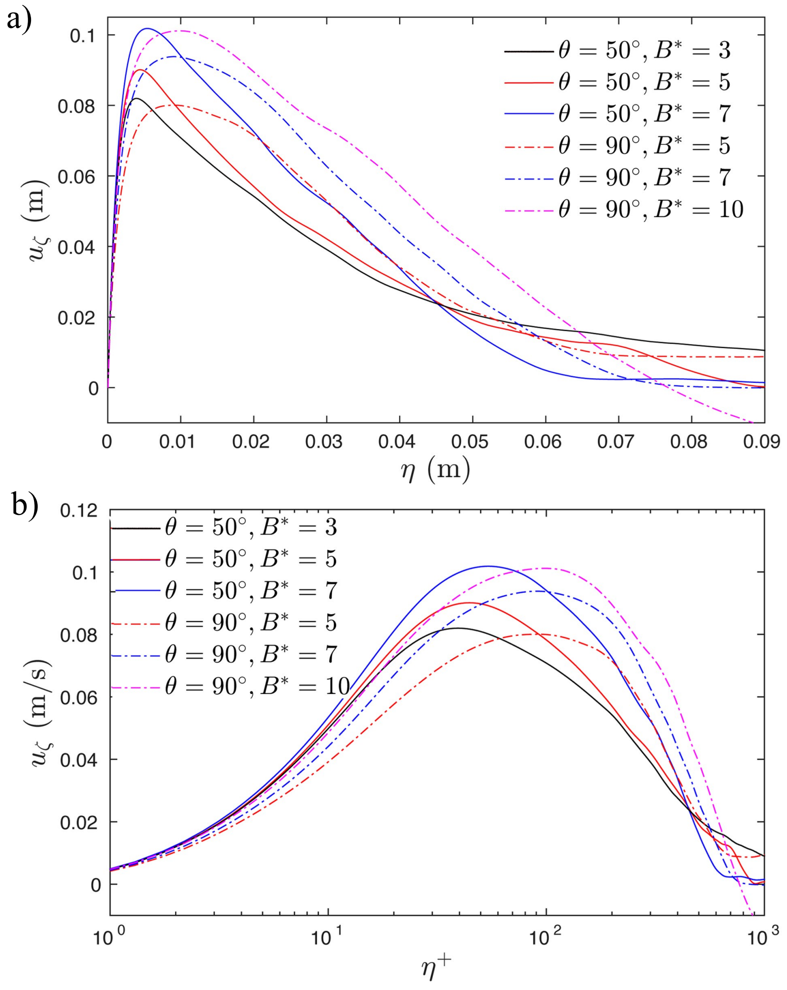

Figure 4.6: Temporal and spatial averaged plume velocity u_ζ (ms^{-1}) as a function of B^* for slope angle $\theta = 50°$, 65° and 90° respectively. The red and black lines are the theoretical u_ζ(m) based on equation and respectively.

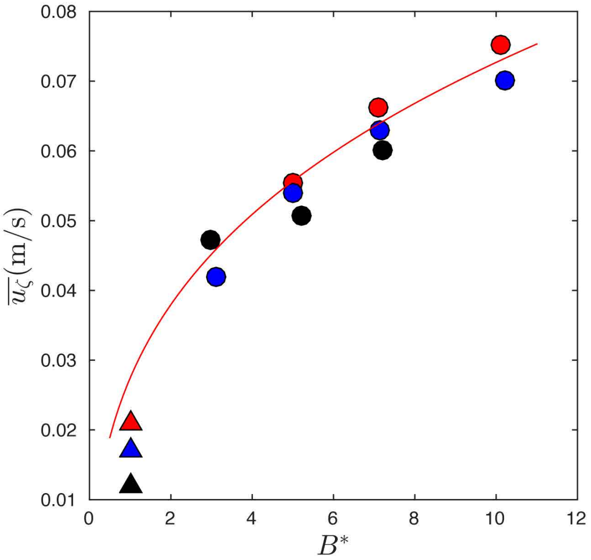

Figure 4.7: Temporal and spatialy averaged plume (over the plume width) velocity $\overline{u_\zeta}$ (ms^{-1}) as a function of B^* for slope angle $\theta = 50°$ (black symbols), 65° (blue symbols) and 90°(red symbols) respectively. The red line is based on the theoretical scaling based on equation (4.26). The triangles represents average plume velocity without external source buoyancy

In figure 4.8 the simulated meltrates are plotted as a function of the up-slope distance for slope angles $\theta = 50°$ (triangles) and $\theta = 90°$ (black circle). The meltrates are estimated by temporal averaging for 100 times the respective buoyancy time period, $N = -\sqrt{g/\rho^*(d\rho\ /d\zeta)}$. For $\theta = 50°$ without subglacial discharge ($B^* = 1$), the meltrate is almost depth independent. With the addition of subglacial discharge the overall meltrate increases upto 40% and is slightly decreasing with the along-slope distance. This trend is even more prominent for $\theta = 90°$ at $B^* = 7$.

The steady state meltrate for different slope angles is plotted as a function of the source buoyancy in figure 4.9. With increasing B^*, the meltrate increases for a given slope angle. However, for shallower slopes V is less sensitive to B^*. The average meltrate increases from $V = 2.4\mu$ ms^{-1} for $\theta = 50°$ and $B^* = 7$ upto $V = 3.1\mu$ms^{-1} for $B^* = 7$ and $\theta = 90°$. For a fixed $\theta = 50°$ the meltrate is 20% higher for $B^* \geq 3$ compared to the no discharge case. For a vertical ice-wall, the addition of the subglacial discharge has feeble effects on the meltrate below a critical value of B^*. McConnochie and Kerr [2017a] reported this transition to occur for a vertical ice-wall above $B^* \geq 3$. For discharge over $B^* \geq 5$ the meltrate increases with the B^* value. This transition is completely absent in the meltrate profiles under a sloping interface. With shallower slope angles the meltrates are less sensitive to the applied B^* values. Fresh discharge water is creating stratification at the ice-interface and suppressing the turbulent eddies.

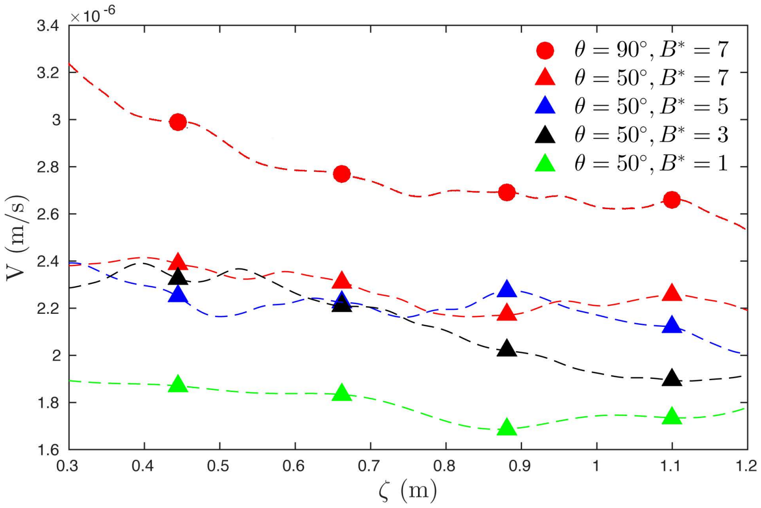

Figure 4.8: Temporally averaged meltrate V (μms^{-1}) as a function of the along-slope distance ζ for different B^* values for slope angle $\theta = 90°$ (circles) and $\theta = 50°$ (triangles) respectively at discrete locations, while the dotted line represents the corresponding continuous values. The meltrates are averaged for 0.05 hr after the discharge front has swept across the domain and the boundary layer plume is at quasi-steady state.

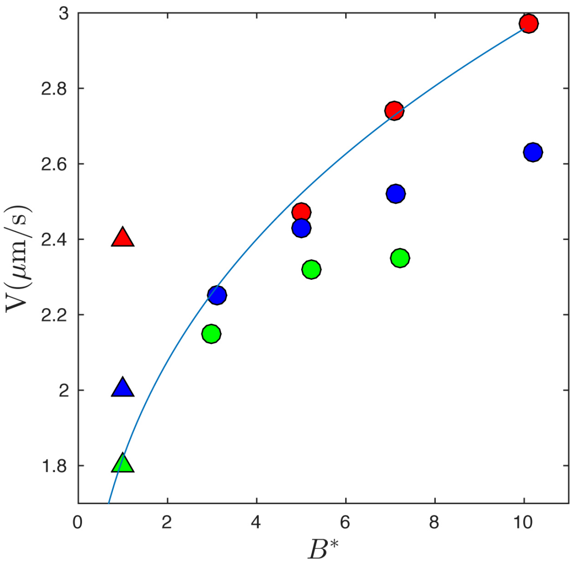

Figure 4.9: Temporal and spatial averaged meltrate V (μ ms^{-1}) as a function of B^* for slope angle $\theta = 50°$ (green symbols), 65° (blue symbols) and 90° (red symbols) respectively. The meltrate is temporally averaged for 0.05 hr and spatially averaged over 0.1 m across the mid-depth, after the discharge front has swept across the domain and the boundary layer plume is resettled to a quasi-steady state.

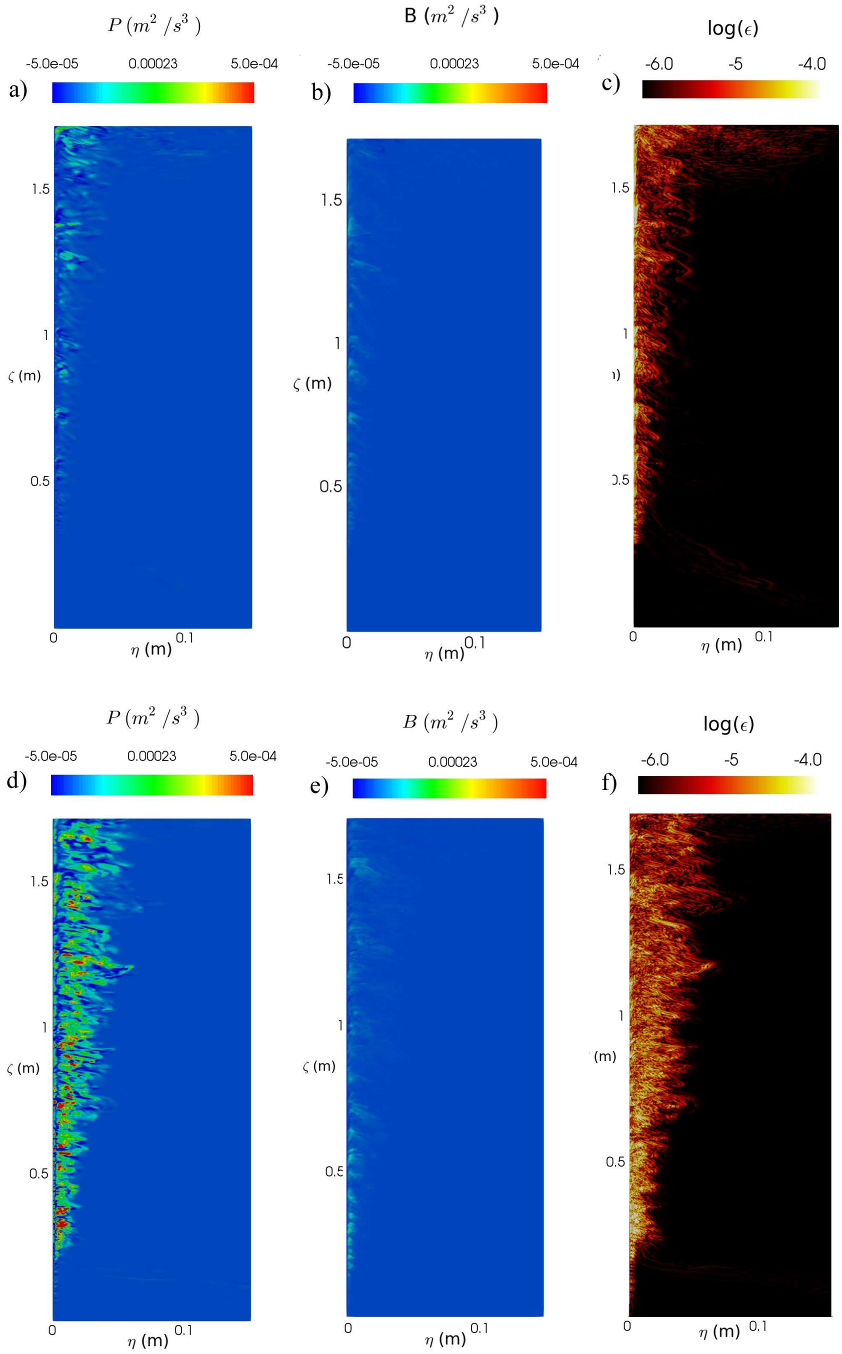

Figure 4.10: Snapshot of the a) turbulent shear production (S), b) buoyancy production (B) and c) dissipation (ε) for $\theta = 50^\circ$ (top panel) and d), e), f) are the corresponding values at the same slope angle with $B^* = 5$.

4.4.1 Turbulent kinetic energy budget

We have investigated the turbulent properties of the boundary layer for different discharge source buoyancy over various slope-angles. The turbulent kinetic energy budget can be expressed as

$$\frac{\partial K}{\partial t} + u_j \frac{\partial K}{\partial x_j} = P - \varepsilon + B - \frac{\partial \Gamma}{\partial x_j}, \tag{4.28}$$

where P is the turbulent shear production

$$P = -\overline{u_i' u_j'} \frac{\partial U_i}{\partial x_j}, \tag{4.29}$$

ε is the rate of turbulent dissipation

$$\varepsilon = \nu \overline{\frac{\partial u_i'}{\partial x_j} \frac{\partial u_i'}{\partial x_j}}, \tag{4.30}$$

B is the turbulent buoyancy production

$$B = -g\overline{\rho' u_\zeta'} \sin\theta + g\overline{\rho' u_\eta'} \cos\theta, \tag{4.31}$$

and the term $\partial\Gamma/\partial x_j$ denotes the turbulent advection of K containing the pressure transport, turbulent transport and viscous transport, given as

$$\Gamma \equiv \overline{p' u_i'} + \frac{1}{2}\overline{u_i' u_i' u_j'} - \nu \frac{\partial K}{\partial x_j}. \tag{4.32}$$

The snapshots of various terms in the turbulent budget are shown in figure 4.10, where terms were temporally and spanwise averaged. Surface contour of turbulent buoyancy production, B shear production, P and dissipations over a slope angle $\theta = 50°$ are shown without any source buoyancy (top panel) and with a $B^* = 7$ (bottom panel), respectively. For a distributed buoyancy source turbulent shear production and buoyancy production are almost equally sustaining to the turbulence. With an added $B^* = 7$, the turbulence in the boundary layer is more rigourous. From a distance $\eta = 0.2$ m from the discharge source there is an increase in the turbulent activities as indicated by the dissipation field. Compared to $B^* = 1$, shear production is much higher here. Over the entire plume turbulence in the boundary layer becomes predominantly sustained by the shear production. Shear production is often higher very close to the wall which is followed by a region of low shear production.

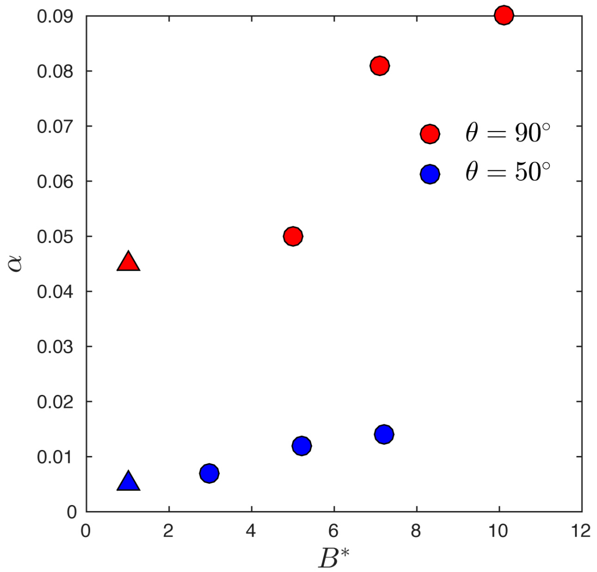

Figure 4.11: Entrainment coefficient α, calculated based on the gradient of the time averaged volume flux, $\alpha = dQ/d\zeta$, averaged over 0.1 m at $\zeta = 1.2$ m, where the plume velocity and the meltrate are weakly dependent on along slope distance. Red and blue dots are α for $\theta = 90°$, and $\theta = 50°$ respectively, red and blue traiangles are the α of the correspoding θ without discharge ($B^* = 1$).

4.5 Discussion and Conclusion

The present chapter has investigated the dynamics of the melting by an external freshwater plume under a sloping interface using direct numerical simulations. We have simulated subglacial discharge plume with varying discharge rates bracketing the conditions found under Antarctic ice-shelves. The plume accumulates fresher water at the source buoyancy next to the ice-wall that is reflected at the inner layer property of the plume. Very close to the discharge source the plume properties (e.g. temperture and salinity) are very similar to the discharged water. As the plume develops over the ice-slope it entrains ambient water and the plume width grows wider. Along the flow direction the plume looses the characteristics of the discharge source due to entrainment and a transition occurs within the plume. Over this transition length (O(0.5 m)) the plume property would no longer be controlled by the source buoyancy and rather by the wall buoyancy. The present domain size is much smaller to capture the effect.

Very close to the discharge source the flow is transitioning into turbulence. The plume is much thinner and huge entrainment is occurring over this region. Once the plume is fully turbulent the plume width increases with the along-slope distance. Over a fixed slope angle and an along-slope distance the plume is wider for a larger source buoyancy B^*. With shallower slopes the increase in plume width with the increasing source buoyancy becomes less prominent. In general, the plume velocity increases with the applied source buoyancy and is well predicted by the theoretical scailing of (4.11). However with shallower slopes the average plume velocity are slightly less sensitive to the theoretical scaling. The simulated meltrates follow the plume velocity and increase with applied B^* values. For a vertical ice face the estimated meltrate closely follows $V \sim B^{*1/3}$ as reported in the observational studies [McConnochie and Kerr, 2017a; Cenedese and Gatto, 2016]. Under a sloping interface meltrate is less sensitive to the applied B^* value. The sensitivity decreases with decreasing slope angle. However, with limited data a concrete functional relationship can not be drawn at this moment.

Over a particular slope angle the turbulent kinetic energy (*tke*) increases with the applied B^* value. Analysis of *tke* budget reveals that, in presence of subglacial discharge the turbulence is predominantly produced by the turbulent shear production over buoyancy production irrespective of the slope angle. This results contradicts the previous *tke* budget for a vertical ice-interface where buoyancy production was a dominant mechanism for the turbulent production.

The sensitivity of the meltrate on the applied B^* as well as on the slope angle, is related to the change in the rate of entrainment of the ambient water into the plume. As the plume entrains more ambient water the a local stratification under the ice-wall is created that opposes the turbulent activities at the ice-ocean boundary layer. Over an inclined the interface the wall normal buoyancy can influence the along-slope momentum by the pressure fluctuation terms Ellison and Turner [1959]. As a result the assumption that the entrainment rate should follow $\alpha = \alpha \sin\theta$ for a slope angle θ may not hold. Below we measured the entrainment coefficient from the plume volume flux based on equation 4.18. Figure 4.11 represents the entraiment coefficients for $\theta = 90^\circ$ (red dots) and $\theta = 50^\circ$ (blue dots) respectively. α seem to be dependent on both the slope angle as well as the strength of the source buoyancy respectively.

At a typical subglacial discharge site in West Antarctica the slope of the ice-shelves can vary between $10^\circ - 40^\circ$. The present study demands further investigations on the effect of subglacial discharge on the meltrate over wider geophysical range of slope angles at large discharge flux, which is beyond scope of the present DNS. In most of this discharge sites undercutting patterns develop at the discharge location that further channelize the flow. Present DNS assumes a planar ice-interface, the evolution of the undercuts and it's effects on the plume flow is still need to be studied with modified DNS code that incorporates the evolution of the ice-ocean boundary. In spite of the limitations, the present study is first of it's kind that describes the effects of subglacial discharge under a sloping interface. The results from the present study shall help to improve the parameterization of the meltrate based on the discharge flux in the basin scale ice-ocean models.

Chapter 5

Conclusion

The effects of convection on the melting of the submerged ice shelves are examined using turbulence resolving simulations. The main focus of this thesis is to understand the nature of the turbulent boundary layer and the subsequent turbulent melting of the ice-face that are sensitive to the ambient flow conditions. The thesis explores geophysical factors like the slope of the ice-shelf, ambient current next to the ice-interface and the effects of subglacial discharge affecting the dynamics of the convecting melt-water plume at the immediate vicinity of the ice-water interface controlling the turbulent transport of salt and heat at the ice-face. Present numerical data successfully resolves diffusive boundary layers and facilitates precise estimations of the diffusive fluxes and the meltrate, otherwise difficult to estimate in a laboratory set up. The three chapters of the thesis are summerised in the following paragraphs.

Chapter 2 explores the effects of the ice-shelf geometry on the convection driven melting. The numerical experiments were conducted for effective Grashof numbers $10^{10} - 10^{12}$, large enough to ensure a fully turbulent flow field. For a purely convective turbulent boundary layer, the diffusive heat transfer is found to be depth independent while the meltrate decreases as $2/3$ rd power of the sine of the slope angles as represented in equation (2.56). The sensitivity of the meltrate with the slope of the ice-shelves arises due to formation of local stratification by the meltwater under the slope that suppresses the eddy transports in the wall-normal direction. This is also reflected in the nature of turbulence produced inside the melt boundary layer. For shallower angles turbulence is predominantly produced by the turbulent shear production whereas for near vertical cases buoyancy production of the turbulence is still significant. Over a larger domain the relative significance of the buoyancy production might be overwhelmed by the stronger shear production.

The relative contributions of convection and ambient velocity shear on the turbulent melting of the sloping ice-face is explored in Chapter 3. Numerical simulations are conducted with ambient currents with values as observed under the ice-shelves ($U_b = 0 - 0.2$ m s^{-1}). The boundary layer at the ice-ocean interface becomes shear driven beyond a threshold background current of $U_b \geq 0.07$ m s^{-1}. With stronger ambient flow a prominent log-layer emerges and the velocity boundary layer extends far beyond the regions of salinity deficit. The shear driven eddies rigorously mix the inner layer and drop the salinity anomaly to such an extent that buoyancy becomes a secondary driver of the flow. This transition is likely to be observed when the local

Froude number surpluses the local Grashof number. Simulations over the periodic domain for an extended period of time in the complete absence of ambient flow also show that the boundary layer can still be shear driven with the emergence of a prominent log-layer. Compared to a convectively driven boundary layer, a shear driven boundary layer is characterised by distinct turbulent micro-structures. Analysis of the vorticity field reveals that ambient flow interacts with the convective flow and forms turbulent vortices due to shear at the ice wall that eventually get stretched in the mean flow direction. The stretching and elongation of the vortices forms smaller and faster eddies with increased eddy transport rate of heat and salt, resulting in higher meltrates. The study explores the limitations of the present ice-ocean parameterization based on buoyant plume theory and provides a parameter regime for the drag coefficient C_d in equation 2.1, facilitating more precise estimations of the meltrate.

In the Chapter 4 we explored the effects of sub-glacial discharge fluxes under the sloping ice-shelves which is more common at the Antarctic ice-front and studied the effect on the melting under sloping ice-shelves. Fresher water from the subglacial discharge location acts as an external buoyancy source to the meltwater plume. Both the plume velocity and the plume width increase with stronger subglaical discharge rate. For an ice-interface with arbitrary slope angle the plume velocity follows a 1/3rd power law to the source buoyancy as well as depends on the wall-drag and the entrainment rate. The turbulent meltrate also increases with increased buoyancy flux. With shallower slopes the meltrate becomes less sensitive to the applied source buoyancy. The estimated entrainment coefficient over various slope angle shows that the entrainment coefficient increases with the applied source buoyancy. Based on the present limited numerical data a concrete functional relationship for the meltrate with the source buoyancy is not established. A theoretical justification of the behaviour of the plume under a slope would be provided in future.

5.1 Discussion and Future work

Overall, the thesis explores the dynamics of the melting of a plane ice-ocean boundary layer down to the diffusive scales otherwise difficult to conduct in a laboratory experiment. Theoretical scalings based on the buoyant plume theory assume a shear driven boundary layer and employ certain symmetries in the flow (cylindrical or wall plume). The present study only focuses on the turbulent transfer processes of heat and salt at the ice-ocean boundary and does not represent the complex flow dynamics inside an ice cavity. The numerical domain is idealised and planar. Spatial evolution of the melting interface is not considered here. A fixed numerical domain implies that the entire domain moves with the interface. The size of the domain limits the largest resolved scale in the simulation O(1 m), therefore the effects of ice-face roughness, stratification and internal wave activities inside ice-cavity, rotation of the earth and open ocean convections are not explored in the thesis. The process of turbulent melting under ice is still an open problem and needs lot more attention with farther turbulence resolving simulations over complicated flow scenario.

The thesis has only investigated the melting process of a fresh ice-block where the heat and salt flux is always from the water into the ice-interface while the freezing at the ice-wall has been excluded. An immediate future work would be to implement similar DNS set up to study the freezing process under sloping ice-shelves. At the base of the grounding line around the Antarctic Ice shelves, the effect of pressure lowers the freezing point. In presence of colder yet relatively saline water, ice melts and drives a fresher buoyant plume next to the ice wall, know as the Ice Shelf Water (ISW). At shallower depths (underneath the overhanging flat portion of the ice shelf), ambient freezing point temperature of the plume increases and the ISW becomes supercool, laden with tiny ice crystals called frazil ice. The frazil crystals can collide with one another and grow in size as a secondary nucleation [Holland and Feltham, 2005; D Jones and Wells, 2018] and can either precipitate at the ice base or get deposited under the overhanging part of the ice shelf. The number and the size distribution of this frazil ice depends on the ambient water mass and flow structures [Feltham et al., 2006]. A layer of vertical ice crystals with sporadic brine channels in between forms at the ice wall, which is known as the mushy layer. Turbulence at the boundary layer controls the growth and the transports of heat and salt across the mushy layer. The formation of frazil ice expels brine into the ambient water that results in a negative buoyancy production. This production of buoyancy can influence the ambient stratification, which can modify the cavity scale circulations. A number of large scale models have studied the sea ice formation [Galton-Fenzi et al., 2012b; Wilchinsky et al., 2015; Jordan et al., 2015] and refreezing under ice shelves [Jenkins and Bombosch, 1995; Khazendar and Jenkins, 2003; Holland and Feltham, 2005]. Recently D Jones and Wells [2018] have models the population growths of frazil ice and have represented a scaling for population explosion of the ice-crystal that significantly influence the plume buoyancy. However no turbulence resolving study has been conducted in this regard and the freezing process under ice wall is parameterized based on large-scale flow structure. It is still very important to understand the nature of the turbulent boundary layer at the freezing interface using turbulence resolving simulations. This DNS study will be carry forward and implemented on a freezing ice-ocean boundary to understand the nature of the turbulence.

The present study is quite significant in the geophysical perspective. Several observations under the ice-shelves of Antarctica reported a range of slope angle [Patton et al., 2016; Dutrieux et al., 2014] under the glacier tongues with parameter ranges the present DNS study. There exist a large region under the ice-shelves where the ambient flow is much weaker [Patton et al., 2016; Padman et al., 2018] and the flow regime is well suited within the convective regime as discussed in chapter 3. Few recent numerical studies have partially addressed this issue and identify a constant drag coefficient can lead to erroneous estimations of the meltrate [Gwyther et al., 2016; Vreugdenhil and Taylor, 2019], specially over the working grid resolution of the large scale models. The results of this thesis therefore motivate further work on the effectiveness of the present parameterization in basin scale models. Based on the analysis of the DNS result we shall implement a modified sub-grid scale parameterization. A diagnostic study would be conducted using ROMS (Regional Ocean Models) MISOMIP (Marine Ice Sheet-Ocean Model Intercomparison Project) model where the sensitivity of the present parameterisation scheme shall be studied in an idealised domain set up. Analysis of these study would tell us how effectively this modifications in the ice-ocean parameterizations can minimize the uncertainty in the future ice-loss prediction. Recent advances in the deep learning based modelling can be another alternative to identify different flow regimes and implement different parameterization schemes accordingly.

Bibliography

Arzeno, I. B.; Beardsley, R. C.; Limeburner, R.; Owens, B.; Padman, L.; Springer, S. R.; Stewart, C. L.; and Williams, M. J., 2014. Ocean variability contributing to basal melt rate near the ice front of ross ice shelf, antarctica. *Journal of Geophysical Research: Oceans*, 119, 7 (2014), 4214–4233. (cited on page 11)

Baines, P. and Sparks, R., 2005. Dynamics of giant volcanic ash clouds from supervolcanic eruptions. *Geophysical Research Letters*, 32, 24 (2005). (cited on page 13)

Beaird, N.; Straneo, F.; and Jenkins, W., 2015. Spreading of greenland meltwaters in the ocean revealed by noble gases. *Geophysical Research Letters*, 42, 18 (2015), 7705–7713. (cited on page 70)

Berger, S.; Drews, R.; Helm, V.; Sun, S.; and Pattyn, F., 2017. Detecting high spatial variability of ice shelf basal mass balance, roi baudouin ice shelf, antarctica. *The Cryosphere*, 11, 6 (2017), 2675–2690. (cited on page 71)

Bindoff, N. L.; Rosenberg, M. A.; and Warner, M. J., 2000. On the circulation and water masses over the antarctic continental slope and rise between 80 and 150 e. *Deep Sea Research Part II: Topical Studies in Oceanography*, 47, 12-13 (2000), 2299–2326. (cited on page 3)

Budd, W. F.; Jacka, T. H.; and Morgan, V. I., 1980. Antarctic iceberg melt rates derived from size distributions and movement rates. *Ann. Glaciol.*, 1 (1980), 103–112. (cited on page 19)

Cameron, R. L. and Bull, G. B., 1962. The thermal diffusivity and thermal conductivity of glacial ice at wilkes station, antarctica. In *Antarctic Research: The Matthew Fontaine Maury Memorial Symposium*, vol. 7, 178–184. Wiley Online Library. (cited on page 12)

Carey, V. P. and Gebhart, B., 1982. Transport near a vertical ice surface melting in saline water: experiments at low salinities. *Journal of Fluid Mechanics*, 117 (1982), 403–423. (cited on pages 8, 18, and 24)

Carey, V. P.; Gebhart, B.; and Mollendorf, J. C., 1980. Buoyancy force reversals in vertical natural convection flows in cold water. *Journal of Fluid Mechanics*, 97, 2 (1980), 279–297. (cited on page 8)

Carroll, D.; Sutherland, D. A.; Hudson, B.; Moon, T.; Catania, G.; Shroyer, E. L.; Nash, J. D.; Bartholomaus, T. C.; Felikson, D.; Stearns, L.; et al., 2016.

The impact of glacier geometry on meltwater plume structure and submarine melt in greenland fjords. *Geophysical Research Letters*, 43, 18 (2016), 9739–9748. (cited on pages 13 and 48)

Carroll, D.; Sutherland, D. A.; Shroyer, E. L.; Nash, J. D.; Catania, G. A.; and Stearns, L. A., 2015. Modeling turbulent subglacial meltwater plumes: Implications for fjord-scale buoyancy-driven circulation. *Journal of Physical Oceanography*, 45, 8 (2015), 2169–2185. (cited on page 70)

Cazenave, A. and Llovel, W., 2010. Contemporary Sea Level Rise. *Ann. Rev. Mar Sci.*, 2, 1 (2010), 145–173. doi:10.1146/annurev-marine-120308-081105. (cited on page 17)

Cenedese, C. and Gatto, V. M., 2016. Impact of a localized source of subglacial discharge on the heat flux and submarine melting of a tidewater glacier: A laboratory study. *Journal of Physical Oceanography*, 46, 10 (2016), 3155–3163. (cited on pages 71 and 89)

Cooper, P. and Hunt, G. R., 2010. The ventilated filling box containing a vertically distributed source of buoyancy. *Journal of Fluid Mechanics*, 646 (2010), 39–58. (cited on pages 13 and 32)

Cowton, T.; Slater, D.; Sole, A.; Goldberg, D.; and Nienow, P., 2015. Modeling the impact of glacial runoff on fjord circulation and submarine melt rate using a new subgrid-scale parameterization for glacial plumes. *Journal of Geophysical Research: Oceans*, 120, 2 (2015), 796–812. (cited on page 13)

D Jones, R. and Wells, A., 2018. Frazil-ice growth rate and dynamics in mixed layers and sub-ice-shelf plumes. *Cryosphere*, 12 (2018). (cited on page 93)

DeConto, R. M. and Pollard, D., 2016. Contribution of antarctica to past and future sea-level rise. *Nature*, 531, 7596 (2016), 591. (cited on page 48)

Depoorter, M. A.; Bamber, J.; Griggs, J.; Lenaerts, J.; Ligtenberg, S. R.; Van den Broeke, M.; and Moholdt, G., 2013. Calving fluxes and basal melt rates of antarctic ice shelves. *Nature*, 502, 7469 (2013), 89. (cited on page 2)

Dinniman, M. S.; Asay-Davis, X. S.; Galton-Fenzi, B. K.; Holland, P. R.; Jenkins, A.; and Timmermann, R., 2016. Modeling ice shelf/ocean interaction in antarctica: A review. *Oceanography*, 29, 4 (2016), 144–153. (cited on pages 15 and 6)

Dutrieux, P.; Stewart, C.; Jenkins, A.; Nicholls, K. W.; Corr, H. F.; Rignot, E.; and Steffen, K., 2014. Basal terraces on melting ice shelves. *Geophysical Research Letters*, 41, 15 (2014), 5506–5513. (cited on pages 15, 10, 11, and 93)

Ellison, T. H. and Turner, J. S., 1959. Turbulent entrainment in stratified flows. *J. Fluid Mech.*, 6 (Oct. 1959), 423–448. (cited on pages 19, 32, 76, and 89)

Ezhova, E.; Cenedese, C.; and Brandt, L., 2018. Dynamics of three-dimensional turbulent wall plumes and implications for estimates of submarine glacier melting. *Journal of Physical Oceanography*, 48, 9 (2018), 1941–1950. (cited on pages 48 and 58)

Feltham, D.; Untersteiner, N.; Wettlaufer, J.; and Worster, M., 2006. Sea ice is a mushy layer. *Geophysical Research Letters*, 33, 14 (2006). (cited on page 93)

Fischer, H. B.; List, J. E.; Koh, C. R.; Imberger, J.; and Brooks, N. H., 2013. *Mixing in inland and coastal waters*. Elsevier. (cited on pages 71 and 76)

FitzMmaurice, A.; Cenedese, C.; and Straneo, F., 2017. Nonlinear response of iceberg side melting to ocean currents. *Geophysical Research Letters*, 44, 11 (2017), 5637–5644. (cited on page 49)

Fricker, H. A.; Coleman, R.; Padman, L.; Scambos, T. A.; Bohlander, J.; and Brunt, K. M., 2009. Mapping the grounding zone of the amery ice shelf, east antarctica using insar, modis and icesat. *Antarctic Science*, 21, 5 (2009), 515–532. (cited on page 71)

Fricker, H. A.; Scambos, T.; Bindschadler, R.; and Padman, L., 2007. An active subglacial water system in west antarctica mapped from space. *Science*, 315, 5818 (2007), 1544–1548. (cited on page 71)

Fried, M. J.; Catania, G.; Bartholomaus, T.; Duncan, D.; Davis, M.; Stearns, L.; Nash, J.; Shroyer, E.; and Sutherland, D., 2015. Distributed subglacial discharge drives significant submarine melt at a greenland tidewater glacier. *Geophysical Research Letters*, 42, 21 (2015), 9328–9336. (cited on page 70)

Galton-Fenzi, B.; Hunter, J.; Coleman, R.; Marsland, S.; and Warner, R., 2012a. Modeling the basal melting and marine ice accretion of the amery ice shelf. *Journal of Geophysical Research: Oceans*, 117, C9 (2012). (cited on page 18)

Galton-Fenzi, B.; Hunter, J.; Coleman, R.; Marsland, S.; and Warner, R., 2012b. Modeling the basal melting and marine ice accretion of the amery ice shelf. *Journal of Geophysical Research: Oceans*, 117, C9 (2012). (cited on page 93)

Gardner, A. S.; Moholdt, G.; Scambos, T.; Fahnstock, M.; Ligtenberg, S.; van den Broeke, M.; and Nilsson, J., 2018. Increased west antarctic and unchanged east antarctic ice discharge over the last 7 years. *Cryosphere*, 12, 2 (2018), 521–547. (cited on page 1)

Gayen, B., 2012. *Turbulence and Internal Waves in tidal flow over topography*. Ph.D. thesis. https://search.proquest.com/docview/927601250?accountid=8330. ProQuest Dissertations and Theses, Copyright - Database copyright ProQuest LLC; ProQuest does not claim copyright in the individual underlying works; Last updated - 2016-03-11. (cited on page 24)

Gayen, B.; Griffiths, R. W.; and Hughes, G. O., 2014. Stability transitions and turbulence in horizontal convection. *Journal of Fluid Mechanics*, 751 (2014), 698–724. (cited on page 25)

Gayen, B.; Griffiths, R. W.; and Kerr, R. C., 2015. Melting driven convection at the ice-seawater interface. *Procedia IUTAM*, 15 (2015), 78–85. (cited on pages 14 and 50)

Gayen, B.; Griffiths, R. W.; and Kerr, R. C., 2016. Simulation of convection at a vertical ice face dissolving into saline water. *Journal of Fluid Mechanics*, 798 (2016), 284–298. (cited on pages 14, 18, 19, 24, 25, 29, 32, 35, 36, 44, 47, 48, 49, 50, 52, and 74)

Gayen, B. and Sarkar, S., 2011. Direct and large-eddy simulations of internal tide generation at a near-critical slope. *Journal of Fluid Mechanics*, 681 (2011), 48–79. (cited on pages 24 and 25)

Gayen, B.; Sarkar, S.; and Taylor, J. R., 2010. Large eddy simulation of a stratified boundary layer under an oscillatory current. *J. Fluid Mech.*, 643 (2010), 233–266. (cited on page 50)

George Jr, W. K. and Capp, S. P., 1979. A theory for natural convection turbulent boundary layers next to heated vertical surfaces. *International Journal of Heat and Mass Transfer*, 22, 6 (1979), 813–826. (cited on page 30)

Gladish, C. V.; Holland, D. M.; Holland, P. R.; and Price, S. F., 2012. Ice-shelf basal channels in a coupled ice/ocean model. *J. Glaciol.*, 58 (Sep. 2012), 1227–1244. (cited on pages 18 and 48)

Golledge, N. R.; Keller, E. D.; Gomez, N.; Naughten, K. A.; Bernales, J.; Trusel, L. D.; and Edwards, T. L., 2019. Global environmental consequences of twenty-first-century ice-sheet melt. *Nature*, 566, 7742 (2019), 65. (cited on pages 3 and 69)

Golledge, N. R.; Kowalewski, D. E.; Naish, T. R.; Levy, R. H.; Fogwill, C. J.; and Gasson, E. G., 2015. The multi-millennial antarctic commitment to future sea-level rise. *Nature*, 526, 7573 (2015), 421. (cited on page 3)

Gray, L.; Joughin, I.; Tulaczyk, S.; Spikes, V. B.; Bindschadler, R.; and Jezek, K., 2005. Evidence for subglacial water transport in the west antarctic ice sheet through three-dimensional satellite radar interferometry. *Geophysical Research Letters*, 32, 3 (2005). (cited on page 71)

Grella, J. and Faeth, G., 1975. Measurements in a two-dimensional thermal plume along a vertical adiabatic wall. *Journal of Fluid Mechanics*, 71, 4 (1975), 701–710. (cited on page 76)

Grossmann, S. and Lohse, D., 2000. Scaling in thermal convection: a unifying theory. *Journal of Fluid Mechanics*, 407 (2000), 27–56. (cited on page 44)

GWYTHER, D.; GALTON-FENZI, B.; HUNTER, J.; AND ROBERTS, J., 2014. Simulated melt rates for the totten and dalton ice shelves. *Ocean Science*, 10, 3 (2014), 267–279. (cited on page 4)

GWYTHER, D. E.; COUGNON, E. A.; GALTON-FENZI, B. K.; ROBERTS, J. L.; HUNTER, J. R.; AND DINNIMAN, M. S., 2016. Modelling the response of ice shelf basal melting to different ocean cavity environmental regimes. *Annals of Glaciology*, 57, 73 (2016), 131–141. (cited on page 93)

GWYTHER, D. E.; GALTON-FENZI, B. K.; DINNIMAN, M. S.; ROBERTS, J. L.; AND HUNTER, J. R., 2015. The effect of basal friction on melting and freezing in ice shelf–ocean models. *Ocean Modelling*, 95 (2015), 38–52. (cited on page 70)

HARIG, C.; LEWIS, K. W.; PLATTNER, A.; AND SIMONS, F. J., 2015. A suite of soft analyzes data on the sphere. *Eos*, (2015). (cited on page 1)

HELLMER, H. H. AND OLBERS, D. J., 1989. A two-dimensional model for the thermohaline circulation under an ice shelf. *Antarctic Science*, 1, 4 (1989), 325–336. (cited on pages 13 and 18)

HELM, V.; HUMBERT, A.; AND MILLER, H., 2014. Elevation and elevation change of greenland and antarctica derived from cryosat-2. *The Cryosphere*, 8, 4 (2014), 1539–1559. (cited on page 1)

HERLINA, H. AND WISSINK, J., 2014. Direct numerical simulation of turbulent scalar transport across a flat surface. *Journal of Fluid Mechanics*, 744 (2014), 217–249. (cited on page 14)

HEWITT, I. J., 2019. Subglacial plumes. *Ann. Rev. Fluid Mech.*, 52 (2019). (cited on page 70)

HOLLAND, D. M. AND JENKINS, A. J., 1999. Modeling thermodynamic ice-ocean interactions at the base of an ice shelf. *Journal of Physical Oceanography*, 29 (1999), 1787–1800. (cited on pages 12, 23, 48, 50, and 70)

HOLLAND, P. R. AND FELTHAM, D. L., 2005. Frazil dynamics and precipitation in a water column with depth-dependent supercooling. *Journal of Fluid Mechanics*, 530 (2005), 101–124. (cited on page 93)

HOLLAND, P. R. AND FELTHAM, D. L., 2006. The effects of rotation and ice shelf topography on frazil-laden ice shelf water plumes. *Journal of physical oceanography*, 36, 12 (2006), 2312–2327. (cited on page 13)

HOLMAN, J. P., 2010. *Heat Transfer (McGraw-Hill Series in Mechanical Engineering)*. Science Engineering & Math, 10 edn. ISBN 9780073529363. https://www.amazon.com/Heat-Transfer-McGraw-Hill-Mechanical-Engineering-ebook/dp/B006RB2G6C?SubscriptionId=0JYN1NVW651KCA56C102&tag=techkie-20&linkCode=xm2&camp=2025&creative=165953&creativeASIN=B006RB2G6C. (cited on pages 19, 25, 29, and 76)

Huppert, H. E. and Josberger, E. G., 1980. The melting of ice in cold stratified water. *J. Phys. Oceanogr.*, 10 (1980), 953–960. (cited on page 10)

Huppert, H. E. and Turner, J. S., 1978. On melting icebergs. *Nature*, 271 (1978), 46–48. (cited on page 18)

Huppert, H. E. and Turner, J. S., 1980. Ice blocks melting into a salinity gradient. *Journal of Fluid Mechanics*, 100 (9 1980), 367–384. doi:10.1017/S0022112080001206. http://journals.cambridge.org/article_S0022112080001206. (cited on pages 10 and 18)

Husband, W. and Ozsahin, S., 1967. Rates of dissolution of potash ore. *The Canadian Journal of Chemical Engineering*, 45, 4 (1967), 234–237. (cited on page 27)

IPCC, A., 2014. : Climate change: Synthesis Report. Contribution of Working Groups i, ii, iii to the Fifth Assesment Report of the Intergovernmental Panel on Climate Change. Technical report, IPCC, Geneva, Switzerland. (cited on page 1)

Jacobs, S.; Huppert, H.; Holdsworth, G.; and Drewry, D., 1981. Thermohaline steps induced by melting of the erebus glacier tongue. *Journal of Geophysical Research: Oceans*, 86, C7 (1981), 6547–6555. (cited on page 10)

Jacobs, S. S.; Jenkins, A.; Giulivi, C. F.; and Dutrieux, P., 2011. Stronger ocean circulation and increased melting under Pine Island Glacier ice shelf. *Nature Geoscience*, 4 (2011), 519–523. (cited on page 18)

Jenkins, A., 1991. A One-Dimensional Model of Ice Shelf-Ocean Interaction. *J. Geophys. Res.*, 96, C11 (Nov. 1991), 20671–20677. (cited on pages 12, 19, 44, and 48)

Jenkins, A., 2011a. Convection-driven melting near the grounding lines of ice shelves and tidewater glaciers. *Journal of Physical Oceanography*, 41, 12 (2011), 2279–2294. (cited on pages 15, 4, 5, 10, 11, 19, 20, and 48)

Jenkins, A., 2011b. Convection-driven melting near the grounding lines of ice shelves and tidewater glaciers. *Journal of Physical Oceanography*, 41 (December 2011), 2279–2294. (cited on page 13)

Jenkins, A., 2016. A simple model of the ice shelf–ocean boundary layer and current. *Journal of Physical Oceanography*, 46, 6 (2016), 1785–1803. (cited on page 48)

Jenkins, A. and Bombosch, A., 1995. Modeling the effects of frazil ice crystals on the dynamics and thermodynamics of ice shelf water plumes. *Journal of Geophysical Research: Oceans*, 100, C4 (1995), 6967–6981. (cited on page 93)

Jenkins, A.; Dutrieux, P.; Jacobs, S. S.; McPhail, S. D.; Perrett, J. R.; Webb, A. T.; and White, D., 2010. Observations beneath Pine Island Glacier in West Antarctica and implications for its retreat. *Nature Geoscience*, 3 (2010), 468–472. (cited on pages 18 and 20)

Johnson, R. and Mollendorf, J., 1984. Transport from a vertical ice surface melting in saline water. *International journal of heat and mass transfer*, 27, 10 (1984), 1928–1932. (cited on page 10)

Jordan, J. R.; Kimura, S.; Holland, P. R.; Jenkins, A.; and Piggott, M. D., 2015. On the conditional frazil ice instability in seawater. *Journal of Physical Oceanography*, 45, 4 (2015), 1121–1138. (cited on page 93)

Josberger, E. G., 1979. Laminar and turbulent boundary layers adjacent to melting vertical ice walls in salt water. Technical report, WASHINGTON UNIV SEATTLE DEPT OF ATMOSPHERIC SCIENCES. (cited on page 8)

Josberger, E. G. and Martin, S., 1981. A laboratory and theoretical study of the boundary layer adjacent to a vertical melting ice wall in salt water. *Journal of Fluid Mechanics*, 111 (1981), 439–473. (cited on pages 8, 10, 14, 18, 19, 25, 29, 35, 36, 49, and 76)

Kader, B. and Yaglom, A., 1972. Heat and mass transfer laws for fully turbulent wall flows. *International Journal of Heat and Mass Transfer*, 15, 12 (1972), 2329–2351. (cited on page 13)

Kerr, R. C., 1994. Melting driven by vigorous compositional convection. *Journal of Fluid Mechanics*, 280 (1994), 255–285. (cited on pages 8 and 18)

Kerr, R. C. and McConnochie, C. D., 2015. Dissolution of a vertical solid surface by turbulent compositional convection. *Journal of Fluid Mechanics*, 765 (2015), 211–228. (cited on pages 10, 14, 18, 19, 23, 30, 32, 35, 36, 44, 48, and 49)

Khazendar, A. and Jenkins, A., 2003. A model of marine ice formation within antarctic ice shelf rifts. *Journal of Geophysical Research: Oceans*, 108, C7 (2003). (cited on page 93)

Khazendar, A.; Schodlok, M.; Fenty, I.; Ligtenberg, S.; Rignot, E.; and Van Den Broeke, M., 2013. Observed thinning of totten glacier is linked to coastal polynya variability. *Nature communications*, 4 (2013), 2857. (cited on page 4)

Kimura, S.; Nicholls, K. W.; and Venables, E., 2015. Estimation of ice shelf melt rate in the presence of a thermohaline staircase. *Journal of Physical Oceanography*, 45, 1 (2015), 133–148. (cited on page 11)

Kuiken, H., 1968. An asymptotic solution for large prandtl number free convection. *Journal of Engineering Mathematics*, 2, 4 (1968), 355–371. (cited on page 8)

Kundu, P. and Cohen, L., 1990. Fluid mechanics, 638 pp. *Academic, Calif*, (1990). (cited on page 59)

Lavergne, C.; Palter, J. B.; Galbraith, E. D.; Bernardello, R.; and Marinov, I., 2014. Cessation of deep convection in the open Southern Ocean under anthropogenic climate change. *Nat. Clim. Change*, 4 (March 2014), 278–282. doi:10.1038/NCLIMATE2132. (cited on page 17)

LE BROCQ, A. M.; ROSS, N.; GRIGGS, J. A.; BINGHAM, R. G.; CORR, H. F.; FERRACCIOLI, F.; JENKINS, A.; JORDAN, T. A.; PAYNE, A. J.; RIPPIN, D. M.; ET AL., 2013. Evidence from ice shelves for channelized meltwater flow beneath the antarctic ice sheet. *Nature Geoscience*, 6, 11 (2013), 945. (cited on pages 11, 71, and 72)

MAGORRIAN, S. J. AND WELLS, A. J., 2016. Turbulent plumes from a glacier terminus melting in a stratified ocean. *J. Geophys. Res. Oceans*, 121 (June 2016), 4670–4696. doi:10.1002/2015JC011160. (cited on pages 13, 19, 20, and 44)

MAKINSON, K.; HOLLAND, P. R.; JENKINS, A.; NICHOLLS, K. W.; AND HOLLAND, D. M., 2011. Influence of tides on melting and freezing beneath filchner-ronne ice shelf, antarctica. *Geophysical Research Letters*, 38, 6 (2011). (cited on page 11)

MARSH, O. J.; FRICKER, H. A.; SIEGFRIED, M. R.; CHRISTIANSON, K.; NICHOLLS, K. W.; CORR, H. F.; AND CATANIA, G., 2016. High basal melting forming a channel at the grounding line of ross ice shelf, antarctica. *Geophysical Research Letters*, 43, 1 (2016), 250–255. (cited on page 71)

MARTÍN-ESPAÑOL, A.; ZAMMIT-MANGION, A.; CLARKE, P. J.; FLAMENT, T.; HELM, V.; KING, M. A.; LUTHCKE, S. B.; PETRIE, E.; RÉMY, F.; SCHÖN, N.; ET AL., 2016. Spatial and temporal antarctic ice sheet mass trends, glacio-isostatic adjustment, and surface processes from a joint inversion of satellite altimeter, gravity, and gps data. *Journal of Geophysical Research: Earth Surface*, 121, 2 (2016), 182–200. (cited on page 1)

MCCONNOCHIE, C. D. AND KERR, R. C., 2016. The turbulent wall plume from a vertically distributed source of buoyancy. *J. Fluid Mech.*, 787 (2016), 237–253. doi: 10.1017/jfm.2015.691. (cited on pages 19 and 48)

MCCONNOCHIE, C. D. AND KERR, R. C., 2016b. The effect of a salinity gradient on the dissolution of a vertical ice face. *J. Fluid Mech.*, 791 (2016b), 589–607. doi: 10.1017/jfm.2016.62. (cited on pages 10, 45, and 48)

MCCONNOCHIE, C. D. AND KERR, R. C., 2017. Testing a common ice-ocean parameterization with laboratory experiments. *J. Geophys. Res. Oceans*, 122 (2017), 5905–5915. (cited on pages 45 and 70)

MCCONNOCHIE, C. D. AND KERR, R. C., 2017a. Enhanced ablation of a vertical ice wall due to an external freshwater plume. *J. Fluid Mech.*, 810 (2017a), 429–447. doi:10.1017/jfm.2016.761. (cited on pages 45, 71, 75, 76, 78, 84, and 89)

MCCONNOCHIE, C. D. AND KERR, R. C., 2018. Dissolution of a sloping solid surface by turbulent compositional convection. *Journal of Fluid Mechanics*, 846 (2018), 563–577. (cited on pages 48, 49, and 72)

MCMILLAN, M.; SHEPHERD, A.; SUNDAL, A.; BRIGGS, K.; MUIR, A.; RIDOUT, A.; HOGG, A.; AND WINGHAM, D., 2014. Increased ice losses from antarctica detected by cryosat-2. *Geophysical Research Letters*, 41, 11 (2014), 3899–3905. (cited on page 1)

McPhee, M. G., 1992. Turbulent heat flux in the upper ocean under sea ice. *Journal of Geophysical Research: Oceans*, 97, C4 (1992), 5365–5379. (cited on page 48)

McPhee, M. G.; Kottmeier, C.; and Morison, J. H., 1999. Ocean heat flux in the central weddell sea during winter. *Journal of Physical Oceanography*, 29, 6 (1999), 1166–1179. (cited on page 48)

McPhee, M. G.; Maykut, G. A.; and Morison, J. H., 1987. Dynamics and thermodynamics of the ice/upper ocean system in the marginal ice zone of the greenland sea. *Journal of Geophysical Research: Oceans*, 92, C7 (1987), 7017–7031. (cited on page 13)

Mondal, M.; Gayen, B.; Griffiths, R. W.; and Kerr, R. C., 2019. Ablation of sloping ice faces into polar seawater. *Journal of Fluid Mechanics*, 863 (2019), 545–571. (cited on pages 18, 19, 47, 48, 49, 50, 52, 53, 55, 56, 58, 66, 72, 73, 74, and 75)

Morgan, V. I. and Budd, W. F., 1978. The distribution, movements and melt rates of Antarctic Iceburghs. In *Iceberg Utilization: Proceedings of the First International Conference and Workshops on Iceberg Utilization for Fresh Water Production, Weather Modification and Other Applications Held at Iowa State University, Ames, Iowa, USA, October 2-6, 1977*, 220–228. Pergamon Press, New York. (cited on page 19)

Morrison, A. K.; Hogg, A. M.; and Ward, M. L., 2011. Sensitivity of the Southern Ocean overturning circulation to surface buoyancy forcing. *Geophys. Res. Lett.*, 38 (July 2011), L14602. (cited on page 18)

Morton, B. R.; Taylor, G.; and Turner, J. S., 1956. Turbulent Gravitational Convection from Maintained and Instantaneous Sources. *Proceedings of the Royal Society of London. Series A. Mathematical and Physical Sciences*, 234 (Jan. 1956), 1–23. (cited on pages 19 and 32)

Motyka, R. J.; Dryer, W. P.; Amundson, J.; Truffer, M.; and Fahnestock, M., 2013. Rapid submarine melting driven by subglacial discharge, leconte glacier, alaska. *Geophysical Research Letters*, 40, 19 (2013), 5153–5158. (cited on page 70)

Moyer, A. N.; Nienow, P. W.; Gourmelen, N.; Sole, A. J.; and Slater, D. A., 2017. Estimating spring terminus submarine melt rates at a greenlandic tidewater glacier using satellite imagery. *Frontiers in Earth Science*, 5 (2017), 107. (cited on pages 19, 70, and 73)

Nakayama, Y.; Menemenlis, D.; Zhang, H.; Schodlok, M.; and Rignot, E., 2018. Origin of circumpolar deep water intruding onto the amundsen and bellingshausen sea continental shelves. *Nature communications*, 9, 1 (2018), 3403. (cited on page 3)

Nilson, R., 1985. Countercurrent convection in a double-diffusive boundary layer. *Journal of Fluid Mechanics*, 160 (1985), 181–210. (cited on pages 8, 18, 28, and 35)

ORSE, A.; JOHNSON, G.; AND BULLISTER, J. L., 1999. Circulation, mixing, and the prouction of antarctic bottom water. *Progress in Oceanography*, 43 (1999), 55–109. (cited on page 4)

PADMAN, L.; SIEGFRIED, M. R.; AND FRICKER, H. A., 2018. Ocean tide influences on the antarctic and greenland ice sheets. *Reviews of Geophysics*, 56, 1 (2018), 142–184. (cited on pages 15, 11, 12, 67, and 93)

PAOLO, F. S.; FRICKER, H. A.; AND PADMAN, L., 2015. Volume loss from antarctic ice shelves is accelerating. *Science*, 348, 6232 (2015), 327–331. (cited on page 47)

PAOLO, F. S.; FRICKER, H. A.; AND PADMAN, L., 2016. Constructing improved decadal records of Antarctic ice shelf height change from multiple satellite radar altimeters. *Remote Sens. Environ.*, 177 (May 2016), 192–205. (cited on pages 17 and 47)

PATTON, H.; SWIFT, D.; CLARK, C.; LIVINGSTONE, S. J.; AND COOK, S. J., 2016. Distribution and characteristics of overdeepenings beneath the greenland and antarctic ice sheets: Implications for overdeepening origin and evolution. *Quaternary Science Reviews*, 148 (2016), 128–145. (cited on pages 15, 10, 11, and 93)

PAYNE, A. J.; HOLLAND, P. R.; SHEPHERD, A. P.; RUTT, I. C.; JENKINS, A.; AND JOUGHIN, I., 2007. Numerical modeling of ocean-ice interactions under pine island bay's ice shelf. *Journal of Geophysical Research: Oceans*, 112, C10 (2007). (cited on pages 13, 19, and 48)

PAYNE, A. J.; VIELI, A.; SHEPHERD, A. P.; WINGHAM, D. J.; AND RIGNOT, E., 2004. Recent dramatic thinning of largest West Antarctic ice stream triggered by oceans. *Geophysical Research Letters*, 31 (2004), L23401. (cited on pages 1 and 3)

PICARD, G.; DOMINE, F.; KRINNER, G.; ARNAUD, L.; AND LEFEBVRE, E., 2012. Inhibition of the positive snow-albedo feedback by precipitation in interior Antarctica. *Nat. Clim. Change*, 2 (July 2012), 795–798. doi:10.1038/NClimate1590. (cited on page 47)

PIECUCH, C. G. AND PONTE, R. M., 2014. Mechanisms of global-mean steric sea level change. *J. Clim.*, 27, 2 (2014), 824–834. doi:10.1175/JCLI-D-13-00373.1. (cited on page 17)

PRINGLE, D.; TRODAHL, H.; AND HASKELL, T., 2006. Direct measurement of sea ice thermal conductivity: No surface reduction. *Journal of Geophysical Research: Oceans*, 111, C5 (2006). (cited on page 6)

REED MACAYEAL, D., 1984. Numerical simulations of the ross sea tides. *Journal of Geophysical Research*, 89 (1984), 607–615. (cited on page 13)

RIGNOT, E.; FENTY, I.; XU, Y.; CAI, C.; AND KEMP, C., 2015. Undercutting of marine-terminating glaciers in West Greenland. *Geophys. Res. Lett.*, 42, 14 (2015), 5909–5917. (cited on page 70)

Rignot, E.; Jacobs, S.; Mouginot, J.; and Scheuchl, B., 2013. Ice-shelf melting around antarctica. *Science*, 341, 6143 (2013), 266–270. (cited on pages 15, 2, 20, 47, and 69)

Rignot, E.; Mouginot, J.; Scheuchl, B.; van den Broeke, M.; van Wessem, M. J.; and Morlighem, M., 2019. Four decades of Antarctic Ice Sheet mass balance from 1979–2017. *Proceedings of the National Academy of Sciences*, 116, 4 (2019), 1095–1103. (cited on page 69)

Rignot, E. and Steffen, K., 2008. Channelized bottom melting and stability of floating ice shelves. *Geophysical Research Letters*, 35, 2 (2008). (cited on page 71)

Rignot, E.; Velicogna, I.; van den Broeke, M. R.; Monaghan, A.; and Lenaerts, J. T., 2011. Acceleration of the contribution of the greenland and antarctic ice sheets to sea level rise. *Geophysical Research Letters*, 38, 5 (2011). (cited on page 1)

Rydt, J. D. and Gudmundsson, G. H., 2016. Coupled ice shelf-ocean modeling and complex grounding line retreat from a seabed ridge. *Journal of Geophysical Research: Oceans*, 121 (2016), 865–880. (cited on page 18)

Salcedo-Castro, J.; Bourgault, D.; et al., 2011. Circulation induced by subglacial discharge in glacial fjords: Results from idealized numerical simulations. *Continental Shelf Research*, 31, 13 (2011), 1396–1406. (cited on page 70)

Sangras, R.; Dai, Z.; and Faeth, G., 1998. Mixing structure of plane self-preserving buoyant turbulent plumes. *Journal of heat transfer*, 120, 4 (1998), 1033–1041. (cited on page 76)

Schmidtko, S.; Heywood, K. J.; Thompson, A. F.; and Aoki, S., 2014. Multidecadal warming of antarctic waters. *Science*, 346, 6214 (2014), 1227–1231. (cited on page 3)

Schodlok, M.; Menemenlis, D.; and Rignot, E., 2016. Ice shelf basal melt rates around a ntarctica from simulations and observations. *Journal of Geophysical Research: Oceans*, 121, 2 (2016), 1085–1109. (cited on page 48)

Sciascia, R.; Cenedese, C.; Nicoli, D.; Heimbach, P.; and Straneo, F., 2014. Impact of periodic intermediary flows on submarine melting of a g reenland glacier. *Journal of Geophysical Research: Oceans*, 119, 10 (2014), 7078–7098. (cited on page 48)

Sciascia, R.; Straneo, F.; Cenedese, C.; and Heimbach, P., 2013a. Seasonal variability of submarine melt rate and circulation in an east greenland fjord. *Journal of Geophysical Research: Oceans*, 118, 5 (2013), 2492–2506. (cited on page 48)

Sciascia, R.; Straneo, F.; Cenedese, C.; and Heimbach, P., 2013b. Seasonal variability of submarine melt rate and circulation in an east greenland fjord. *Journal of Geophysical Research: Oceans*, 118, 5 (2013), 2492–2506. (cited on page 70)

Sergienko, O., 2013. Basal channels on ice shelves. *Journal of Geophysical Research: Earth Surface*, 118, 3 (2013), 1342–1355. (cited on page 71)

Serreze, M. C. and Barry, R. G., 2011. Processes and impacts of Arctic amplification: A research synthesis. *Global and planetary change*, 77, 1-2 (2011), 85–96. (cited on page 69)

Shepherd, A.; A, E. R. I. G.; Barletta, V. R.; Bettadpur, M. J. B. S.; and H, K., 2012a. A reconciled estimate of ice-sheet mass balance. *Science*, 338 (Nov 2012). doi:10.1038/nature12238. (cited on page 1)

Shepherd, A.; Ivins, E.; Rignot, E.; Smith, B.; van den Broeke, M.; Velicogna, I.; Whitehouse, P.; Briggs, K.; Joughin, I.; Krinner, G.; et al., 2018. Mass balance of the antarctic ice sheet from 1992 to 2017. *Nature*, 556 (2018), pages219–222. (cited on page 1)

Shepherd, A.; Ivins, E. R.; Geruo, A.; Barletta, V. R.; Bentley, M. J.; Bettadpur, S.; Briggs, K. H.; Bromwich, D. H.; Forsberg, R.; Galin, N.; et al., 2012b. A reconciled estimate of ice-sheet mass balance. *Science*, 338, 6111 (2012), 1183–1189. (cited on page 1)

Shepherd, A.; Wingham, D.; and Rignot, E., 2004. Warm ocean is eroding west antarctic ice sheet. *Geophys. Res. Lett.*, 31, 23 (2004), n/a–n/a. doi:10.1029/2004GL021106. http://dx.doi.org/10.1029/2004GL021106. L23402. (cited on page 19)

Siegert, M. J., 2005. Lakes beneath the ice sheet: the occurrence, analysis, and future exploration of lake vostok and other antarctic subglacial lakes. *Annual Review of Earth and Planetary Science*, 33 (2005), 215–245. (cited on page 71)

Silvano, A.; Rintoul, S. R.; Peña-Molino, B.; Hobbs, W. R.; van Wijk, E.; Aoki, S.; Tamura, T.; and Williams, G. D., 2018. Freshening by glacial meltwater enhances melting of ice shelves and reduces formation of antarctic bottom water. *Science advances*, 4, 4 (2018), eaap9467. (cited on page 4)

Slater, D.; Nienow, P.; Sole, A.; Cowton, T.; Mottram, R.; Langen, P.; and Mair, D., 2017. Spatially distributed runoff at the grounding line of a large greenlandic tidewater glacier inferred from plume modelling. *Journal of Glaciology*, 63, 238 (2017), 309–323. (cited on page 70)

Slater, D. A.; Goldberg, D. N.; Nienow, P. W.; and Cowton, T. R., 2016a. Scalings for submarine melting at tidewater glaciers from buoyant plume theory. *Journal of Physical Oceanography*, 46, 6 (2016), 1839–1855. doi:10.1175/JPO-D-15-0132.1. (cited on pages 13 and 19)

Slater, D. A.; Goldberg, D. N.; Nienow, P. W.; and Cowton, T. R., 2016b. Scalings for submarine melting at tidewater glaciers from buoyant plume theory. *Journal of Physical Oceanography*, 46, 6 (2016), 1839–1855. (cited on page 70)

Snow, K.; Hogg, A. M.; Sloyan, B. M.; and Downes, S. M., 2016. Sensitivity of Antarctic Bottom Water to change in surface buoyancy fluxes. *Journal of Climate*, 29 (January 2016), 313–330. doi:10.1175/JCLI-D-15_0467.1. (cited on page 18)

Spence, P.; Griffies, S. M.; England, M. H.; Hogg, A. M.; Saenko, O. A.; and Jourdain, N. C., 2014. Rapid subsurface warming and circulation changes of antarctic coastal waters by poleward shifting winds. *Geophysical Research Letters*, 41, 13 (2014), 4601–4610. (cited on page 18)

Stanton, T.; Shaw, W.; Truffer, M.; Corr, H.; Peters, L.; Riverman, K.; Bindschadler, R.; Holland, D.; and Anandakrishnan, S., 2013. Channelized ice melting in the ocean boundary layer beneath pine island glacier, antarctica. *Science*, 341, 6151 (2013), 1236–1239. (cited on page 11)

Stevens, C.; McPhee, M.; Forrest, A.; Leonard, G.; Stanton, T.; and Haskell, T., 2014. The influence of an antarctic glacier tongue on near-field ocean circulation and mixing. *Journal of Geophysical Research: Oceans*, 119, 4 (2014), 2344–2362. (cited on page 10)

Straneo, F. and Cenedese, C., 2015. The dynamics of greenland's glacial fjords and their role in climate. *Annual review of marine science*, 7 (2015), 89–112. (cited on page 71)

Sugden, D. E.; Denton, G. H.; and Marchant, D. R., 1991. Subglacial meltwater channel systems and ice sheet overriding, asgard range, antarctica. *Geografiska Annaler: Series A, Physical Geography*, 73, 2 (1991), 109–121. (cited on page 11)

Swingedouw, D.; Fichefet, T.; Huybrechts, P.; Goosse, H.; Driesschaert, E.; and Loutre, M.-F., 2008. Antarctic ice-sheet melting provides negative feedbacks on future climate warming. *Geophysical Research Letters*, 35, 17 (2008). (cited on page 18)

Thoma, M.; Jenkins, A.; Holland, D.; and Jacobs, S., 2008. Modelling circumpolar deep water intrusions on the amundsen sea continental shelf, antarctica. *Geophysical Research Letters*, 35, 18 (2008). (cited on page 3)

Tsuji, T. and Nagano, Y., 1988. Turbulence measurements in a natural convection boundary layer along a vertical flat plate. *International journal of heat and mass transfer*, 31, 10 (1988), 2101–2111. (cited on page 30)

Turner, J. S., 1979. *Buoyancy effects in fluids*. Cambridge University Press. (cited on pages 25 and 49)

van Wessem, J. M.; Jan Van De Berg, W.; Noël, B. P.; Van Meijgaard, E.; Amory, C.; Birnbaum, G.; Jakobs, C. L.; Krüger, K.; Lenaerts, J.; Lhermitte, S.; Ligtenberg, S. R. M.; Medley, B.; Reijmer, C. H.; van Tricht, K.; Trusel, L. D.; van Ulft, L. H.; Wouters, B.; Wuite, J.; and van den Broeke, M. R., 2018. Modelling the climate and surface mass balance of polar ice sheets using RACMO2: Part 2: Antarctica (1979-2016). *Cryosphere*, 12, 4 (2018), 1479–1498. (cited on page 69)

Vaughan, D. G.; Comiso, J. C.; Allison, I.; Carrasco, J.; Kaser, G.; Kwok, R.; Mote, P.; Murray, T.; Paul, F.; Ren, J.; et al., 2013. Observations: cryosphere. *Climate change*, 2103 (2013), 317–382. (cited on pages 1 and 3)

Velicogna, I., 2009. Increasing rates of ice mass loss from the greenland and antarctic ice sheets revealed by grace. *Geophysical Research Letters*, 36, 19 (2009). (cited on page 1)

Vliet, G. C., 1969. Natural convection local heat transfer on constant-heat flux inclined surfaces. *Journal of Heat Transfer*, (November 1969), 511–516. (cited on page 40)

Vreugdenhil, C. A. and Taylor, J. R., 2019. Stratification effects in the turbulent boundary layer beneath a melting ice shelf: insights from resolved large-eddy simulations. *Journal of Physical Oceanography*, , 2019 (2019). (cited on pages 72 and 93)

Wåhlin, A.; Yuan, X.; Björk, G.; and Nohr, C., 2010. Inflow of warm circumpolar deep water in the central amundsen shelf. *Journal of Physical Oceanography*, 40, 6 (2010), 1427–1434. (cited on page 3)

Walker, D. P.; Brandon, M. A.; Jenkins, A.; Allen, J. T.; Dowdeswell, J. A.; and Evans, J., 2007. Oceanic heat transport onto the amundsen sea shelf through a submarine glacial trough. *Geophysical Research Letters*, 34, 2 (2007). (cited on page 3)

Washburn, E. W., 1926. *International Critical Tables of Numerical Data, Physics, Chemistry and Technology*. The National Academies Press, Washington, DC. doi:10.17226/20230. https://www.nap.edu/catalog/20230/international-critical-tables-of-numerical-data-physics-chemistry-and-technology. (cited on page 25)

Weast, R. C.; Astle, M. J.; Beyer, W. H.; et al., 1989. *CRC handbook of chemistry and physics*, vol. 1990. CRC press, Boca raton FL. (cited on page 25)

Wells, A. J. and Worster, M. G., 2008. A geophysical-scale model of vertical natural convection boundary layers. *Journal of Fluid Mechanics*, 609 (2008), 111–137. (cited on pages 27, 30, 32, and 44)

Wells, A. J. and Worster, M. G., 2011. Melting and dissolving of a vertical solid surface with laminar compositional convection. *Journal of Fluid Mechanics*, 687 (2011), 118–140. (cited on pages 7, 8, 18, 23, 26, 27, and 29)

Wells, M. and Wettlaufer, J., 2005. Two-dimensional density currents in a confined basin. *Geophysical & Astrophysical Fluid Dynamics*, 99, 3 (2005), 199–218. (cited on page 13)

Wilchinsky, A. V.; Heorton, H. D.; Feltham, D. L.; and Holland, P. R., 2015. Study of the impact of ice formation in leads upon the sea ice pack mass balance using a new frazil and grease ice parameterization. *Journal of Physical Oceanography*, 45, 8 (2015), 2025–2047. (cited on page 93)

Wingham, D. J.; Siegert, M. J.; Shepherd, A.; and Muir, A. S., 2006. Rapid discharge connects antarctic subglacial lakes. *Nature*, 440, 7087 (2006), 1033. (cited on page 71)

Woods, A. W., 1992. Melting and dissolving. *Journal of Fluid Mechanics*, 239 (1992), 429–448. (cited on page 18)